Airfoil self-noise predictions using DDES and the FWH analogy

P. Pindi Nataraj

191199198 : Master Graduation Assignment

Graduation number : 399

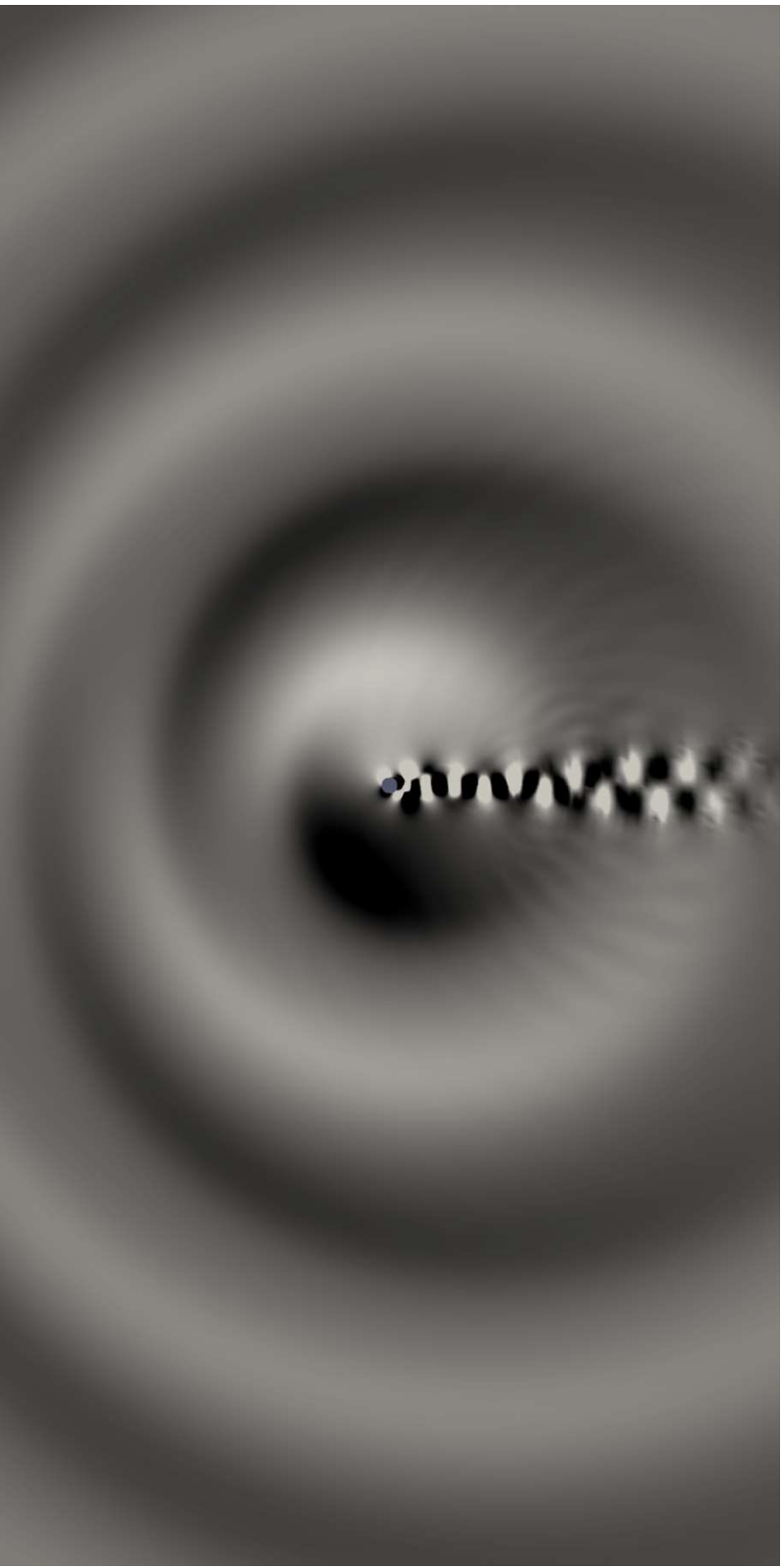

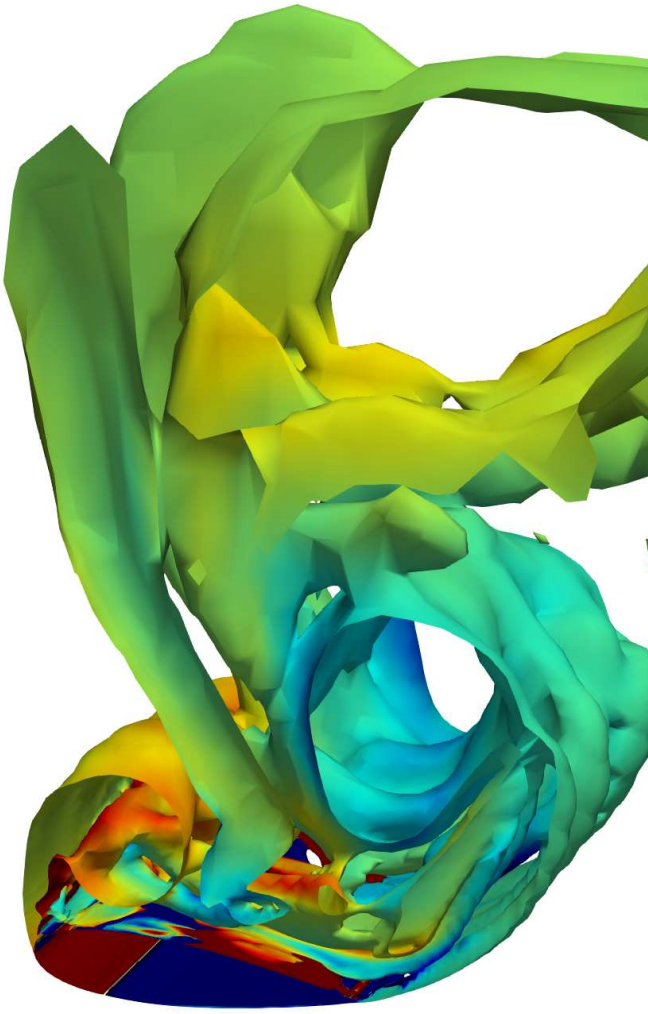

UNIVERSITY OF TWENTE.

TNO innovation for life

Airfoil self-noise predictions using DDES and the FWH analogy

A thesis submitted in fulfillment of the requirements for the degree of Master of Science in

Mechanical Engineering

at the University of Twente

Graduation number: 399

Student Name: Prakyath Pindi Nataraj
Student Number: 2322129

Graduation Assessment Committee

Chairman: Prof.dr.ir. C.H. Venner
University Supervisor: dr. H. Ozdemir
Company Supervisor: dr. A. Koodly Ravishankara
External Member: ir. L.G. Koerkamp

Host institutions:

University of Twente, TNO Petten

To be publicly defended on Monday, 25 April, 2022

ABSTRACT

Noise emissions from wind turbines are one of the hurdles to expanding existing wind energy infrastructure in the vicinity of urban environments. Airfoil self-noise is one of the fundamental contributors to wind turbine noise. Noise mitigation strategies in the form of blade add-ons have been the focus of contemporary research. A comprehensive understanding of the physics involved in noise generation is necessary to devise add-ons such as trailing edge serrations, metal foam trailing edges, and vortex generators; this can be accomplished by conducting wind tunnel experiments or high-fidelity simulations. However, wind tunnel experiments for certain flow regimes such as deep stall involve installation effects and jet interactions which have proven to be cumbersome to decouple. Thus, it is common practice to then resort to high-fidelity simulations for noise estimation in such regimes. Nevertheless, the scale disparity between the aerodynamic and acoustic phenomena renders high-fidelity approaches such as Direct Numerical Simulation (DNS) and Large Eddy Simulation (LES) impractical for direct noise predictions as they would require long simulation run times, complex numerical schemes, and very fine spatial and temporal resolution; these complications necessitate the use of lower fidelity approaches and acoustic analogies.

The scope of this thesis is to explore the applicability of one such CFD-CAA framework involving Delayed Detached-Eddy Simulation (DDES) and the Ffowcs-Williams and Hawkings (FWH) analogy to obtain far-field noise predictions for the significant airfoil self-noise mechanisms of turbulent boundary layer – trailing edge noise (TBL-TE) and separation-stall noise. In this regard, the CFD-CAA framework is first composed and validated successfully for a quasi-2D laminar flow test case. The focus is then shifted to analyzing the case of the NACA0021 in deep stall. The influence of dissipative convective schemes and sub-grid scale models on the flow resolution is investigated first, following which the DDES approach is validated with existing experimental and numerical data. Furthermore, the far-field acoustic data obtained with the help of the FWH workflow agrees qualitatively with the trends observed in the literature.

Finally, the case of the NACA0018 with attached flow is investigated with the DDES-FWH framework; this is a rather unconventional case for DDES as it does not involve flow separation. The boundary layer being resolved by RANS leads to an insufficient resolution of the length scales relevant for TBL-TE noise, thereby predicting a far-field noise signature that is not in line with the literature. It is then concluded that the DDES-FWH framework is only suitable for separation-stall noise and blunt trailing edge vortex shedding regimes, and LES-FWH is recommended for TBL-TE noise predictions.

CONTENTS

List of Figures

List of Tables

Acronyms

BPM Brooks, Pope and Marcolini. 8

CAA Computational Aeroacoustics. 1

CTU Convective Time Units. 46

DDES Delayed Detached-Eddy Simulation. i

DES Detached-Eddy Simulation. 18, 24

DG-FEM Discontinuous Galerkin Finite Element Method. 31

DNS Direct Numerical Simulation. i, 4, 22

FVM Finite Volume Method. 31

FWH Ffowcs-Williams and Hawkings. i, 4

GIS Grid Induced Separation. 25

JST Jameson-Schmidt-Turkel. 32

KH Kelvin-Helmholtz. 14

LBL-VS Laminar boundary layer – vortex shedding noise. 9

LBM Lattice-Boltzmann Method. 10

LES Large Eddy Simulation. i, 4, 22, 23

MSD Modelled Stress Depletion. 25

MUSCL Monotone Upstream-centered Schemes for Conservation Laws. 33

OASPL Overall Sound Pressure Level. 39

PSD Power Spectral Density. 20

RANS Reynolds-Averaged Navier Stokes. 22

RMS Root Mean Squared. 44

SA Spalart-Allmaras. 20, 23

SGS sub-grid scale. 22

SLA Shear Layer Adapted. 26

SPL Sound Pressure Level. 9

TBL-TE turbulent boundary layer – trailing edge noise. 1

URANS Unsteady Reynolds-Averaged Navier Stokes. 18

VTM Vortex Tilting Measure. 26

1 INTRODUCTION

Interest in airfoil self-noise predictions has been motivated by its importance to broadband helicopter rotor, wind turbine, and airframe noise [8]. From the point of view of wind turbine noise, trailing edge (TE) noise has proven to be a dominant noise source in the audible frequency range by measurements [22]. Although engineering models for TE noise are widespread, high-fidelity approaches are essential to validate such models and obtain accurate TE noise directivity patterns. Stall noise occurs when the flow over a section of the blade having thick airfoil profiles is stalled, in stall-regulated wind turbines and due to gusts. The lack of engineering models for stall noise stems from the difficulty inherent in predicting stall occurrence.

Consequently, the two alternatives to predicting stall noise would be numerical or experimental [23]. As Computational Aeroacoustics (CAA) is becoming more commonplace in acoustics research and development, Large Eddy Simulation (LES) and Direct Numerical Simulation (DNS) have proven to be reliable for both direct and hybrid CAA methods for predicting near and far-field noise data. In the hybrid method, the near field aerodynamic noise on the coupling surface is obtained by CFD, and analytical or numerical transport equations govern its propagation to an observer in the far-field.

The scope of this thesis is to explore the applicability of the hybrid CAA approach consisting of Hybrid RANS/LES method of Delayed Detached-Eddy Simulation coupled with the time-domain variant of the Ffowcs-Williams and Hawkings acoustic analogy [24] to predict far-field noise for the airfoil self-noise cases of low mach number turbulent boundary layer – trailing edge noise (TBL-TE) and separation-stall noise from the flow over an airfoil in deep stall. Wind tunnel testing of airfoils beyond stall poses additional problems of installation effects [8] and nozzle jet oscillations [9], which would have an impression on the far-field noise signature, thereby justifying the need for the coupled DDES-CAA approach. The former TBL-TE case is a rather unconventional application of DDES, making it an interesting case study.

To achieve the objectives set earlier, it is vital to identify and validate the appropriate DDES method and FWH workflow; the first step in this regard is to take stock of the various methods by reviewing the existing literature pertaining to the theory and application of DDES and the FWH acoustic analogy, which is done in Chapter 2. Furthermore, the airfoil self-noise predictions at low and moderate mach numbers by DNS and LES aided hybrid CAA methods are also studied. The various insights drawn in the previous chapter further influence the choice of specific numerical schemes, turbulence models, sub-grid length scales, and other case-specific methods to enable an accurate prediction of the hydrodynamic field. In addition to this information, Chapter 4 describes the common numerical methods such as spatial and temporal discretization schemes; the FWH solver is outlined in brief, along with information about the associated input and output data files. Chapter 5 is begun by comparing the flow and noise data obtained for a simple laminar flow test case with the same from established approaches. Then, the focus is shifted to validating the unsteady aerodynamic data of the deep stall test case. In the process of validating the deep stall test case, the flow solution and statistical data are investigated to discern the right choice of the convective scheme and SGS length scale for the surface pressure fluctuations. The obtained stall noise predictions are analyzed, after which the chapter is concluded by probing the flow and noise data obtained for the TBL-TE noise test case. Lastly, the outcome of the work, potential remedies for the pitfalls, and further points of

investigation are summarized in Chapter 6.

2 LITERATURE SURVEY

This chapter concerns the various reference literature consulted to derive insights on CAA and the associated methodologies, following which airfoil self noise, the relevant contributors for the same, and the underlying physical phenomena are reviewed in brief. In conjunction with this, the findings from the application of high-fidelity simulation methods for airfoil aerodynamics and aeroacoustics are discussed. Finally, the turbulence modeling approaches and the relevant sub-grid length scales considered in this study and their significance on the flow solution are given.

2.1 Computational Aeroacoustics

Computational aeroacoustics deals with the use of numerical methods to determine and analyze flow-induced noise. The problems posed on the accurate prediction of aerodynamic noise are the issues of length scale disparity, simulation of unbounded domains, energy disparity, and acoustic inefficiency [25]. Conventional CAA methods only address a particular combination of these issues and not comprehensively. The schematic classification of existing CAA methods is shown in figure 2.1. The direct and hybrid methods are relevant to the current study. They differ based on the extent of the simulation domain, nature of computational mesh, and employed numerical schemes.

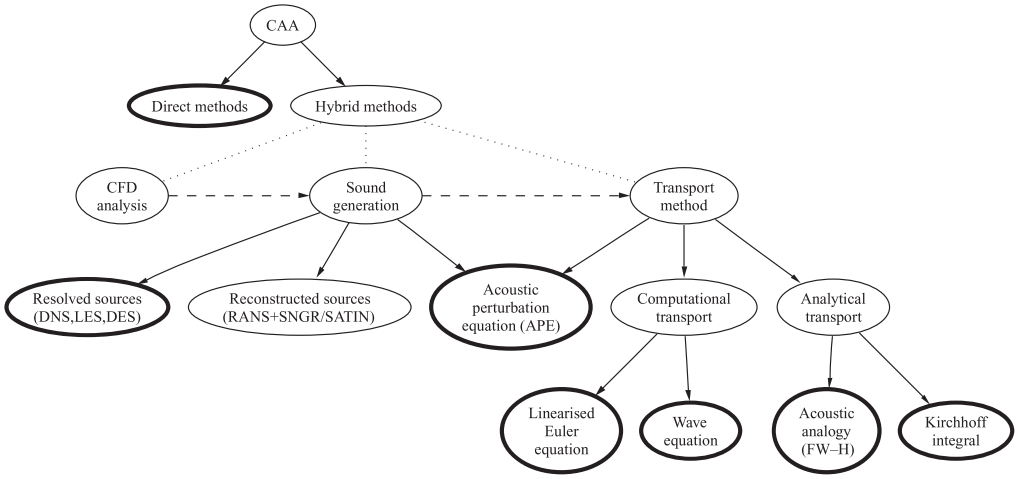

Figure 2.1: Classification of CAA approaches [1]

2.1.1 Direct Method

The direct method refers to the approach in which both flow and noise fields are computed simultaneously. The domain encompasses the source and extends to the region of interest in the near or far-field. The direct method thus requires a grid that can spatially resolve both the flow and noise fields. Given the disparity in scales of the flow and acoustic phenomena in practical problems, besides the requirement of long run times, it demands an inordinate amount of

computational resources, limiting its applicability to low Reynolds number simple flow configurations [26]. This method of CAA also requires complex discretization schemes as traditional schemes used in CFD simulations have high dispersion and diffusion errors and are tuned to attenuate spurious waves, which will prove detrimental to the radiation of the sound to the far-field [1].

Furthermore, the turbulence resolving approach used also impacts the nature of the acoustic field. By using Direct Numerical Simulation (DNS), the acoustic field is obtained as a consequence of all the flow scales. Whereas, with Large Eddy Simulation (LES), the acoustic field obtained is generated only by the dynamics that have been captured.

2.1.2 Hybrid Method

In the hybrid approach, the unsteady near-field flow and the acoustic solution is computed with the help of a CFD approach. The sound generated at the source in the near-field is then concurrently transported to the observer in the far-field by employing computational modeling or analytical acoustic transport equations.

Computational transport methods refer to the case where the equations for acoustic transport are discretized on a grid external to the CFD source grid. Transport equations, such as the linearized Euler equations or the wave equation, are solved, which are relatively simpler than those solved in the CFD domain.

In the analytical hybrid CFD-CAA approach, an acoustic analogy is used. It involves an integral formula derived as an analytical solution of the governing acoustic transport equation, such as the Lighthill's [27] or Ffowcs-Williams and Hawkings (FWH) equation [28]. The noise at the observer in the far-field is obtained by computing a surface integral comprising specific source terms. The surface considered for integration can either be the surface of the object immersed in the fluid or a particular surface that is chosen such that all physical phenomena that contribute to the noise at the observer in the far-field are included. In a few scenarios, volume integration of specific source terms in the domain external to the integration surface must be carried out because of the relevance of quadrupole sources.

FWH, Kirchoff, and Lighthill's integral solutions are the most widely used integral methods with scale resolving simulations. The FWH acoustic analogy is explained in detail in the following section.

2.2 Ffowcs Williams and Hawkings Acoustic Analogy

As described earlier, the FWH acoustic analogy involves computing a surface integral on a specific data surface to obtain the acoustic information at the observer in the far-field. Hence, it is also commonly referred to as the FWH integral equation. The ambient medium in which the sound propagates is hypothesized to be at rest. The FWH integral equation is the solution of the FWH acoustic transport equation given by equation 2.1 theorized by Ffowcs-Williams and Hawkings in their seminal article [28]. It extends Lighthill's acoustic analogy to make it applicable to moving surfaces.

$$\begin{aligned}\frac{\partial^2\left(\rho' H_s\right)}{\partial t^2} - c_\infty^2 \frac{\partial^2\left(\rho' H_s\right)}{\partial x_i^2} =& \frac{\partial^2\left(T_{ij} H_s\right)}{\partial x_i \partial x_j} - \frac{\partial}{\partial x_i}\left(\left(\rho v_i\left(v_j - V_j\right) + p_{ij}\right) n_j \delta(f)|\nabla f|\right) \\ &+ \frac{\partial}{\partial t}\left(\left(\rho v_j - \rho' V_j\right) n_j \delta(f)|\nabla f|\right)\end{aligned} \tag{2.1}$$

The above equation considers the generalized variables of velocity $\mathbf{v}H_s$, pressure pH_s, and density ρH_s that are defined throughout the bounded CFD and unbounded CAA domains shown in the figure 2.2. Here, $H_s(f)$ refers to the Heaviside step function, $\delta(f)$ is the Dirac delta

function, both of which are functions of the shape function *f* of the FWH data surface, **n** is the unit outward normal to the FWH data surface, and **V** is the velocity of the data surface Γ_p.

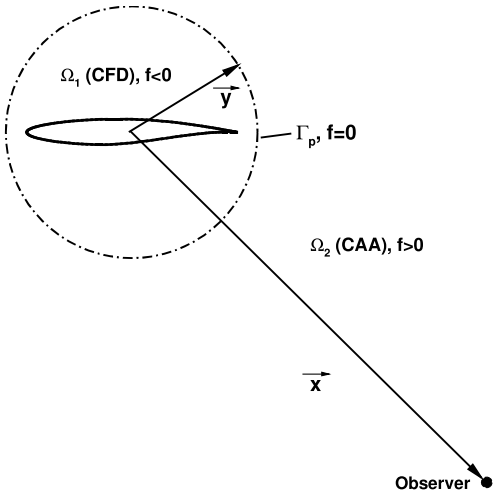

Figure 2.2: The permeable FWH surface [2]

The time-domain solutions derived by Di Francescantonio [29] and Farassat [24] and frequency domain solutions of the FWH equation are widely used for noise predictions. The time-domain integral FWH solution does not require a Green's function customized to the flow geometry as a more generalized free-field Green's function is used to obtain the solution enabling the treatment of arbitrarily shaped data surfaces. The integral formulation [4] is as shown below.

$$\rho'(\mathbf{x},t)c_\infty^2 H_s = \frac{\partial^2}{\partial x_i \partial x_j}\int_{\Omega_2}\left[\frac{T_{ij}}{4\pi r\left|1-M_r\right|}\right]_{\tau=\tau^*} dV(\mathbf{z}) \quad -\frac{\partial}{\partial x_i}\int_{\Gamma_p}\left[\frac{\left(\rho v_i\left(v_j-V_j\right)+p_{ij}\right)n_j}{4\pi r\left|1-M_r\right|}\right]_{\tau=\tau^*} d\Gamma + \frac{\partial}{\partial t}\int_{\Gamma_p}\left[\frac{\left(\rho v_j-\rho' V_j\right)n_j}{4\pi r\left|1-M_r\right|}\right]_{\tau=\tau^*} d\Gamma \tag{2.2}$$

The emission and observer times are given by τ and *t* respectively, coordinate ***z*** represents the moving coordinates of the FWH data surface and is the same as ***y*** at the emission time τ_o and when the data surface is stationary, *r* is the magnitude of the radiation vector $r = |\boldsymbol{x}-\boldsymbol{y}|$ from the data surface to the observer, M_r is the Mach number of a moving point on the FWH surface in the radiation direction ***r***, v_j and V_j are the components of velocity of the local fluid velocity at the FWH surface and the velocity of the FWH surface respectively, n_j is the component of the unit surface normal at a given point on the FWH surface, T_{ij} is the Lighthill's stress tensor given by equation 2.4, $p_{ij} = (p-p_\infty)\,\delta_{ij} - \sigma_{ij}$ is the compressive stress tensor, c_∞ the speed of sound in the ambient medium and τ^* is the corrected retarded time defined as follows:

$$\tau^* = t - r\left(\tau^*\right)/c_\infty \tag{2.3}$$

$$T_{ij} = \rho v_i v_j + (p-p_\infty) - (\rho-\rho_\infty)\,c_\infty^2\delta_{ij} - \sigma_{ij} \tag{2.4}$$

The first term in equation 2.2, represents the quadrupole term to which the Lighthill stress tensor is the sole contributor. It accounts for the noise generated by turbulence and flow distortions. The second integral is the dipole source term which includes the contribution from the loading on the data surface. The third is the volumetric displacement term, often referred to as the thickness or monopole term. As volume integrals are expensive to compute, the

FWH surface is usually located such that it encloses all the noise sources (monopole, dipole, and quadrupole), making it feasible to ignore the volume integral. Farassat [24] further ignores the shear forces on the FWH surface and arrives at equation 2.5, which is widely used for aerodynamic noise predictions.

$$\begin{aligned} 4\pi p'(\vec{x},t) = & \int_{\Gamma_p} \left[\frac{\dot{Q}_n}{r\left(1-M_r\right)^2} \right]_{\tau=\tau^*} dS + \int_{\Gamma_p} \left[\frac{Q_n c_\infty \left(M_r - M^2\right)}{r^2\left(1-M_r\right)^3} \right]_{\tau=\tau^*} dS \\ & + \frac{1}{c_\infty} \int_{\Gamma_p} \left[\frac{\dot{L}_r}{r\left(1-M_r\right)^2} \right]_{\tau=\tau^*} dS + \int_{\Gamma_p} \left[\frac{L_r - L_M}{r^2\left(1-M_r\right)^2} \right]_{\tau=\tau^*} \\ & + \frac{1}{c_\infty} \int_{\Gamma_p} \left[\frac{L_r\left(M_r - M^2\right)}{r^2\left(1-M_r\right)^3} \right]_{\tau=\tau^*} dS \end{aligned} \tag{2.5}$$

$$Q_n = \left(\left(\rho_0 - \rho\right) V_i + \rho v_i\right) \hat{n}_i \tag{2.6}$$

$$L_i = \left[P_{ij} + \rho v_i \left(v_j + V_{0j}\right)\right] \hat{n}_j \tag{2.7}$$

In equation 2.5, $M_r = M_i \hat{r}_i, L_r = L_i \hat{r}_i, L_M = L_i M_i$ and $\dot{L}_r = \dot{L}_i \hat{r}_i$. Where M_i is the Mach number of the component of the local FWH surface velocity. The time derivatives are taken with respect to the emission time. The subscript p in Γ_p refers to a permeable data surface. However, solid surfaces can also be used in the 1A formulation; the surface of the object immersed in the fluid can also be used as the data surface, but such a consideration should be made only if the physics of the problem permits it. The insignificance of the quadrupole term in low speed and low Reynolds number flows allows for such a simplification. In that case, using a solid FWH surface reduces equation 2.5 further, as shown in the section 4.2.

The FWH analogy, although being computationally less demanding than direct methods, has a few drawbacks. As a few FWH integral approaches tend to neglect the contribution of quadrupole sources, it is necessary to have an initial idea of the underlying noise sources, such that the right choice of the integral solution is made. The FWH surface should be located in a region where there is confidence in obtaining an accurate solution devoid of any spurious reflections from the domain boundaries. The spurious reflections caused at the boundaries can be remedied by using non-reflecting boundary conditions or radiation boundary conditions at the domain boundaries. The spurious reflections can also be treated by appending the computational domain with an absorbing zone. The absorbing zone is an additional mesh where either an extra artificial dissipation term or adequate grid stretching is included. Passage of vortices through the FWH surface is manifested as non-physical waves; this can be avoided by either truncating the FWH surface in such a region or by using multiple end caps to average out the effect as suggested by Shur [30]. The mesh at the region of the FWH surface and the time resolution considered limits the maximum frequency that can be resolved in the grids, thus justifying the need for finer spatial resolution of the grid and temporal resolution for flow scenarios in which a broadband sound spectrum is to be expected. One of the inherent computationally demanding aspects of the FWH analogy approach is the computation of the radiation vectors; this, unfortunately, cannot be circumvented.

2.3 Aeroacoustics of Wind Turbines

Developments of noise mitigation technologies such as blade add-ons, blade tips, and turbine control schemes have been vital in maintaining low noise levels in modern wind turbines. Nevertheless, onshore wind turbines are rendered to operate at reduced power to cope with noise limit

regulations. The individual wind turbine noise mechanisms as per Bertagnolio and Fischer [23] correspond to:

- Turbulence inflow noise or leading edge noise
- Turbulent boundary layer - trailing edge noise
- Laminar boundary layer vortex shedding noise
- Stall noise
- Blunt trailing edge noise

2.4 Airfoil Self-Noise Mechanisms

The list of sources mentioned in the previous section entails all the airfoil self-noise mechanisms investigated experimentally by Brooks [8], wherein a parametric study of the NACA0012 with different span sizes and angles of attack ($0° - 25.2°$) is made. They state that leading edge noise can be efficient only when the leading edge is sharp compared to the scale of turbulence in the inflow and/or the inflow turbulent boundary layer.

2.5 Turbulent Boundary Layer Trailing Edge (TBL-TE) Noise

As depicted in the figure 2.3, trailing edge noise results from the interaction between the turbulent eddies present in the unsteady turbulent boundary layer convecting over the airfoil with the sharp trailing edge. The far-field noise spectra for TBL-TE noise is broadband in nature for fully turbulent attached flows [3]. It is one of the dominant sources of noise on a wind-turbine blade. Add-ons such as trailing edge serrations or metal foam trailing edges help mitigate noise emissions, although the former is the most widely used [23].

2.5.1 Analytical models for TBL-TE predictions

At low Mach numbers, the turbulent eddies in the vicinity of a sharp edge are efficient noise sources as per Ffowcs-Williams and Hall [31]; they relate the far-field sound spectra to the properties of flow, streamwise turbulence velocity, and the length scale of turbulence present in the flow. Applying the theory of Ffowcs-Williams and Hall to the TBL-TE problem results in the scaling of the trailing edge noise to the fifth power of the flow velocity.

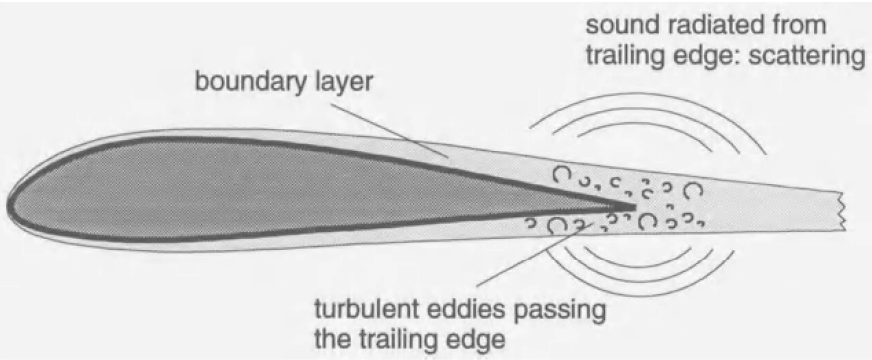

Figure 2.3: Turbulent Boundary Layer Trailing Edge Noise [3]

As mentioned earlier, Brooks, Pope and Marcolini (BPM) [8] developed a semi-empirical model that was derived by curve fitting the noise data obtained from a series of wind tunnel experiments covering the different noise mechanisms, albeit for a symmetric airfoil. In the BPM model, the total trailing edge noise is constituted of the contributions from the suction side and pressure side boundary layers and the angle of attack. Each of the contributions is in the form of a spectral curve that is a function of the chord-based Reynolds number (Re), Mach number (M), boundary-layer displacement thickness (δ^*), angle of attack (α), and a spectral function.

Another widely used analytical model is that developed by Amiet [32], who uses an iterative procedure along with Schwarzschild's technique to obtain an analytical solution of the canonical Helmholtz's equation to which the zero-potential, no penetration boundary conditions, and the Kutta condition are applied. The result was an expression for the autospectral density of the far-field acoustic pressure that depends on the turbulent boundary layer's turbulence statistics and the airfoil response function. The drawback of this model is that it is derived for the case of flow on a flat plate with the flow being aligned with the chord.

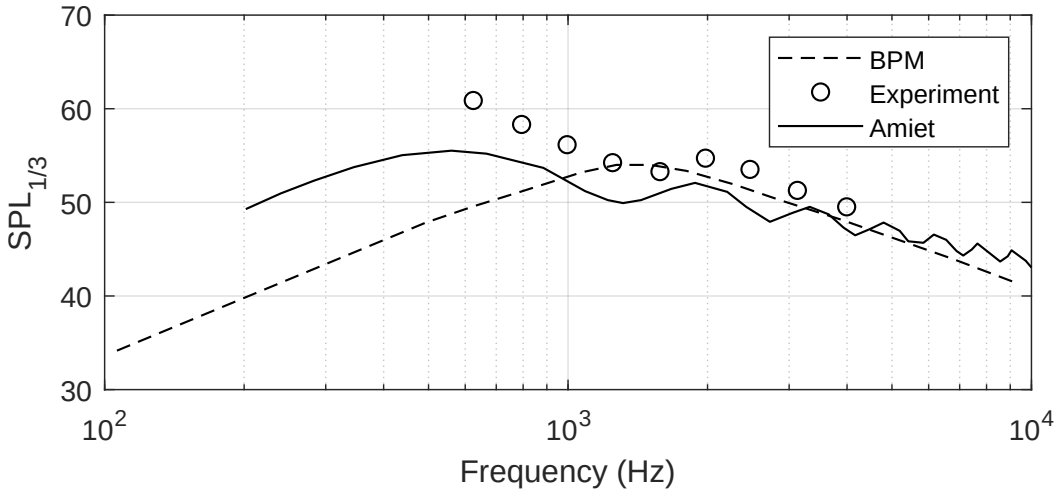

Figure 2.4: Comparison between TBL-TE noise spectra predictions from the BPM model and Amiet's theory [4]

Figure 2.4 [33] is a plot comparing the one-third octave noise spectra between an experiment, the BPM model, and Amiet's theory for an observer located on the mid-span in the far-field of a NACA0012 airfoil at zero angle of attack and the chord-based Reynolds number 660000. It can be deduced from the figure that both the BPM model and Amiet's theory provide accurate predictions at high frequencies. But Amiet's theory fares well compared to the BPM model at low frequencies by underpredicting the sound pressure level by 5 dB, whereas the discrepancy is much more in the BPM model. The reasons for underprediction are that Amiet's theory considers a flat plate boundary layer in which the spanwise pressure length scale is low compared to that of the larger eddies produced in the vicinity of the trailing edge where an adverse pressure gradient is present. The erroneous prediction of the BPM model at low frequencies is attributed to the inherent difficulty in measuring trailing edge noise at low frequencies.

2.5.2 Computational predictions of TBL-TE Noise

Compared to the engineering models, high-fidelity CFD aided CAA provides a more detailed insight into the noise mechanisms. Various authors have investigated fundamental noise phenomena such as the TBL-TE noise in the purview of the design of low-noise profiles for wings, high-lift devices, wind turbine blades, and propellers. Wolf [5] investigated the far-field noise

data for the case of NACA0012 at $\alpha = 0°$, with a chord-based Reynolds number (Re_c) of 408000. The noise data was compared with the wind-tunnel experiments performed for the same flow configuration by Brooks [8]. The boundary layers on the suction and pressure sides were tripped in both the simulation and the experiment to avoid modeling the Laminar boundary layer – vortex shedding noise (LBL-VS) noise. The normalized wall pressure spectra were also compared with that obtained from experiments by Sagrado and Hynes [34]; this is shown in the figure 2.5. Here, $\Phi(\omega)$ is the one-sided pressure spectra $(\Phi(\omega)U_e/q_e^2\delta^*)$ that is scaled with the pressure scale $q_e = 1/2\rho U_e^2$ and the time scale δ^*/U_e. In figure 2.5a, and figure 2.5b, U_e refers to the edge velocity of the boundary layer, and δ^* refers to the boundary layer displacement thickness. The non-dimensional wall pressure spectra in the two studies agree with each other.

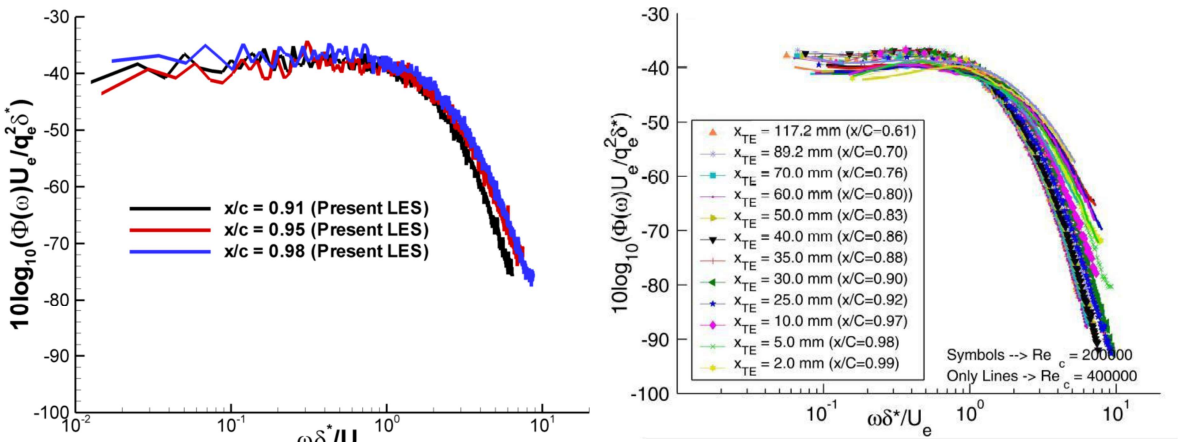

(a) From LES by Wolf [5] (b) From experiments by Sagrado and Hynes [34]

Figure 2.5: Comparison of normalized wall pressure spectra between LES study by Wolf and Sagrado's experiments

For the LES study, an O-grid mesh was created by using a blunt trailing edge of a certain thickness (h); however, this did not have a significant impact on the noise prediction as the bluntness factor $h/\delta^* \approx 0.3$ which was in accordance with Blake [35], who stated that vortex-shedding is observed for trailing edges with bluntness factor greater than 3. Nevertheless, a separation bubble was detected at the trailing edge, which was very small, and hence, it was only considered to have a weak impact; it is associated with the small secondary peak at Helmholtz number $kc \approx 11$ in the Sound Pressure Level (SPL) spectra plotted in the figure 2.6. The plot shows excellent agreement between the simulation and experiment in a range of frequencies. The effect of quadrupole sources in sound radiation is deemed negligible as the maximum discrepancy appears in the lower frequency range and amounts to 3dB, which can be ignored. A similar trend is found at different observer locations and the directivity plots at different Helmholtz numbers.

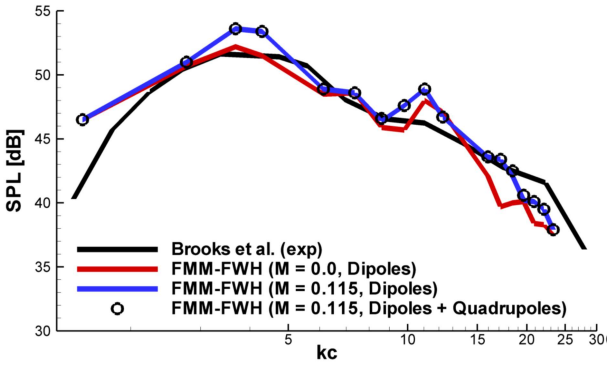

Figure 2.6: SPL spectra for an observer located in the far-field on the mid-span plane perpendicular to the chord [5]

Carpio [6] carried out an experimental study to investigate the cases of solid, permeable, and non-permeable metal foam trailing edge inserts shown in the figure 2.7. The case considered was a NACA0018 profile at $\alpha = 0°$, free-stream Mach Number M_∞ of 0.06 and a chord-based Reynolds number $Re_c = 280000$. The far-field noise spectrum at an observer located in the far-field generated by the permeable configuration exhibits a maximum attenuation of 11dB in the far-field noise in a range of frequencies up to a chord-based Strouhal number ($St = fc/U_\infty$) of 16, after which, a relative increase is observed from figure 2.8b; this is assumed to be produced by surface roughness as per figure 2.8b. The non-permeable configuration produces a far-field noise signature similar to the solid trailing edge configuration. It is proposed that cross-flow through the porous insert is responsible for noise attenuation and not the acoustically absorbent properties of the metal foam.

(a) Solid TE (b) Permeable TE (c) Non-permeable TE

Figure 2.7: Trailing edge configurations investigated experimentally by Carpio [6] and numerically by Teruna [7]

In a bid to ascertain the noise reduction mechanism in the permeable trailing edge configuration, Teruna [7] numerically investigated the previous cases by resolving the near-field with the Lattice-Boltzmann Method (LBM), and the acoustic propagation to the far-field was done with both the solid and permeable FWH formulations. As expected for low Mach number flows, there was no significant discrepancy between the SPL predictions from the two FWH methods, as shown in the far-field SPL plots in the figure 2.9. The spectra from the coupled LBM-FWH approach show good agreement with the experiments, except for the higher range of frequencies, whose discrepancy has been attributed to a different tripping mechanism used in the simulation (zig-zag tape). The same trend of attenuation for the permeable insert is observed in the plots of directivity in the lower frequencies where the source is compact. The smaller differences in the lower and higher frequencies in both the permeable and non-permeable configurations are speculated to be due to the neglected monopole and metal-foam surface roughness contributions. Furthermore, a beamforming approach identifies the region of maximum noise intensity near the trailing edge for the airfoils with solid and non-permeable inserts and the solid-porous junction for the airfoil with permeable insert.

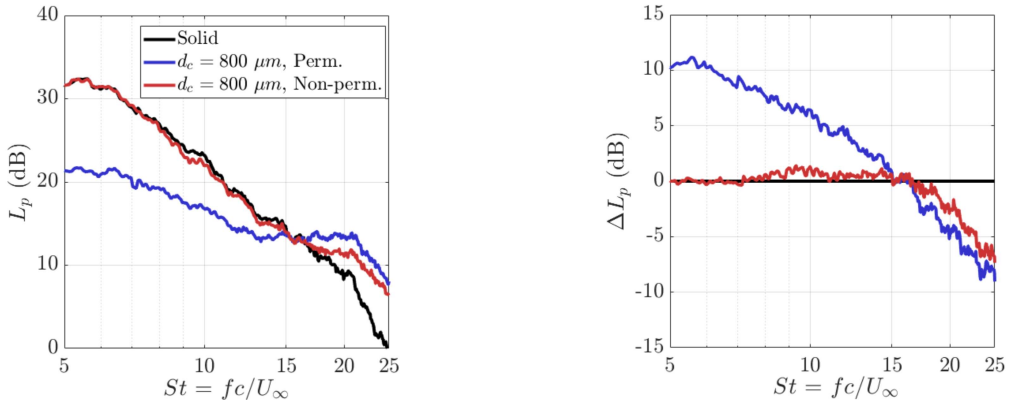

(a) Sound Pressure Level L_p spectra

(b) SPL relative to the solid TE ΔL_p

Figure 2.8: SPL spectrum at an observer located in the far-field on a plane perpendicular to the trailing edge and on the mid-span a) absolute values b)relative values with respect to the solid TE [7]

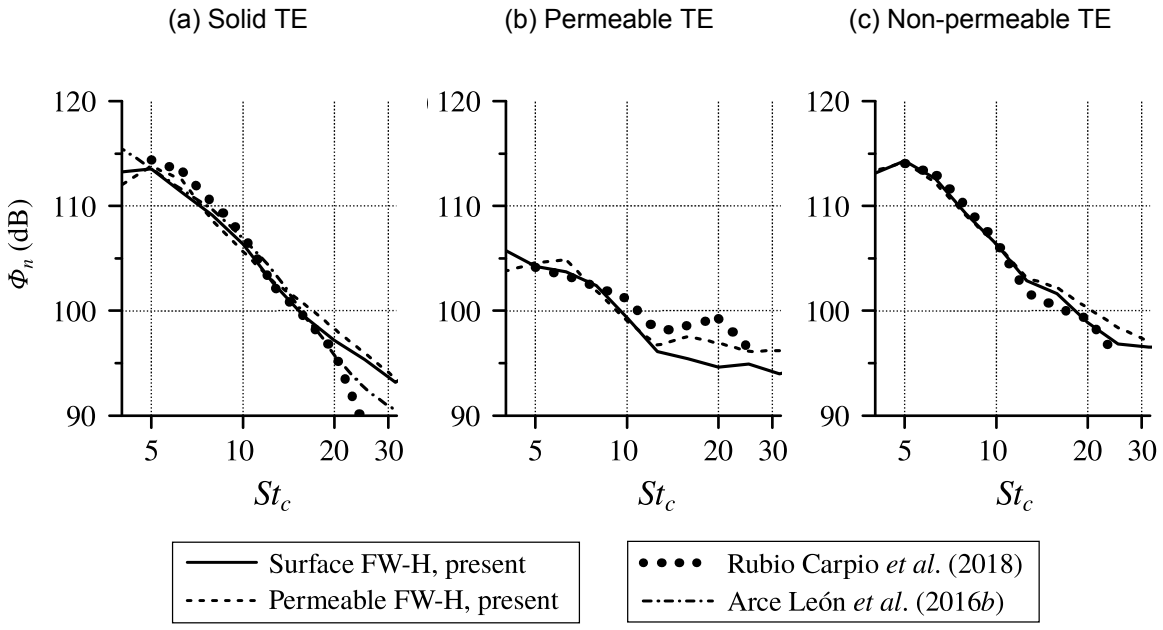

Figure 2.9: The normalized one-third octave spectra obtained for the different configurations at the far-field observer location by Teruna [7]

2.6 Separation-Stall Noise

In wind turbine blades, flow separation occurs at the blade's root due to thick airfoil sections. Stall-regulated turbines utilize stall to limit the power output. Unsteady phenomena such as gusts or wake-blade interaction also cause stall. Flow separation on airfoils due to an increase in the angle of attack causes an increase in the amplitude of the low-frequency sound. Brooks [8] noted an increase of more than 10dB relative to TBL-TE noise for the case of separation-stall noise. Paterson [36] investigated the noise produced by the interaction of stationary tip-vortex with a downstream airfoil; the far-field noise was found to be independent of the strength of the vortex. The airfoil's stalled region's surface pressure fluctuations were significantly larger than the same in the unstalled region. With the help of cross-correlation measurements between

the surface microphones and the far-field microphones for a mildly-separated flow, it was concluded that the noise is emitted from the trailing edge. However, with the airfoil in deep-stall, the dominant source of noise is the whole chord.

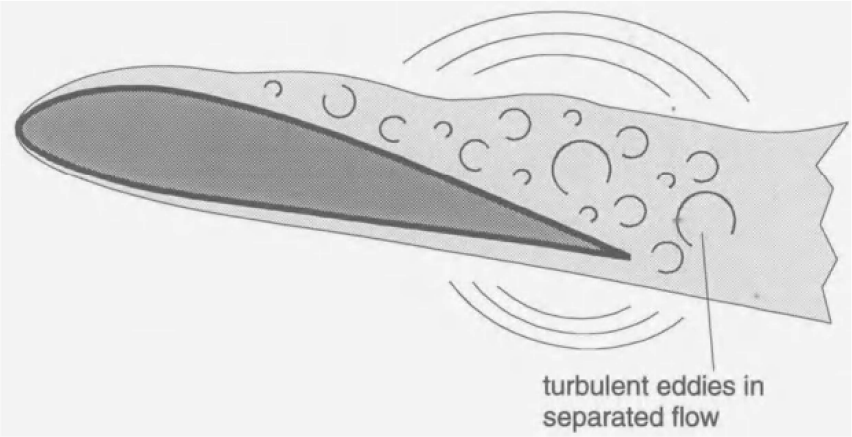

Figure 2.10: Separation Stall Noise [3]

2.6.1 Analytical models for separation stall noise

The semi-empirical noise model of Brooks [8] described in the previous section is also applicable for the case of separation-stall noise and provides accurate predictions. The prediction from the BPM model compare well with the experimental far-field noise data for conditions of high Reynolds number at low and moderate angles of attack as observed in one-third octave plots in the figure 2.4 and figure 2.11, unlike low Reynolds number flows involving massive separation (deep-stall) shown in the SPL plot in figure 2.12.

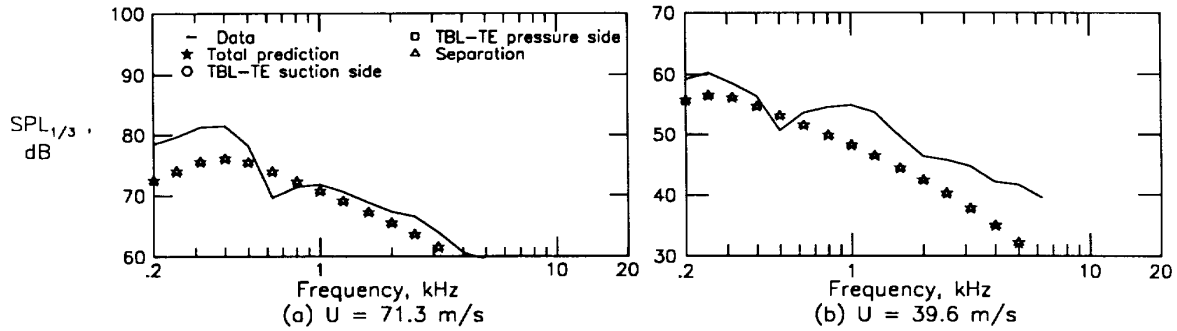

Figure 2.11: Self-noise spectra by the BPM model for NACA0021 airfoil with 10.16cm-chord and $\alpha = 15.6^{\circ}$ [8]

Moreau [9] carried out wind tunnel experiments of NACA0012 airfoils, flat plates, elliptic, and the cambered NACA65-(12)10 airfoils at high angles of attack. The chord-based Reynolds number (Re_c) was set at 1.5×10^5. An increase in the magnitude of the low-frequency noise was found. Two distinctive stall regimes were characterized, namely light stall and deep stall. The light-stall case has a broadband far-field sound spectrum but is marked by a low frequency peak. Whereas the deep stall regime consists of two distinct peaks in the lower frequency region and a high-frequency region having lower sound levels when compared to the light stall case. It was also speculated that one of the peaks in the spectrum for deep stall is due to confinement issues caused by the interaction between the nozzle jet and the oscillations

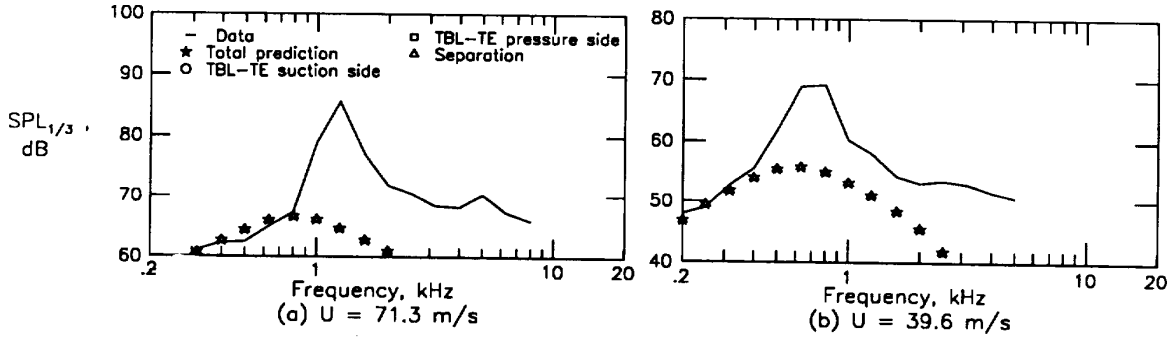

Figure 2.12: Self-noise spectra by the BPM model for NACA0021 airfoil with 2.54cm-chord and $\alpha = 22.2°$ [8]

in separated flow close to the airfoil. The far-field spectra plots in figure 2.13a and figure 2.13b correspond to horizontal and vertical configurations. The configurations are classified based on the ratio of the nozzle flow width W to the airfoil span L. The vertical configuration was expected to entail installation effects due to low relative flow width, the ratio of nozzle flow width W to the airfoil chord c.

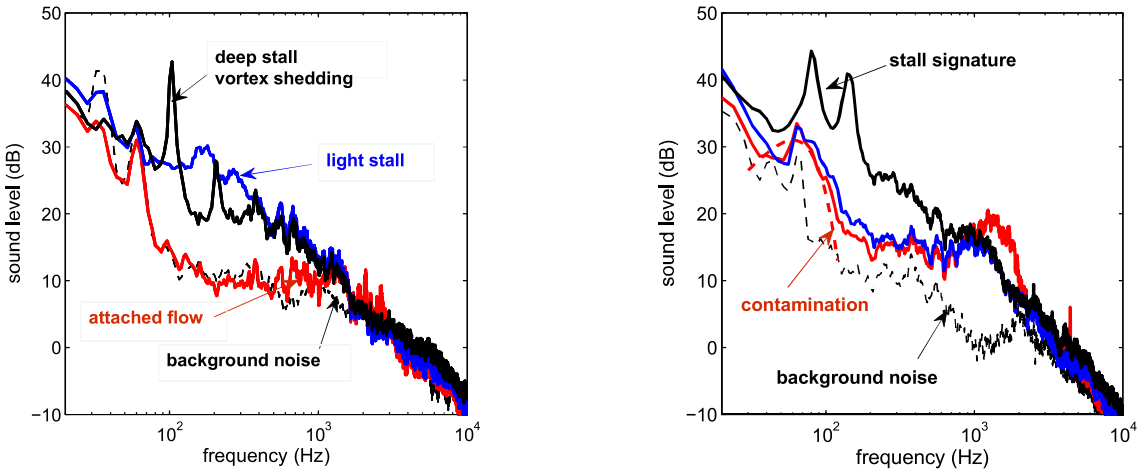

(a) $L = 13cm, c = 8cm, W = 30cm$ (b) $L = 30cm, c = 10cm, W = 13cm$

Figure 2.13: Far-field noise spectra for NACA0012 airfoils [9]. — $\alpha = 5°$; — $\alpha = 15°$; — $\alpha = 26°$

The analytical model proposed by Moreau [9] is based on Curle's analogy; the acoustic sources are assumed to be at the trailing edge. As the SPL spectra for the light and deep-stall configurations scale to the power 5 or 6, it is suspected to be a consequence of dipolar sources. Unlike the assumption of streamwise homogeneity in familiar TE-noise models such as the one proposed by Amiet [32], the low-frequency motions pertinent to stall are synonymous with large spanwise coherence length (l_y). As a result, Amiet's theory was deemed applicable for the high frequencies, and a new model was proposed for the lower frequencies [9]. The model is independent of the airfoil profile, relative flow width, and confinement ratios. The principal inputs taken are the spanwise wavenumber spectrum and separation bubble thickness, among others. Figure 2.14 is the plot of the experimental and model-based SPL spectra at an observer located in the far-filed and on the mid-span plane. The predictions agree with the experiment at lower frequencies and deviate at higher frequencies. It can also be observed that both the experimental and predicted spectra and the offset wall-pressure spectra collapse over a range of frequencies.

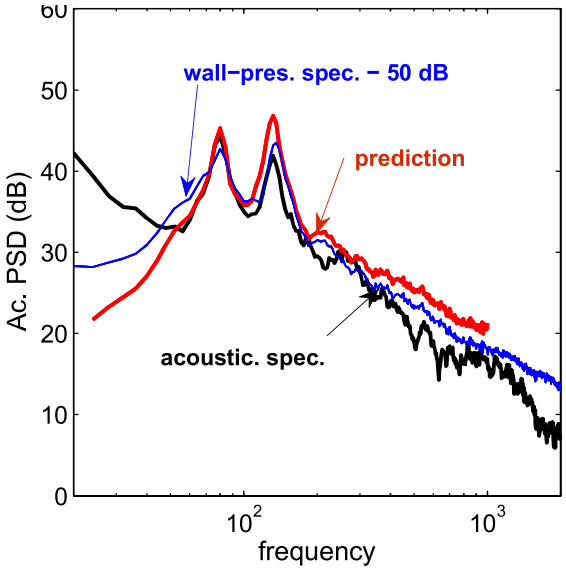

Figure 2.14: Comparison of SPL spectra between separation-stall noise model of Moreau vs experimental measurement [9]. — model; — wall pressure spectrum; — experiment

2.6.2 Computational predictions of separation stall noise

Getting reliable data from wind tunnel experiments for high Reynolds number flows with the airfoil at large angles of attack is challenging because of the tunnel flow deflections caused. Thus high-fidelity simulations are resorted to for investigating the acoustics during such situations. The case of separation-stall noise by a NACA0012 airfoil of span 0.5c at $\alpha = 15^\circ$ with the chord-based Reynolds number 250000 and Mach number of 0.2 was considered by Wolf [10]. Sharp leading edge separation with the boundary layer fully detached on the suction side was found to occur in the simulation. The integral force coefficients were overpredicted compared to the experiments investigating a similar configuration. As wall pressure fluctuations were correlated throughout the span, large span sizes of 1c and 2c were investigated. The drop in spanwise correlation was deemed acceptable in the 2c case alone. The solid surface variant of the FWH integral formulation given in equation 2.5 was used to project the acoustic data to the far-field. The resulting spectra at the far-field observer located on the mid-span plane and 24c away from the trailing edge are plotted in figure 2.15. The far-field spectrum for one of the NACA0012 cases tested by Brooks [8] is also included for comparison. It is seen that the sound is overpredicted across the whole range of frequencies, especially the relevant low-frequency noise.

Turner [11] investigated the acoustic field of a NACA0012 airfoil at angles of attack 5°, 10°, and 15° with a low Reynolds number of 50,000 and a Mach number of 0.4. The solid surface FWH formulation was used to extrapolate the surface pressure fluctuations to the far-field; this means that the considered sound sources were dipole, which is relevant to the low-frequency stall noise. For the $\alpha = 5^\circ$ case, the flow separates at $x/c = -0.4$ and reattaches at $x/c = 0.1$. The flow for the $\alpha = 10^\circ$ separates at the leading edge and reattaches at $x/c = -0.225$ due to the transition of the separated shear layer to turbulence through the Kelvin-Helmholtz (KH) instabilities. The airfoil is fully stalled at $\alpha = 15^\circ$ with the presence of large-scale vortex shedding in the wake. The plot of the obtained normalized sound power at ten chord lengths away from the airfoil mid-chord $(x = 0)$ is given in figure 2.16. It is observed that there exists an increase of the sound power in both the $\alpha = 10^\circ$ and 15° with respect to the $\alpha = 5^\circ$ case, with the shedding peak at the chord-based Strouhal number $St = 0.75$. For medium frequencies $(1.5 < St < 10)$, the sound power is comparable amongst all the configurations. Finally, it is interesting to note the broad-band increase in sound power of the $\alpha = 10^\circ$. It is speculated that the increase might

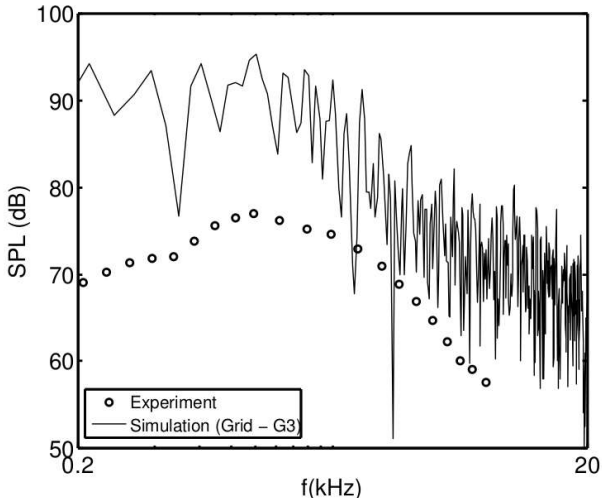

Figure 2.15: Far-field SPL spectrum comparison between experiment and LES [10]

be due to the scattering of wake quadrupole noise at the trailing edge or scattering from the separated shear layer at the leading edge. This speculation is further driven by the increase in noise signature for the $\alpha = 10°$ case in the directions $\theta = 120°$ and $\theta = 230°$, with $\theta = 0°$ being aligned with the chord line.

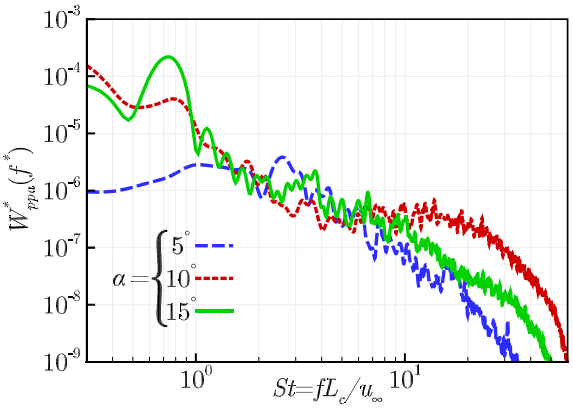

Figure 2.16: Normalized sound power in the far-field at ten chords away from the airfoil mid-chord [11]

The normalized sound power W_{ppa} in the previous figure is calculated by integrating the one-sided PSD of fluctuating pressure (S_{ppa}) between two observer angles θ_1 and θ_2. Its expression is given by the equation 2.8; where, R refers to the distance between the observer and airfoil mid-chord, b is the span of the surface considered for the acoustic source integration, and ρ_∞ and a_∞ are the density and the speed of sound in the far-field.

$$W_{ppa}\left(\theta_1, \theta_2, f\right) = \frac{Rb}{\rho_\infty a_\infty} \int_{\theta_1}^{\theta_2} S_{ppa}(\theta, f) d\theta \tag{2.8}$$

Turner [11] also investigated the sources on the airfoil relevant at specific frequencies; for this, the amplitude of fluctuations was visualized by plotting the contours of the magnitude of the solid surface FWH loading term's Fourier transform $|L_w|$ on the airfoil's suction surface. The phase variation of the source pressure fluctuations is visualized by plotting the imaginary part of L_w, i.e., $|L_w| \sin(\phi)$. The corresponding plots are depicted in figure 2.17a, and figure 2.17b.

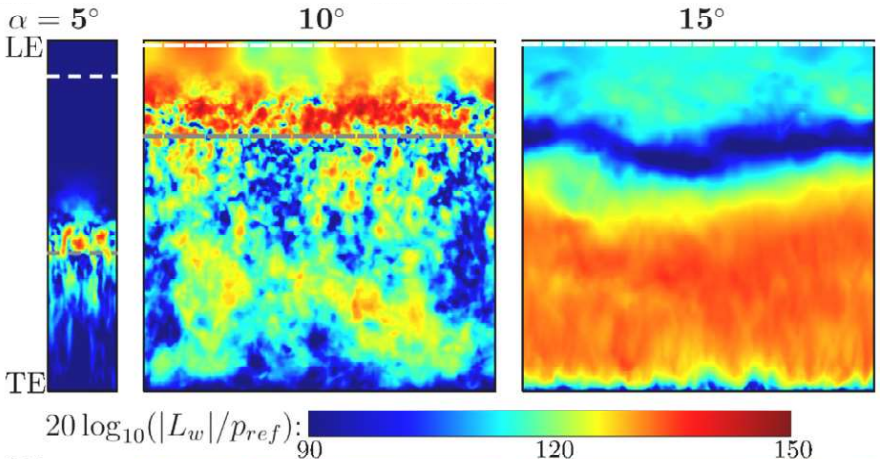

(a) Fourier transform magnitude. $p_{ref} = 10^{-10}p_\infty$

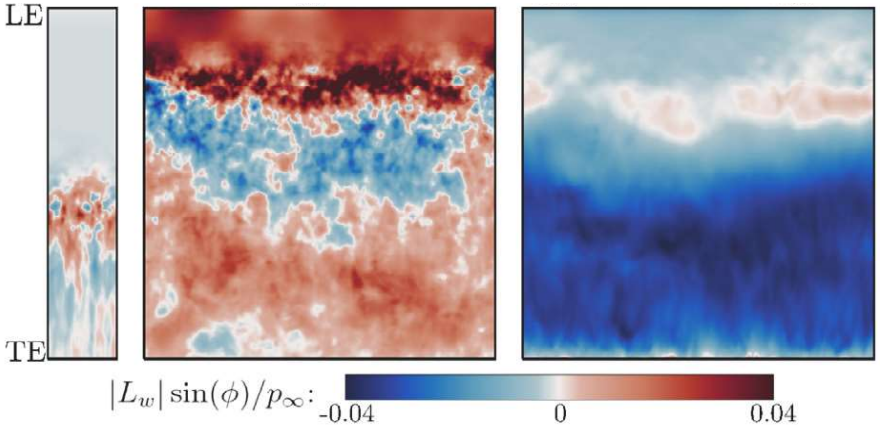

(b) The imaginary part of the Fourier transform

Figure 2.17: Amplitude and phase variation on the airfoil's suction side surface at $St = 0.75$ [11] with the observer at $\theta = 90°$ and ten chord lengths away from the mid-chord

The magnitude of the Fourier transform is an indicator of the source strength. At the shedding peak frequency $St = 0.75$, figure 2.17a indicates high values of source strength in the region aft of the quarter chord line for the fully-stalled airfoil; these sources are also in phase as per the phase contour in figure 2.17b. This observation is consistent with earlier literature and explains the peak obtained at this St in the far-field. The high source strength is surmised to be a consequence of the vortex shedding in the wake. In the $\alpha = 5°$ and $\alpha = 10°$ cases, source strengths are highest at the region where the boundary layer reattaches.

Furthermore, the airfoil at $\alpha = 10°$ has a high source strength just upstream of the boundary layer detachment line due to the KH instabilities. The broadband sound spectra, in this case, is comparable to the fully-stalled airfoil because of the presence of an in-phase source region that covers a major part of the airfoil's suction side, unlike the airfoil at $5°$ angle of attack that has a high-source strength concentrated on a very small portion of the airfoil surface. Through similar analyses, the fully-stalled configuration is observed to have a more in-phase source distribution relative to the other two cases due to the spanwise coherent structures shed during stall, even though there is a gradual decrease in spanwise coherence with increasing frequency. The nature of the acoustic sources in the $5°$ and $10°$ are such that the acoustic source strengths increase with increasing frequency, however with a larger variation in phase, except for the case of the high-frequencies where the acoustic sources at the leading edge for the airfoil at $\alpha = 10°$ are in-phase, thus causing an increase in the sound power.

In addition to the above, frequency-filtered acoustic pressure was plotted, which de-

picted the vortex street shed in the fully-separated wake causing the emission of dipole pulses when incident on the trailing edge. A strong pressure signature is also impressed on the wall due to the strength of the shed vortices. At higher frequencies, the vortices gradually weaken once they convect away from the wall, and thus only the vortices shed at the trailing edge would have more prominence in scattering the noise from the trailing edge. At the highest frequencies, it has been observed from the interference pattern for the full-stall case that quadrupole sources may be of significance. However, the study by Turner was done for flows of moderate Mach number $(M = 0.4)$. The same may not hold for the current study involving low Mach number flows $(M \leq 0.1)$.

2.7 Airfoils in Deep Stall

The NACA0021 airfoil in deep stall is considered in this study as it is one of the benchmark cases for validating high-fidelity turbulence resolving approaches for massively-separated flows. Furthermore, a detailed experimental study of this airfoil in deep stall by Swalwell [13] is one of the driving factors for the same. The following sub-sections provide a brief description of flow physics of deep stall followed by critical experimental findings, insights on and from numerical analyses available in the literature.

2.7.1 Flow Physics

Deep stall is an unsteady phenomenon involving massive separation on the airfoil's suction side characterized by regions of high recirculation on the suction side and a separation bubble extending beyond the trailing edge. Flow incident on the airfoil causes the shear layer to separate, roll up, and leads to the alternating shedding of vortices at the leading and trailing edges. The shed vortices have high values of coherence along the spanwise direction, although the spanwise extent of the geometry influences it. Wave-like instabilities in the separated shear layer such as the Kelvin-Helmholtz instability develop, causing its transition to turbulence. Figure 2.18 is a contour plot of vorticity obtained from a comprehensive DES study pursued by Mockett [12]. The shear layer roll-up at the trailing edge can be observed along with the diminishing vortex street in the far wake. A wide range of turbulent scales is present in the near wake. Furthermore, in reality, many turbulent scales are also present in the far wake but are not depicted here due to the mesh that gradually coarsens away from the near wake, limiting the scales that are resolved.

The coherent structures and instabilities are also prominent noise mechanisms in separation-stall noise along with shear layer flapping, as mentioned by Lacagnina [37].

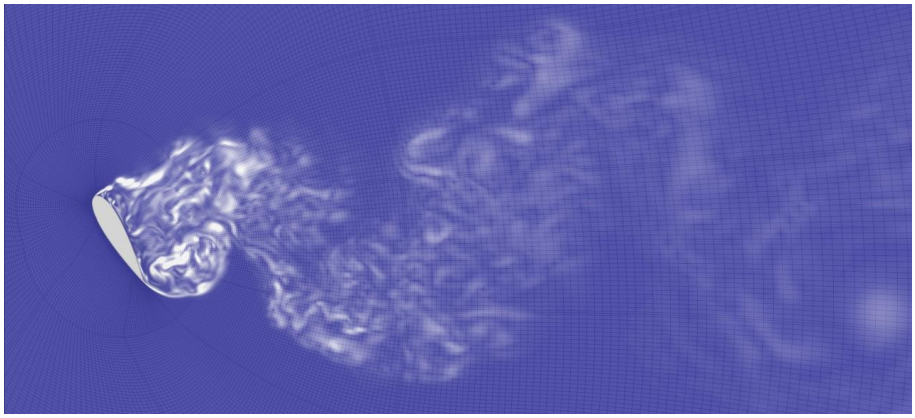

Figure 2.18: Plot of vorticity magnitude depicting the flow field associated with deep stall [12]

2.7.2 Prior Experimental Work

Very few experiments have been conducted for the deep stall test case because of difficulty getting reliable data due to the nozzle jet interaction with the airfoil at high angles of attack. The time-averaged integral lift $(\overline{C_l})$ and drag coefficients $(\overline{C_d})$ from experiments were provided by Hoerner [38]; for the airfoil at $\alpha = 60°$, these values are 0.91 and 1.65, respectively.

Swalwell conducted wind tunnel experiments on the profiles of NACA0021, NACA4421, and the S809 airfoils to determine the effect of turbulence intensity on the stall of these airfoils used in wind turbine blades [13]; an extensive database for the high angle of attack cases regarding their time histories of the integral coefficients and the surface pressure spectra was generated. The unsteady surface pressure data was recorded for the NACA0021 profile for a range of angles of attacks $0° \leq \alpha \leq 90°$ [39]. An airfoil of 12.5cm chord was used, and the span was 7.2c. The incident flow at a freestream Mach number of 0.1 resulted in a chord-based Reynolds number of 2.75×10^5. The arrangement of the pressure taps on the airfoil section is shown in figure 2.19b. It was found that the primary shedding frequency (f) of the integral lift and drag in terms of Strouhal number remains nearly constant with respect to the angle of attack when the width of the chord normal to the freestream is used as the length scale, $St = fcsin\alpha/U_\infty$.

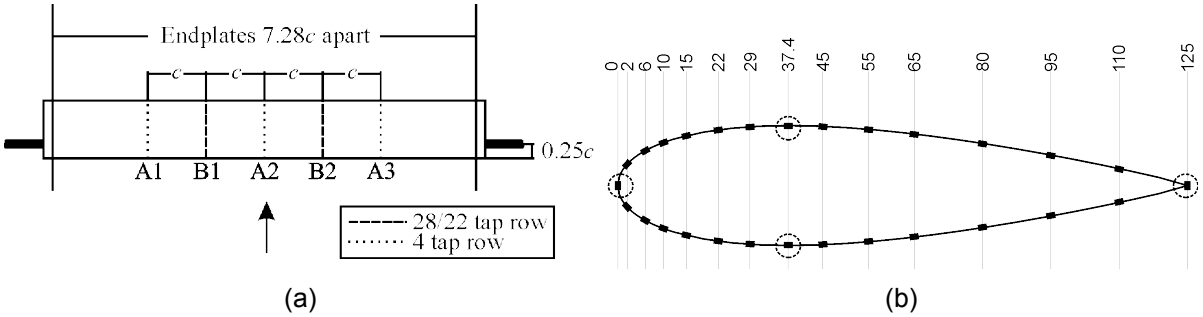

Figure 2.19: Tapping locations along airfoil cross-sections from Swalwell's experiment [13]

For the NACA0021 airfoil at $60°$ angle of attack, the time-varying integral coefficients of lift (C_l), drag (C_d), normal (C_n), and tangential (C_t) are plotted in figure 2.20. The values of the coefficients are determined by integrating the pressure data from one of the tapped rows B1 or B2. It was observed that there is difficulty in discerning the shedding process from the plots of C_l or C_d. However, plotting C_t, the shedding process was quite evident as it corresponded to the presence of beats in the C_t signal. It was reasoned that the vortex shed at the leading edge alone influences the tangential force. Hence would contain one frequency, making it more distinguishable; nonetheless, due to inherent three-dimensional effects, the shedding process was deemed aperiodic.

2.7.3 Numerical Findings

One of the first studies to have applied Detached-Eddy Simulation (DES) for the case of an airfoil in deep stall was by Shur [15]. A NACA0012 profile at an angle of attack of $45°$ with chord and span of 1m and the chord-based Reynolds number 10^5 were considered. For comparison, the same case with Unsteady Reynolds-Averaged Navier Stokes (URANS) and 2D DES was also investigated. By plotting the vorticity contours (ω_z) at certain spanwise locations as shown in figure 2.21, it was evident that scales smaller than that of the order of c were resolved. In contrast, URANS was only capable of resolving large quasi-2D eddies. Unlike URANS, the three-dimensional nature of the vortices was also captured in the DES simulation. The time-averaged integral coefficients and the surface pressure distribution matched the experiment excellently for the deep stall case. Additional investigations of the airfoil at angles of attack $8°$

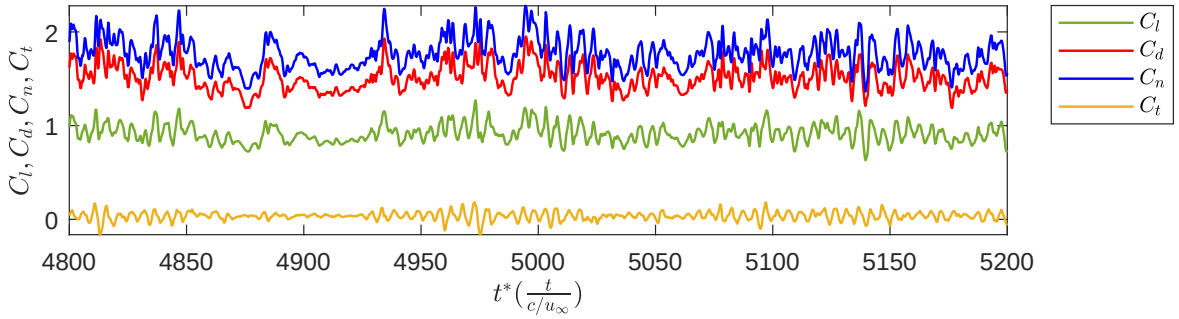

Figure 2.20: Time variation of experimental lift, drag, normal and tangential force coefficients [13]

and 20° were also conducted; where it was found that at $\alpha = 8^\circ$, DES essentially behaved like URANS, which did provide a good estimate in comparison with the experimental results. It was also found that 2D DES failed as it provided lift and drag estimates which were overpredicted by 70% in comparison with the experiments.

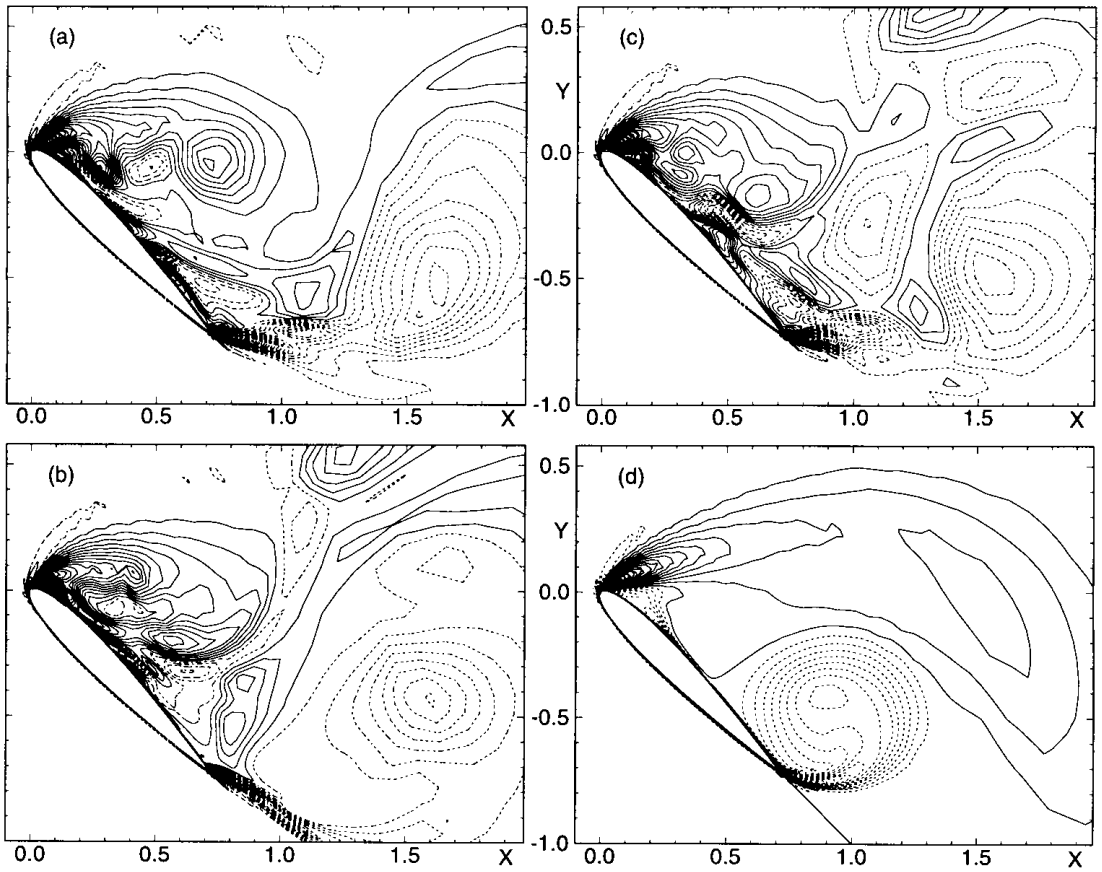

Figure 2.21: Plots of vorticity ω_z at spanwise z/c sections of (a)0.25, (b) 0.5 and (c)0.75 predicted by DES97 [14] and with (d) 3D URANS [15]

The FLOWMANIA research project [40] involved the NACA0012 in deep stall as one of the test cases. Angles of attack from 0° to 90° were explored, with both URANS and DES. From the DES results of the NACA0012 at $\alpha = 60^\circ$, it was noticed that the vortex shedding process was not regular, and between the vortex roll-up and separation at the leading and trailing edges, the flow remained in a state involving intermediary structures, that persisted for a longer time.

It was also shown that the URANS case resulted in a deterministic lift signal, unlike the same from DES. The same is observed by Zhang [16], who used the Spalart-Allmaras (SA) in both URANS and DDES. The plots of time-varying lift and drag coefficients for both SA-based RANS and DDES are shown in figure [16]. This figure shows that the lift and drag signals for the DDES simulation do vary stochastically.

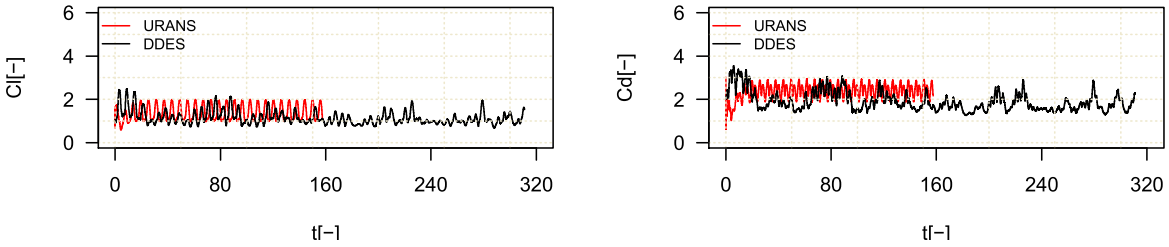

Figure 2.22: Time variation of spanwise averaged lift and drag signals [16]

Owing to the availability of a vast experimental database for NACA0021 in deep stall, the NACA0021 at $\alpha = 60°$ was one of the test cases considered in the DESider project [41]. The various participants considered different span sizes, URANS, and DES turbulence modeling approaches. Based on a running-average plot of the lift coefficient, it was observed that long time samples were required to obtain reliable values of lift coefficient. The flowfield's highly unsteady three-dimensional nature was dependent on the span size considered. The spanwise averaged Power Spectral Density (PSD) magnitude (figure 2.23) of the sectional lift of the span $4c$ agreed well with the experiments, whereas the $1c$ case overpredicted the PSD magnitude at frequencies lower than the primary shedding frequency; The $2c$ span was found to intermediary to these two. The non-dimensional frequency considered here was the chord-based strouhal number $St = fc/U_\infty$. Interestingly, the spanwise averaged surface pressure coefficient plots shown in figure 2.24 for the $1c$ case agreed better with the experiment than the $4c$ span. The effect of the underlying RANS turbulence model was found to have no prominent effect on the results.

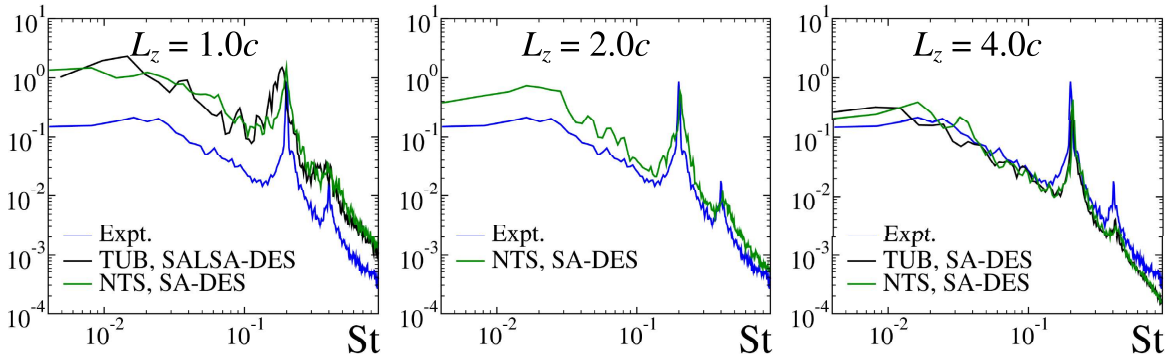

Figure 2.23: Effect of span sizes on the PSD magnitude [17]

Two-point spanwise correlation of u, v and w components of velocity were plotted by Garbaruk [17] at different locations in the suction side wake of the $1c$ and $4c$ spans. For the $4c$ airfoil, u and v components had consistently lower correlation values than the $2c$ airfoil, whereas the component w had the opposite trend.

As a validation effort to inspect the applicability of the shear-layer adapted length scale (Δ_{SLA}) [42], Guseva [18] conducted the SA-based DDES simulation of the NACA0021 at $60°$ with a span of $4c$. The solution from the standard DDES, which utilizes the grid-based length

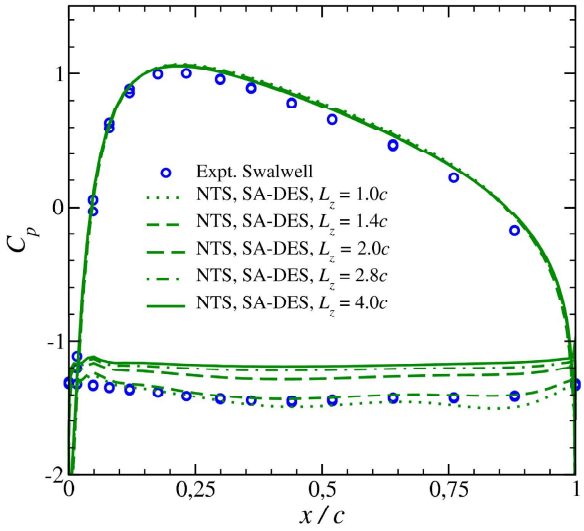

Figure 2.24: Effect of span size on surface pressure coefficients [17]

scale (Δ_{max}) and (Δ_{SLA}), were compared. The modified length scale was predicted to be a fraction of the standard DDES length scale near the leading and trailing edge separation regions; this caused the reduction of eddy viscosity in these regions shown in the figure 2.25. The decrease accelerated the roll-up of the separated layer but did not change the wake shape comprehensively, thus resulting in a similar statistical result as in standard DDES.

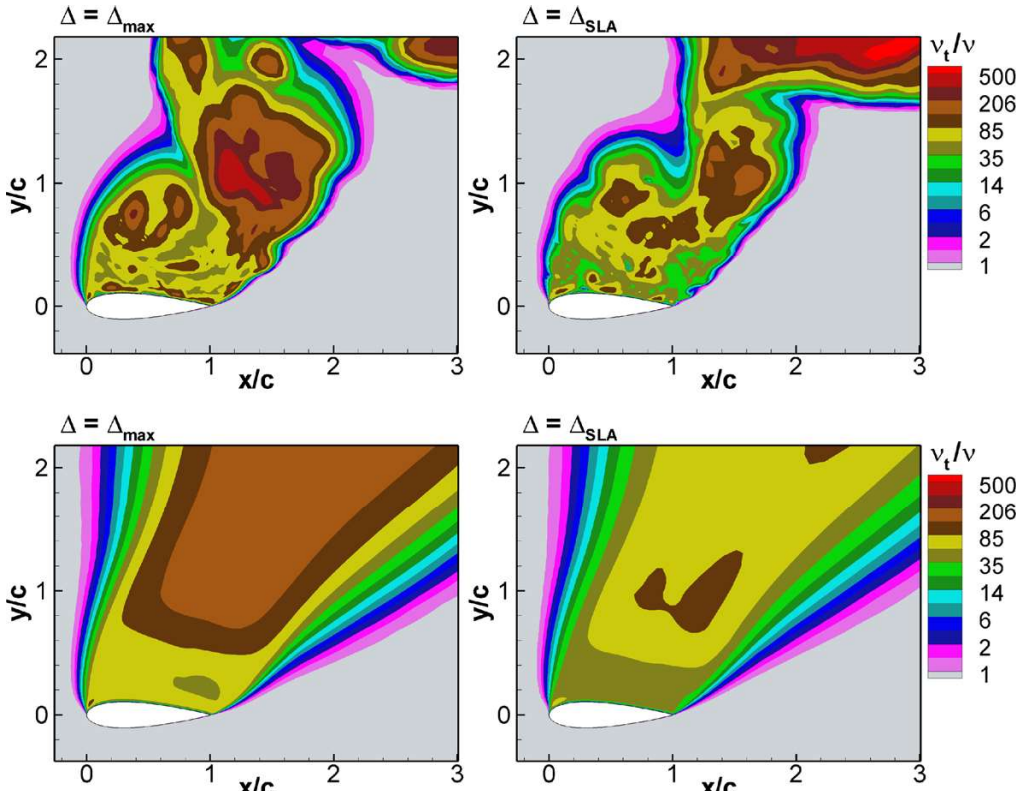

Figure 2.25: Comparison of instantaneous (upper) and time-averaged (lower) eddy viscosity contours between Δ_{max} and Δ_{SLA} [18]

A validation exercise of the NACA0021 deep stall with the SU2 open-source suite was done by Molina [43]. A comparative study was made by investigating the effect of span

lengths, convective schemes, and sub-grid scale (SGS) models. It was noted that the use of low-dissipation schemes resolved the fine structures in the wake in comparison with the more dissipative Roe scheme. Furthermore, the use of the vorticity-based SGS model (Δ_ω) [44] proved to predict lower values of eddy viscosity in the initial regions of the shear layer leading to an accelerated roll-up of leading and trailing edge vortices and finer resolution of the turbulent scales in those regions. Finally, the larger span of $2c$ proved to provide a relatively distinct value of the shedding-peak and its harmonic in the PSD plot of the lift coefficient and a more accurate surface pressure distribution concerning the experiment.

Park [45] used the solver PyFR to execute wall-resolved implicit LES simulations of the flow over a NACA0021 airfoil in deep stall. Span sizes of $7c, 4c, 2c$, and $1c$ were considered. The same span size effects explained in the earlier literature were found to hold. Naturally, the predicted mean integral coefficients and the PSD spectra were of better accuracy for the $7c$ case than what was obtained by DES or DDES. By referring to the non-dimensional pressure contours, it was reasoned that with the increase in span, the primary vortices on the suction side moved further away from the airfoil; additionally, the pressure drop in the wake was also found to have reduced, thus leading to weakened vortices associated with larger span lengths.

2.8 Turbulence Modeling

Flows of practical significance are turbulent and are generally characterized by high Reynolds numbers. Analytical solutions of the Navier Stokes equations in such regimes are yet to be obtained. It is common practice to then obtain approximate solutions by reducing the governing equations to a set of algebraic equations with the help of numerical techniques such as Finite Difference Method (FDM), Finite Element Method (FEM), and Finite Volume Method (FVM). The available turbulence modeling approaches in the sequence of decreasing degree of resolved turbulence and computational cost are Direct Numerical Simulation (DNS), Large Eddy Simulation (LES), Hybrid RANS/LES, and Reynolds-Averaged Navier Stokes (RANS); of these, the approaches that are of significance to the current study and associated turbulence models are explained in the upcoming sub-sections.

2.8.1 RANS Turbulence Models

Following the division of the constituent flow variables into mean and fluctuating components (Reynolds decomposition), time-averaging the continuity and momentum equations yields a set of equations governing the mean values of the flow variables, called the Reynolds-Averaged Navier Stokes (RANS) equations. The resulting Reynolds-averaged continuity and momentum equations are given in equation 2.9 and equation 2.10.

$$\frac{\partial \rho}{\partial t} + \frac{\partial}{\partial x_j}\left(\rho U_j\right) \tag{2.9}$$

$$\frac{\partial \left(\rho U_i\right)}{\partial t} + \frac{\partial}{\partial x_j}\left(\rho U_i U_j\right) = -\frac{\partial P}{\partial x_i} + \frac{\partial}{\partial x_j}\left[\mu\left(\frac{\partial U_i}{\partial x_j} + \frac{\partial U_j}{\partial x_i}\right) - \rho\overline{u_i' u_j'}\right] \tag{2.10}$$

In the above equations, ρ is the density, U_i refers to the mean velocity, u_i' is the fluctuating component of the velocity, P is the mean pressure, and μ is the dynamic viscosity. The term $\rho\overline{u_i' u_j'}$ corresponds to an additional stress term called Reynolds stresses that is a result of the Reynolds-averaging process. This term consists of the fluctuating components, which would further have to be governed by modeling equations to ensure the closure of the system of equations. Eddy viscosity models are the most widely used RANS turbulence models. They are based on the Boussinesq hypothesis, which expresses the Reynolds stresses in terms of the mean deformation rates as given by equation 2.11; where, μ_t is the eddy viscosity, which

is the single unknown that is calculated with the help of transport equations of other turbulence parameters such as the turbulent kinetic energy k, turbulent kinetic energy dissipation rate ϵ, turbulence frequency ω among others.

$$-\rho\overline{u_i'u_j'} = \mu_t\left(\frac{\partial U_i}{\partial x_j} + \frac{\partial U_j}{\partial x_i} - \frac{1}{3}\frac{\partial U_k}{\partial x_k}\delta_{ij}\right) - \frac{2}{3}\rho k\delta_{ij} \tag{2.11}$$

Among the various eddy viscosity models widely used, the Spalart-Allmaras (SA) [46] turbulence model is of importance for the current study and is explained concisely in the following text.

Spalart-Allmaras Turbulence Model

The Spalart-Allmaras (SA) turbulence model is a one equation eddy viscosity model. where a modified kinematic eddy viscosity parameter $\tilde{\nu}$ is modeled. The kinematic eddy viscosity ν_t is obtained as follows:

$$\nu_t = \tilde{\nu}f_{v1} \quad f_{v1} = \frac{\chi^3}{\chi^3 + c_{v1}^3} \quad \chi = \frac{\tilde{\nu}}{\nu} \tag{2.12}$$

The function f_{v1} is referred to as the wall damping function. The transport equation for $\tilde{\nu}$ is as given euqation 2.13.

$$\frac{\partial\tilde{\nu}}{\partial t} + \nabla\cdot(\tilde{U}\tilde{\nu}) = \underbrace{c_{b1}S\tilde{\nu}}_{\text{Production Term}} + \underbrace{\frac{1}{\sigma}\left[\nabla\cdot(\nu+\tilde{\nu})\nabla\tilde{\nu} + c_{b2}(\nabla\tilde{\nu})^2\right]}_{\text{Diffusion Term}} - \underbrace{c_{w1}f_w\left(\frac{\tilde{\nu}}{d}\right)^2}_{\text{Destruction Term}} \tag{2.13}$$

In the above equation, S is the strain rate tensor, d is the distance to the nearest wall and f_w is another wall damping function; σ, c_{b1}, c_{b_2} and c_{w1} are model constants. The reader is referred to the article by Spalart[46] for further information about the constitutive functions and the calibration constants. The SA turbulence model was developed for modeling the effect of turbulence on the mean flow in boundary layers with an adverse pressure gradient, thus justifying its wide use in turbomachinery and aerodynamics applications involving attached or mildly separated flows. The model is ill-suited for application in flows involving massive separation, decaying turbulence, and free shear flows.

2.8.2 Large Eddy Simulations

The RANS approach models the aggregate effect of the large and small turbulence scales on the mean flow. However, when a more detailed insight into the fundamental flow physics of the problem is needed, it is customary to resort to higher-fidelity approaches such as Large Eddy Simulation (LES). It is accepted that the large and usually anisotropic scales of the flow govern the physics of the flow and contain a major share of the flow's turbulent kinetic energy. On the contrary, the smaller and largely isotropic Kolmogorov microscale eddies are solely responsible for viscous dissipation, and they only contain a small fraction of the total turbulent kinetic energy. The aim of LES is then to resolve the energy-containing eddies and model the effect of the more uniform eddies on the resolved flow. The scale separation is achieved by filtering the Navier-Stokes equations. The resulting filtered LES continuity and momentum equations for compressible flows are given by equation 2.14 and equation 2.15.

$$\frac{\partial\rho}{\partial t} + \frac{\partial}{\partial x_j}(\rho\tilde{u}_j) = 0 \tag{2.14}$$

$$\frac{\partial(\rho\tilde{u}_i)}{\partial t} + \frac{\partial}{\partial x_j}(\rho\tilde{u}_i\tilde{u}_j) = -\frac{\partial\tilde{p}}{\partial x_i} + \mu\frac{\partial}{\partial x_j}\left(\frac{\partial\tilde{u}_i}{\partial x_i}\right) - \left(\frac{\partial}{\partial x_j}(\rho\widetilde{u_i u_j}) - \frac{\partial}{\partial x_j}(\rho\tilde{u}_i\tilde{u}_j)\right) \tag{2.15}$$

The filtering operation yields an additional stress term (third term on the right hand side) called the sub-grid-scale stresses $\left(\tau_{sgs_{i,j}} = \rho\widetilde{u_i u_j} - \rho\tilde{u}_i\tilde{u}_j\right)$. Unlike the Reynolds stresses, the SGS stresses include contributions from the SGS eddies, the resolved eddies, and the interactions between the resolved and SGS eddies. However, like the Reynolds stresses, the SGS stresses are also predicted with the help of eddy viscosity models or models involving a transport equation for a turbulent variable. Nevertheless, this is not looked into further in this study.

For high Reynolds number wall-bounded flows, LES simulations demand very fine grids by virtue of resolution required to capture the physics in the boundary layer, rendering a computational expense that is far higher than RANS and nearly an order of magnitude lower than that required by DNS [14], the need for near isotropic grids further exacerbates the computational demand. Following a feasibility study of LES on an airliner wing [14], it was estimated that the about 10^{11} grid points and nearly 5×10^6 time-steps were required to perform a fairly accurate simulation, deeming it to require a daunting computational effort. For detached flows, the grid requirements are less severe.

2.8.3 Hybrid RANS/LES

Hybrid RANS/LES methods utilize the merits of RANS in attached boundary layers and LES in regions of flow separation; they are broadly classified into two categories, namely non-zonal and zonal methods. In the non-zonal approach, there is continuity in the treatment of the RANS/LES interface, and the model equations determine the RANS and LES regions. The onus on defining the RANS and LES regions is on the user in the case of the zonal approach, and there is a discontinuity in the treatment at the RANS/LES interface, where the LES content is explicitly reconstructed to account for large differences in frequency spectrum between RANS and LES regions [47].

Very Large Eddy Simulations (VLES), Limited Numerical Scales (LNS), DES, and DDES are examples for non-zonal hybrid RANS/LES. DDES is of interest in the current study owing to its proven applicability to accurately predict the dynamic flow statistics in flows involving separation [43][48][49]. Hybrid RANS/LES approaches are plagued by grey area effects due to their inability to neither resolve nor model the turbulence in the hybrid RANS/LES interface. Different formulations of SGS lengths scales have proven to be of help in mitigating the grey area issue. DES, DDES, associated SGS length scales, and the accompanying problems are briefly discussed below.

Detached Eddy Simulations

It is well known that for attached flows, very fine grids are needed to resolve relevant turbulence length scales; this is not the case in massively separated flows, as the significant turbulence scales are of the order of the object geometry, thus demanding a much coarser grid. Hence, a non-zonal hybrid RANS/LES approach called Detached-Eddy Simulation (DES) [14] was proposed by Spalart that modeled the boundary layers with RANS and resolved the massive separation region of the flow with LES. The underlying SGS model was based on the one equation SA [46] turbulence model, in which the wall distance variable 'd' in its destruction term was replaced by a modified wall distance term $\tilde{d}$ that is defined in the equation 2.16.

$$\tilde{d} = \min\left(d, C_{DES}\Delta\right) \tag{2.16}$$

In the equation for the modified length scale, C_{DES} is a model constant, d is the wall distance from the node, and Δ is the local maximum grid spacing $\Delta = max(\Delta_x, \Delta_z, \Delta_z)$. The value of $C_{DES} = 0.65$ has been calibrated by Shur [15] for the decaying isotropic turbulence case. In the near-wall regions where $d < C_{DES}\Delta$, the flow is modeled by the SA-based RANS and resolved by LES with the SA-based SGS model elsewhere. This method is also referred to as DES97. The maximum dimension definition of the SGS length scale Δ used here will be referred to specifically as Δ_{max} in the following sections.

Delayed Detached Eddy Simulation

In simulation scenarios involving thick boundary layers, shallow separation regions, and while using grids with wall parallel spacing that is lower than the boundary layer thickness, the LES leg of the DES becomes operational and leads to inadequate generation of turbulent content for the region where the flow was intended to be resolved, thus reducing the turbulent stresses leading to reduced skin friction and sometimes premature separation. The occurrence of separation is termed as Grid Induced Separation (GIS), and the more general reduction in turbulent stresses is termed Modelled Stress Depletion (MSD).

Spalart [50] proposed a correction to the DES length scale $\tilde{d}$ as follows:

$$\tilde{d} \equiv d - f_{\mathsf{d}} \max\left(0, d - C_{\mathsf{DES}}\Delta\right) \tag{2.17}$$

Here, f_d refers to a blending function that takes the value of 0 in the RANS regions $(\tilde{d} = d)$ and 1 in the LES region, reducing to the DES97 expression for the length scale given in the equation 2.16. The blending function is given by the hyperbolic tangent function shown in the equation 2.18.

$$f_{\mathsf{d}} \equiv 1 - \tanh\left(\left[8r_{\mathsf{d}}\right]^3\right) \tag{2.18}$$

In the expression of the blending function f_d, the argument r_{d} is a length scale parameter and is a function of the wall distance d, kinematic eddy viscosity ν_t, kinematic molecular viscosity ν, the Kármán constant κ and the velocity gradient $U_{i,j}$. It is given by the following relation.

$$r_{\mathsf{d}} \equiv \frac{v_t + v}{\sqrt{U_{i,j}U_{i,j}}\kappa^2 d^2} \tag{2.19}$$

Unlike DES97, the DDES formulation is now dependent on the flow and the solution. The new formulation of the length scale $\tilde{d}$ detects boundary layers and *delays* the resolution of the flow in the boundary layer and is thus termed Delayed Detached-Eddy Simulation(DDES).

2.8.4 Vorticity-based SGS length scale

The formulation of the DDES length scale in the equation 2.17 proved to be relatively successful in shielding the resolution of the boundary layers by LES. Nevertheless, the issue involving the delayed formation of instabilities in the mixing layers, also referred to as the 'grey area issue' persistent with DES97, was not remedied by the DDES formulation. The grey area is referred to the RANS-LES interface where the DES or DDES length scale $\Delta \approx d$.

The delay in the formation of instabilities in free shear layers was attributed to the use of the SGS length scale Δ_{max} by Deck [44], who worked on modifying a version of the SGS length scale that was proposed earlier by Chauvet and Deck [51] for zonal DES (ZDES) as follows:

$$\Delta_\omega = \sqrt{n_x^2\Delta_y\Delta_z + n_y^2\Delta_x\Delta_z + n_z^2\Delta_x\Delta_y} \tag{2.20}$$

In the above expression for the vorticity-based SGS length scale (Δ_ω), n_x, n_y and n_z are the unit vectors associated with the local vorticity $\vec{\omega}$. The expression for Δ_ω was primarily meant to rectify the grey area issue prevalent in flow problems involving separation induced either by geometry or by an adverse pressure gradient. The expression for the SGS length scale $\Delta\omega$ modified by Deck [44] for unstructured grids is given by the expression 2.21. Where $\bar{S}_\omega$ is the average cross-section of the cell normal to the local vorticity $\vec{\omega}$.

$$\Delta_\omega = \sqrt{\bar{S}_\omega} \tag{2.21}$$

2.8.5 Shear Layer Adapted SGS length scale

While using the standard definition of DES or DDES, resolution of the flow in quasi-2D regions of separated shear layers by anisotropic grids causes a delay in the development of KH instabilities and prevents their transition to turbulence. This is due to the definition of the length scale Δ_{max}, which overpredicts the SGS eddy viscosity. The definition of Δ_ω, although an improvement over Δ_{max}, still overpredicts the SGS eddy viscosity when the vorticity is no longer two-dimensionally aligned with the grid [42]. An attempt to resolve the issue was made by proposing a modified version of the Δ_ω, which is defined for hexahedral cells as follows:

$$\tilde{\Delta}_\omega = \frac{1}{\sqrt{3}} \max_{n,m=1,8} |(\mathbf{l}_n - \mathbf{l}_m)| \tag{2.22}$$

In the above definition, $\mathbf{l}_n = \mathbf{n}_\omega \times \mathbf{r}_n$, where $\mathbf{n}_\omega$ refers to the unit vector aligned with the vorticity vector, $\mathbf{r}$ is the cell center vector and $\mathbf{r_n}$ is the cell vertex vector at vertex n $(n = 1, 2, ...8)$. Considering a cell in an anisotropic grid with $\Delta_z > \Delta_y > \Delta_x$, $\Delta_{max} = \Delta_z$, $\Delta_\omega = \sqrt{\Delta_x \Delta_y}$ and $\tilde{\Delta}_\omega = \frac{1}{\sqrt{3}} \left(\Delta x^2 + \Delta y^2\right)^{1/2}$. When the vorticity vector is aligned with the z coordinate, Δ_{max} results in an overpredicted SGS eddy viscosity, Δ_ω which although removes the independence of Δ_z leads to an inaccurate value of SGS eddy viscosity as Δ_x would not be relevant for the resolved turbulence scales; this issue is rectified by using $\tilde{\Delta}_\omega$, which is of the order $O(\max\{\Delta x, \Delta y\})$. It was further observed by Shur [42] that $\tilde{\Delta}_\omega$, although proved to be a significant improvement over Δ_{max}, proved to still delay the development of the KH instability, which meant that the local SGS eddy viscosity had to be reduced further. In a bid to achieve this, a modified length scale called the Shear Layer Adapted (SLA) SGS length scale (Δ_{SLA}) was formulated where the $\tilde{\Delta}_\omega$ was further multiplied by a non-dimensional function $F_{KH}(< VTM >)$, whose argument is a grid independent definition of a certain parameter called the Vortex Tilting Measure (VTM) was introduced. VTM is a kinematic measure that identifies the quasi 2D areas in the initial shear layers where the KH instabilities have to be developed. The expression for VTM is given in equation 2.23.

$$VTM \equiv \frac{\sqrt{6}|(\hat{\mathbf{S}} \cdot \omega) \times \omega|}{\omega^2 \sqrt{3\,\mathrm{tr}\left(\hat{\mathbf{S}}^2\right) - [\mathrm{tr}(\hat{\mathbf{S}})]^2}} \max\left\{1, (v^*/v_t)\right\}, \quad v^* = 0.2v \tag{2.23}$$

$$\Delta_{SLA} = \tilde{\Delta}_\omega F_{KH}(< VTM >) \tag{2.24}$$

In the expression for VTM, $\hat{\mathbf{S}} \cdot \omega$ refers to the inviscid vorticity evolution term, ω is the vorticity, $\hat{\mathbf{S}}$ is the strain rate tensor and tr() refers to the trace of a tensor. VTM is close to zero in quasi 2D flow regions and varies between a range of values near one in regions of developed 3D turbulence; thus, a cell averaged value of VTM $(< VTM >)$ is used. The function F_{KH}, is a piecewise linear function that is defined as follows:

$$F_{KH}(< VTM >) = \max\left\{F_{KH}^{\min}, \min\left\{F_{KH}^{\max}, F_{KH}^{\min} + \frac{F_{KH}^{\max} - F_{KH}^{\min}}{a_2 - a_1}(< VTM > - a_1)\right\}\right\} \tag{2.25}$$

Here $F_{KH}^{\max}$, $\{F_{KH}^{\min}$, a_2 and a_1 are empirical constant that are equal to 1, 0.1, 0.3 and 0.15 respectively. $F_{KH} = F_{KH}^{\min}$ for a value of VTM less than a prescribe threshold, following which it rapidly increases to $F_{KH} = F_{KH}^{\max}$ for high values of VTM.

3 OBJECTIVES

The focus of this thesis is to evaluate the robustness of the DDES-FWH framework in obtaining accurate airfoil self noise predictions. The DDES simulations are carried out using SU2, and the far-field noise data is computed with the FWH integral solver developed by Molina [48]; the solver is based on the time-domain FWH integral solution derived by Farassat [24] for solid integration surfaces.

The FWH solver is first validated by analyzing the noise from the laminar flow past a circular cylinder.

The next step in evaluating the robustness of the DDES-FWH is to investigate the airfoil self-noise mechanism of separation-stall. For this purpose, the low Reynolds number case of the NACA0021 in deep stall is investigated. The objectives pertinent to this exercise are:

- To investigate the role of convective schemes with varying degrees of artificial dissipation on obtaining a physically accurate flow solution suitable for acoustics post-processing.
- To identify the influence of the SGS length scales on the flow physics and resolution.
- Identify the characteristics of the far-field noise predictions for an airfoil in deep stall and verify whether the far-field noise predictions are physically accurate.

The last step in evaluating the robustness of the DDES-FWH framework is to check whether accurate far-field noise predictions for a case of turbulent boundary layer trailing edge (TBL-TE) noise is possible. As this case does not involve flow separation, it is not a natural application of DDES.

4 METHODOLOGY

This chapter consists of key information regarding the hybrid CFD-CAA approach's constituents. The near-field flow solution has to be obtained by a CFD solver. The solver description and numerical methods under consideration for spatial and temporal discretization and used convective schemes are discussed in section 4.1. Section 4.2 includes the simplified solid surface Farassat 1A integral solution, followed by a detailed schematic of its Python implementation by Molina [48]. The section also provides the reader an insight into the input data required to obtain the far-field noise data at the desired observer locations.

4.1 Overview of Numerics

Prior know-how in developing and using the simulation suite at the host organization TNO and the availability of extensive documentation concerning the implemented numerical methods led to SU2 being a natural choice. SU2 is an open-source simulation suite used for multi-physics simulation and design [52]. It consists of solver module SU2_CFD which is capable of solving steady and unsteady flow and heat transfer problems governed by the Euler, Navier-Stokes, RANS, heat and wave equations. Spatial discretization of the governing equations is accomplished by edge based Finite Volume Method (FVM) or Discontinuous Galerkin Finite Element Method (DG-FEM) . Among the several temporal discretization methods, convective schemes and linear solvers available, the methods relevant to solving the unsteady flow problems considered in this study are discussed in this section. These methods are common to all the test cases discussed in the chapter 5. Nevertheless, more specific details are mentioned in the simulation setup of the individual test cases.

4.1.1 Spatial Discretization

The integral form of the governing equations form the basis for the Finite Volume Method (FVM). The flow domain is constituted of various control volumes over which the governing equations are integrated. The Gauss divergence theorem helps converting the volume integrals to the surface integrals following which the surface and volume integrals are evaluated numerically. The FVM discretization results in a set of linear algebraic equation for each control volume which have to be solved. FVM is less restrictive in comparison with FDM as it permits the discretization of the domain by structured, unstructured and arbitrary grids from which the control volumes are constructed. Ease of implementation and nominal memory requirements are other favourable traits of FVM.

Flow problems in SU2 are principally solved on unstructured meshes with an edge-based data structure [52]. The median-dual vertex-based scheme is used to compose the control volumes. The simplified semi-discretized form of the governing equation that is obtained after integration over control volumes and the use of Gauss divergence theorem is given by equation 4.1 [52].

$$\begin{aligned}\int_{\Omega_i} \frac{\partial U}{\partial t}\, \mathrm{d}\Omega + \sum_{j \in \mathcal{N}(i)} \left(\tilde{F}^c_{ij} + \tilde{F}^{vk}_{ij}\right) \Delta S_{ij} - Q\,|\Omega_i| \\ = \int_{\Omega_i} \frac{\partial U}{\partial t}\, \mathrm{d}\Omega + R_i(U) = 0\end{aligned} \tag{4.1}$$

In equation 4.1, U refers to the matrix of the conserved variables (density, momentum and energy in the context of the Navier-Stokes equations), Ω_i is the volume of the dual control volume, Q is the volumetric source term, ΔS_{ij} is the area of the face associated with edge ij, $\tilde{F}^c_{ij}$ and $\tilde{F}^{vk}_{ij}$ are the local convective and viscous fluxes. The residual $R_i(U)$ is the sum of the total flux contributions and volumetric source terms. The particulars of discretization of the convective flux is given in subsection 4.1.3.

4.1.2 Temporal Discretization

Unsteady flow problems in SU2 can treated by both explicit and implicit time integration. The implemented methods are the implicit and explicit Euler along with Runge-Kutta method which has higher order accuracy. Conditional stability of explicit methods requires the use of small time steps, thereby rendering the simulation to be inefficient; in contrast, implicit methods are stable and permit the use of larger CFL numbers resulting in a larger time-step enabling faster convergence. Thus, it is decided to use the implicit Euler method for time integration. Following the spatial discretization process mentioned in equation 4.1, the resulting unsteady problem is given by the following equation:

$$\frac{dU_i}{dt} + R_i(U) = 0 \tag{4.2}$$

The inherently implicit dual-time stepping strategy proposed by Jameson [53] is further chosen as it is more robust and ensures a higher order accuracy in time. In this method, the concept of pseudo-time (τ) is introduced and the unsteady problem at each physical time step is further solved by time-marching in pseudo-time to a steady state to obtain a steady state solution. The steady state problem at the physical time step n is given in equation 4.3; where, $R^*\left(U^n\right)$ is the modified residual. In SU2, the second order implicit method is chosen for time marching in the pseudo time. The time step size in pseudo time is set by specifying the number of iterations. A more detailed explanation of the numerical implementation can be found in the work of Zhou [2].

$$\frac{dU^n}{d\tau} + R^*\left(U^n\right) = 0 \tag{4.3}$$

The simulated time span, physical time steps and inner iterations vary for every test case that has been considered and hence, their details are provided in the simulation setup section for each of the individual cases in Chapter 5. Following the complete spatial and temporal discretization of the governing NS or RANS equations, the system of linear equations is solved by the Generalized Minimal Residual(GMRES) method by default in SU2.

4.1.3 Convective Schemes

Among the various upwind and central difference schemes in SU2, the impetus is currently given to the legacy Roe, JST, and the more contemporary SLAU2 schemes.

The Jameson-Schmidt-Turkel (JST) scheme [54] is essentially a central difference scheme in the absence of shocks. Central difference schemes are generally unstable on coarse grids as the resulting flow solution contains non-physical oscillations. The Roe's scheme [55] is an approximate Riemann solver. It is an upwind convective scheme of first-order accuracy

and can be expressed as a combination of a central difference term and an artificial dissipation term. The convective flux from adjacent nodes is used to reconstruct the convective flux at both the sides of the control volume's face. Although having poor accuracy, the upwind discretization ensures stability irrespective of the grid resolution. Second order upwinding is obtained by reconstructing the states on either side of the interface by the Monotone Upstream-centered Schemes for Conservation Laws (MUSCL) approach. Furthermore, in the presence of high gradients, limiters are used to ensure the monotonicity of the solution.

Kitamura [56] proposed a modification of the more general AUSM+ upwind scheme that was first proposed for applications in flows of low or high Mach numbers. SLAU2 involved splitting the convective flux vector into the mass and pressure fluxes, albeit with reduced dissipation. The derived pressure flux constituted a central difference term and two artificial dissipation terms that varied as per the $O(M)$ and $O(M^2)$, with M the Mach number of the flux at the interface. Upon the use of various spatial convective schemes, it was found that the flow solution for a flow over NACA0018 at 0° angle of attack with a Mach number of 0.01 was 5% more accurate than the solution obtained with the Roe scheme.

Modifications for the SLAU2 and Roe's scheme were proposed by both Winkler and Travin that involved multiplying the artificial dissipation terms in the schematic with a blending function σ. Winkler's modification (σ_{FD}) [57] is defined in equation 4.4; here, f_d is the DDES blending function defined by equation 2.18 that is used to distinguish between RANS $(f_d = 0)$ and LES regions $(f_d = 1)$, thereby maintaining pure upwinding nature in the boundary layers and avoiding pure central differencing in the LES regions, thereby ensuring monotonicity.

$$\sigma = \sigma_{FD} = \max(0.05, 1 - f_d) \tag{4.4}$$

Travin's modification (σ_{NTS}) [58], the definition of which is rather complex and not discussed here, maintains a value of 1 in the boundary layers to maintain pure upwinding and is nearly 0 in the LES regions to enable better flow resolution.

In the purview of acoustics, it is recommended to avoid pure upwinding in the LES regions as it involves numerical dissipation that shortens the resolved energy cascade. Although central differencing schemes obtain the best resolution, they would also require finer grids. Thus, the low dissipation Roe and SLAU2 schemes modified by σ_{FD} or σ_{NTS} should intuitively provide better flow resolution. This is verified in the section 5.2.7.

4.2 The FWH Solver

Now that some details of the CFD solver have been discussed, the crucial second part of the CFD-CAA framework used is the FWH integral solver. The current solver used is a Python implementation of Farassat's 1A variant of the integral solution for the FWH acoustic transport equation. This script was developed and used by Molina for determining the far-field noise spectra and directivity plots for the Tandem Cyinders test case [48] which is a model for the landing gear geometry.

4.2.1 Solid Surface Integral FWH Solution

For convenience, the generalized FWH integral solution derived by Farassat [24] discussed in section 2.2 is repeated here. The acoustic pressure fluctuation at the observer at position $\vec{x}$ and time t is given by:

$$
\begin{aligned}
4\pi p'(\vec{x},t) = & \int_{\Gamma} \left[\frac{\dot{Q}_n}{r\left(1-M_r\right)^2} \right]_{\tau=\tau^*} d\Gamma + \int_{\Gamma} \left[\frac{Q_n c_\infty \left(M_r - M^2\right)}{r^2\left(1-M_r\right)^3} \right]_{\tau=\tau^*} d\Gamma \\
& + \frac{1}{c_\infty} \int_{\Gamma} \left[\frac{\dot{L}_r}{r\left(1-M_r\right)^2} \right]_{\tau=\tau^*} d\Gamma + \int_{\Gamma} \left[\frac{L_r - L_M}{r^2\left(1-M_r\right)^2} \right]_{\tau=\tau^*} d\Gamma \\
& + \frac{1}{c_\infty} \int_{\Gamma} \left[\frac{L_r\left(M_r - M^2\right)}{r^2\left(1-M_r\right)^3} \right]_{\tau=\tau^*} d\Gamma
\end{aligned} \tag{4.5}
$$

$$
Q_n = \left(\left(\rho_0 - \rho\right) V_i + \rho v_i\right) \hat{n}_i \tag{4.6}
$$

$$
L_i = \left[P_{ij} + \rho v_i \left(v_j + V_{0j}\right)\right] \hat{n}_j \tag{4.7}
$$

Equation 4.5 is referred to as the generalized solution as it also is applicable to moving data surfaces. It should be noted that in equation 4.5 the time derivatives in $\dot{Q}_n$ and $\dot{L}_r$ are taken with respect to the emission time τ and not the observer time t. In the above equations, Γ refers to the FWH integration surface, r is the radiation vector between a point on the data surface and the observer in the far-field, pointing in the direction of the observer, c_∞ is the speed of sound in the ambient medium, ρ is the local density and ρ_0 is the free-stream density, V_i is the component of velocity of the FWH surface in the i direction, v_i is the local fluid velocity on the FWH surface, $\hat{n}_i$ is the component of the unit normal vector of the integration surface, $P_{ij} = \left(p - p_0\right)\delta_{ij}$ is the inviscid part of the compressible stress tensor, M_i is the mach number of the component of velocity corresponding to the local FWH surface. Also, $M_r = M_i \hat{r}_i, L_r = L_i \hat{r}_i, L_M = L_i M_i$ and $\dot{L}_r = \dot{L}_i \hat{r}_i$. For a stationary impermeable FWH surface and stationary observer, $V_i = 0$, $v_i = 0$ and $M_i = 0$, thereby reducing equation 4.5 to the following integral solution.

$$
4\pi p'(\vec{x},t) = \frac{1}{c_\infty} \int_{\Gamma} \left[\frac{\dot{L}_r}{r} \right]_{\tau=\tau^*} \Gamma + \int_{\Gamma} \left[\frac{L_r}{r^2} \right]_{\tau=\tau^*} d\Gamma \tag{4.8}
$$

The following subsection sheds light on how this has been implemented by Molina [48] in Python.

4.2.2 FWH Python Script

Upon observing the equation 4.8, the crucial information necessary for obtaining the unsteady acoustic pressure data at the observer is the local values of pressure fluctuation, radiation vectors from all the data points on the FWH surface to the observer locations, surface normal vectors, and the distribution of the data points on the FWH data surface. Upon obtaining this data at every time instance from the CFD simulation, the surface integral is carried out as per the integral solution for every emission time instance; this is achieved in the current Python script with the help of certain input files and user defined functions. The sequence of operations is shown schematically in the figure 4.1.

The green trapezoidal cells refer to the input data, data files, or output observer noise file. The square cells with bold entries are the user-defined functions imperative to the script. The blue cells correspond to the binary file generation branch of the script, and the cells shaded in red are the functions constituting the main branch of the script, used for calculating the far-field acoustic pressure data.

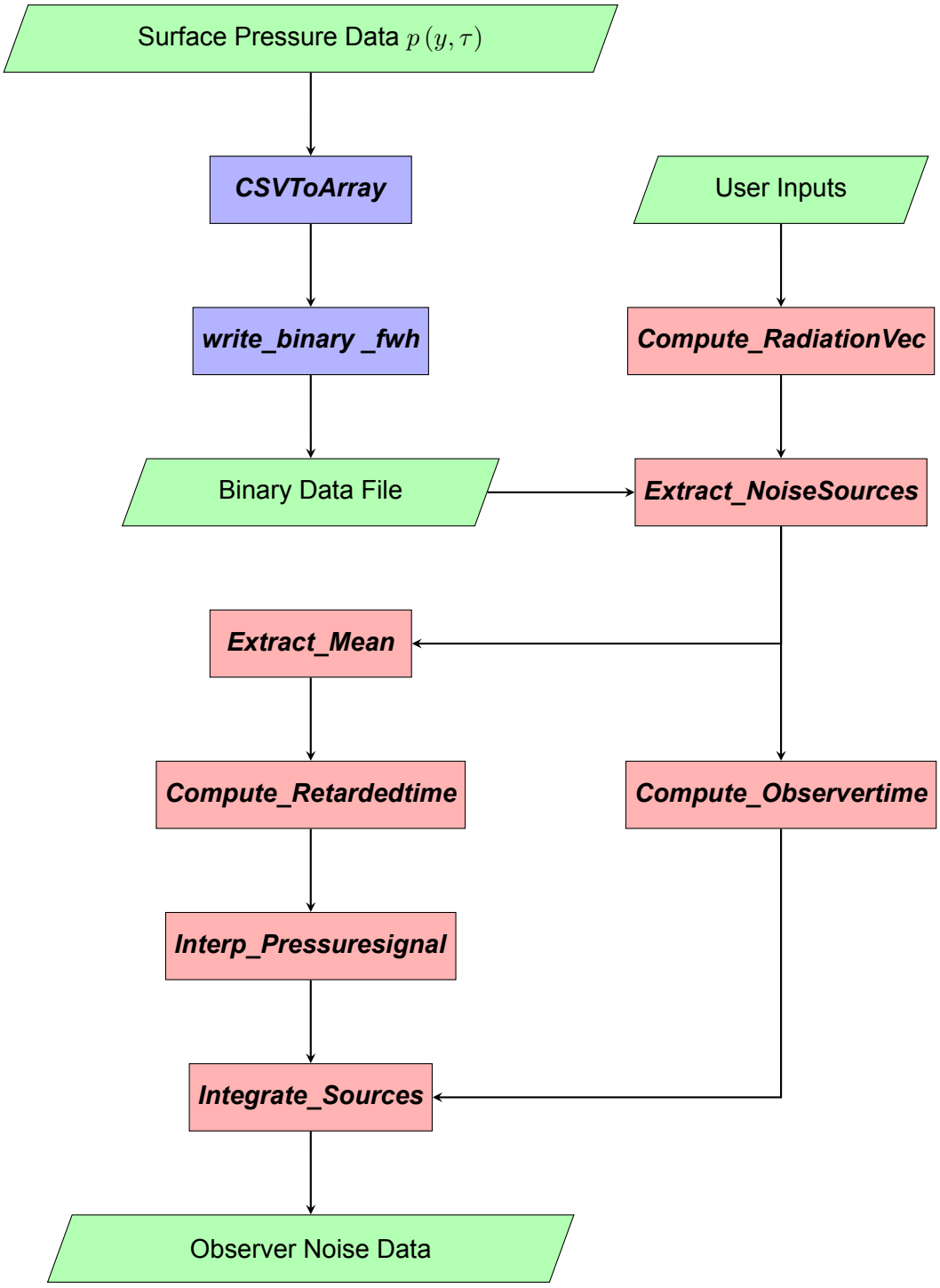

Figure 4.1: Flowchart of the used FWH script

User Inputs

The required user inputs for the script are:

- Binary data file.
- Surface coordinates file: Any one of the surface data files generated by the flow solution can be considered.
- Number of dimensions (optional, as the default selection, is 3).

- Type of analogy (optional, as default selection is 1A).
- Sampling frequency: Number of iterations between the instances at which the surface data files are written.
- Time step considered in the simulation.
- Coordinate normals file.
- Starting iteration number: required to calculate the emission and observer times.

Input Files

The unsteady surface pressure data files generated by SU2 are one of the crucial inputs required by the script. The sampling frequency has to be calculated in terms of the surface pressure data file's writing frequency such that the relevant acoustic sources are captured without compromising the system memory and code performance.

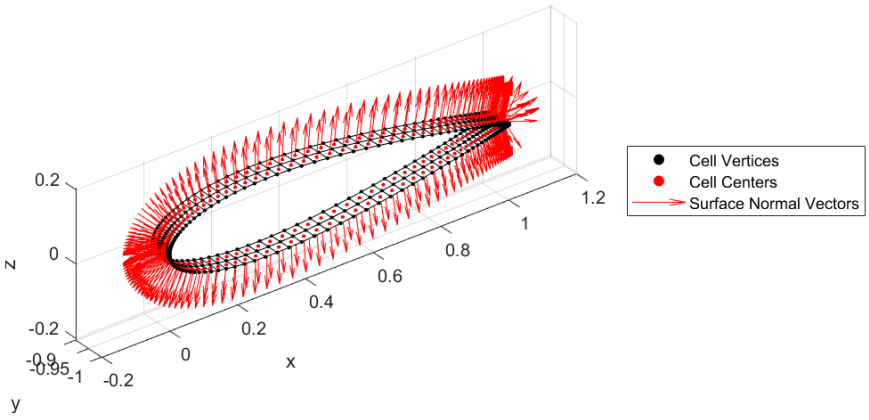

Figure 4.2: FWH Surface and Coordinate Normals

The object surface itself is selected as the FWH integration surface. As it is also the boundary on which the no-slip and adiabatic boundary conditions are imposed, the surface pressure data files for the desired writing frequency can be written directly by SU2 without extensive post-processing. However, as the control volumes are constructed using a median-dual vertex-based scheme in SU2, the data is written at the cell vertices. For the proper functioning of the FWH script, it would be necessary to have cell-centered data, which means that the output surface pressure files for all the recorded iterations have to be post-processed such that the cell vertex data is interpolated to the cell centers. The interpolation is achieved in ParaView by using the *Point Data to Cell Data* filter. The surface pressure data can also be scaled with the help of the script used to interpolate the data from cell vertices to cell centers if necessary. Figure 4.2 shows a segment of the FWH data surface (airfoil surface) that is considered in the surface pressure data file.

Another important input to the script is the *Coordinate Normals* file, which consists of the cell center coordinates, coordinates of the unit surface normals of the FWH data surface, and the area of cells(or panels) considered on the data surface. This information is vital to the script as per equation 4.8. A segment of the surface mesh of the FWH surface consisting of the cells, cell centers, and the surface normals(scaled for ease of visualization) considered is shown in figure 4.2. This file is generated by post-processing in ParaView because of the availability of the connectivity information, which enables ease of calculation of the cell areas even for complicated geometries.

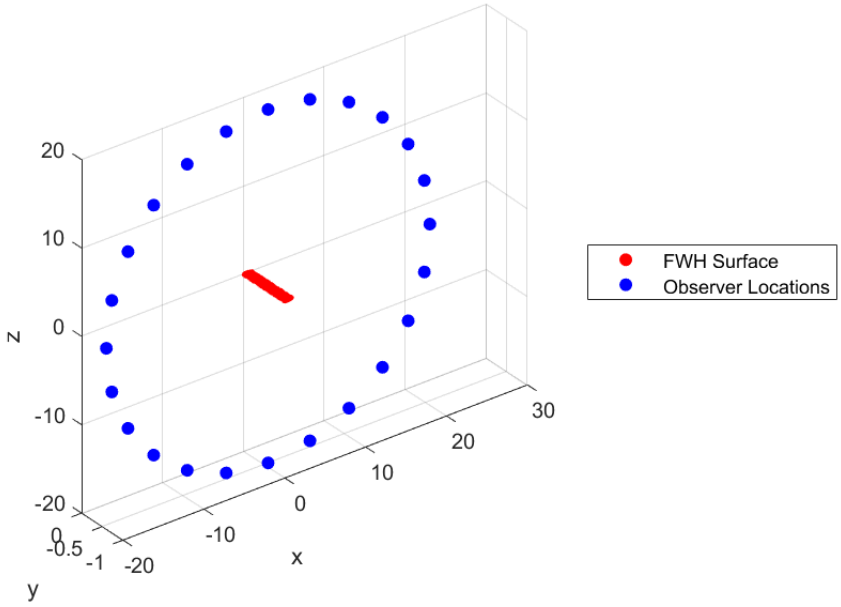

Figure 4.3: Observer location distribution in the far-field

Finally, as per the reference literature or the users' objectives, the coordinates of the desired observer locations are included in a data file; this is another input file needed to calculate the radiation vectors, emission and observer times. For the current thesis, a simple circular distribution of the observers around the FWH data surface, as shown in figure 4.3 will suffice as the objective is to obtain sound power spectra and directivity information. Whereas, for beamforming purposes, the distribution of the observers follows a more complex pattern.

Output Noise Data

The output noise data file consists of an array comprising the observer time instances and the predicted acoustic pressure at each time instance for the various observers included in the input file. This data file can be further post-processed to generate the sound pressure level spectra and the directivity plots.

4.2.3 User-defined functions

The secondary binary data file branch is solely needed for consolidating the unsteady surface pressure data into one binary file for ease of use, which otherwise would require excessive memory and parallelization of the script. The functions of both these branches are briefly discussed below.

CSVToArray

The surface pressure data files are written down by the post-processing module of SU2 (*SU2_SOL*) for specific time iterations as per the desired sampling frequency for acoustics post-processing. The data in these files consist of the cell vertex data, but as data at the cell centers is required, the interpolation is carried out in ParaView's $pvpython$ environment, following which the cell-centered pressure data is saved. However, the temporal resolution required for acoustics means that many such files would be needed for generating results suitable for comparison with literature or experiments. Traditional files such as $.csv$ or $.vtk$ are not practical for these

purposes, and it will be convenient to have a single file that consists of the unsteady pressure data organized as per the point IDs of the cell center coordinates and iteration numbers.

The first step in organizing the data as per the objectives mentioned above is achieved with the *CSVToArray* function. This function reads the pressure data from the surface pressure *.csv* files and organizes them into a two-dimensional array in which the columns correspond to the point IDs and the rows correspond to the iteration numbers.

write_binary_fwh

The function is used to write the number of time steps and the number of points along with the array obtained from the ***CSVToArray*** into a binary file. The binary file will be one of the inputs along with the other user inputs for the main branch of the script.

Compute_RadiationVec

The unsteady surface pressure data, the number of iterations, and the number of points on the FWH surface are allotted to arrays by unpacking the binary file generated earlier with the help of another user-defined function *read_binary_fwh*, which has not been included in the figure 4.1 for conciseness.

Given the default inputs of the analogy type $(1A)$, the number of dimensions, formulation type (solid) and case-specific inputs in the form of the binary file, coordinate normals file, cell center coordinates file, observer locations file, and flow parameters. All the points listed in the cell center coordinates file are looped over to compute the radiation vectors to each observer location so as to obtain an array consisting of the components of the radiation vectors and their magnitude.

Extract_NoiseSources

Given that the 1A FWH analogy is chosen, the unsteady surface pressure data is available, and the radiation vectors are calculated, the next step as per equation 4.8 is to calculate the loading term in the direction of the radiation vector L_r as per equation 4.7 for every panel and time iteration considered; this is achieved by the function *Extract_NoiseSources*.

Furthermore, *Extract_Mean* is invoked to obtain the fluctuating component of L_r, which is the difference between the instantaneous value of L_r and the time-averaged L_r.

Compute_RetardedTime

The last step in determining the integrands in equation 4.8 would be to calculate the time derivative of the loading term L_r; a second-order central differencing scheme achieves this for all the time iterations other than the first and last iterations for which forward or backward differencing is used. Now that all the terms are calculated, the full integrand for the surface integral in equation 4.7 is evaluated as per equation 4.9 and assigned to an array pp_ret.

$$pp\_ret = \frac{1}{4\pi}\left(\frac{\dot{L}_r}{c_\infty r} + \frac{L_r}{r^2}\right) \tag{4.9}$$

Compute_Observertime

As per the function name, the observer time is calculated for every given time iteration, panel, and observer location. The observer time can be calculated as per equation 4.10 if the emission time and radiation vectors are known.

$$t = \tau + \frac{r}{c_\infty} \tag{4.10}$$

Interp_PressureSignal

The pp_ret calculated at the emission time τ by the ***Compute_RetardedTime*** is interpolated cubically to the observer time t with the help of the function ***Interp_PressureSignal***.

Integrate_Sources

The interpolated instantaneous surface pressure source term is finally integrated on the FWH surface to obtain the far-field acoustic pressure fluctuation $p'(\vec{x}, t)$ at the observer location $\vec{x}$ and observer time t. The value is calculated for the desired observer locations and times and is written in the output **Observer Noise Data** file.

The output file consists of the time series of the acoustic pressure fluctuations at the observer locations, whose coordinates are one of the few mandatory user inputs. This data can be used to generate sound pressure level spectra, cross-correlation spectra, and directivity plots.

4.3 Acoustics Post-processing

After obtaining the acoustic pressure time-series at the observer, it is essential to post-process the data to perform time-domain and frequency-domain analysis to obtain insights into the nature of the sound signature by determining the Overall Sound Pressure Level (OASPL) directivity, the SPL spectrum, and the SPL directivity. The measure of the OASPL quantifies sound signals, and it is defined as follows:

$$\text{OASPL} = 20 \log_{10} \left(p_{rms} / p_{ref} \right) \tag{4.11}$$

Where, p_{ref} is the reference pressure whose value is considered to be 20μPa for aeroacoustic applications and 1μPa for hydroacoustics. p_{rms} is the RMS value of the acoustic pressure p'. The resulting OASPL is measured in decibels dB. A common convention is to express the reference pressure along with the decibel units as dB $(\text{re} : p_{ref})$. Decibel A-weighting can be applied to the measure of the SPL to take into account the response of human ear, but this is not considered in the current context. The SPL spectrum is often consulted to ascertain the tonal or broadband nature of the noise signal. The contribution of monopole and multipole sources at various frequencies can be determined by plotting the SPL polar at various observer locations. SPL is determined from the acoustic pressure time series as per the equation 4.12.

$$\text{SPL} = 10 \log_{10} \left(G_{pp} / p_{\text{ref}}^2 \right) \text{ dB re } p_{\text{ref}} \tag{4.12}$$

In the equation for determining SPL, G_{pp} refers to the PSD of the acoustic pressure time series. G_{pp} in this context is determined by calculating the discrete Fourier transform of the time variation of pressure fluctuations or by Welch's method. The latter has been used for all the SPL calculations in this report. When calculated at multiple observer locations distributed in a certain pattern in the far-field, the SPL spectrum also helps plot the SPL directivity polar, which is crucial in evaluating the noise sources relevant to a certain flow phenomenon at a particular frequency.

The information explained in this chapter is essential to understand better the report as a combination of the numerical settings explained earlier are used to obtain the flow solution. By developing a detailed understanding of the implementation of the FWH integral solution in the acoustics solver, the outputs necessary for the correct functioning of the FWH solver are

recognized. Finally, the far-field acoustic pressure fluctuations output of the flow solver is further post-processed to obtain the time and frequency-domain acoustic data mentioned in section 4.3. The following chapter provides a detailed analysis of the unsteady aerodynamic and acoustic results obtained for the cases of the validation, separation-stall noise and TBL-TE noise test cases.

5 RESULTS AND DISCUSSION

This chapter consists of validating the workflow explained in the previous section by analyzing and comparing the flow and acoustic data of the quasi-three-dimensional laminar cylinder test case with the literature. Following this, the physics pertinent to airfoils in deep stall is explained with the help of flow field results and statistical measures of the integral aerodynamic coefficients. The role of the convective schemes and the SGS models on the flow solution is explained. Frequency-domain analysis of far-field noise data is carried out and the resulting trends of the separation-stall noise are qualitatively compared with the literature. Finally, the DDES-FWH workflow is applied to a scenario where the NACA0018 airfoil is at 0° angle of attack. The boundary layer and flow field data are investigated, following which the resulting far-field acoustic information is compared with the experiments. Specific details about the simulation setup are explained in their respective sections for all the test cases.

5.1 Cylinder Test Case

The following subsections consist of the description of the two and three-dimensional laminar cylinder test cases investigated to validate the implementation of the chosen FWH integral solution method developed by Molina [48]. Firstly, the spatial and temporal discretization schemes used for both cases are briefly discussed, following which details of the grid and the boundary conditions are described. The subsection is concluded by validating the flow solution and the far-field acoustic data.

5.1.1 Test case description

Before foraying into the CAA of the cases involving turbulent flow over airfoils that involve multi-scale phenomena, it is essential to validate the CFD-CAA workflow for a simpler two-dimensional test case. In this regard, the two-dimensional laminar cylinder test case has been frequented by many authors for validation, particularly the low mach number laminar flow over a circular cylinder investigated by Inoue[19]; the flow at a Reynolds number of 150 was resolved by DNS. The noise data was computed with the help of Curle's acoustic analogy, and corrections were made to include the Doppler effect for a more physically accurate comparison. Lysenko [20] also referred to this laminar cylinder test case to validate their numerical methodology proposed to resolve the acoustic field directly with the help of LES; an attempt at validating the same is made in the current section. The free-stream flow parameters are tabulated in table 5.1. The following text will refer to this test case as the two-dimensional laminar cylinder test case or cylinder case 1.

Re	Ma	D(m)	T_∞(K)	p_∞(Pa)
150	0.2	1	300	101325

Table 5.1: Flow parameters for the cylinder case 1

5.1.2 Simulation Setup

Numerical Settings

As a simple laminar flow test case is considered, it would be appropriate to choose the FVM-based Navier Stokes solver in SU2, details of which are briefly given in section 4.1.1; the reader is directed to the reference [52] for further details. The second-order implicit dual time-stepping scheme is used for temporal discretization, eliminating the CFL number dependence. The second-order upwind scheme of Roe is used to discretize the convective flux terms with MUSCL reconstruction of the flux. The Venkatakrishnan slope limiter is chosen to ensure monotonicity. Numerical time-steps of both $0.068D/u_\infty$ and $0.034D/u_\infty$ have been investigated and are found to provide an accurate estimate of the flow solution. Nevertheless, only the results from the latter time step are discussed in this chapter.

Mesh and Boundary Conditions

The mesh requirements are less constrained as a low Reynolds number laminar flow is simulated. An O grid mesh consisting of quadrilateral elements that gradually coarsen towards the far-field boundary is used. It is taken care that $y+$ has a value lower than 1 everywhere in the domain. The grid has 398 cells in the azimuthal direction θ and 399 cells in the radial direction r.

As depicted in figure 5.1, the far-field boundary condition is used at the outer boundary of the domain, and a no-slip and adiabatic wall boundary conditions are enforced at the cylinder boundary.

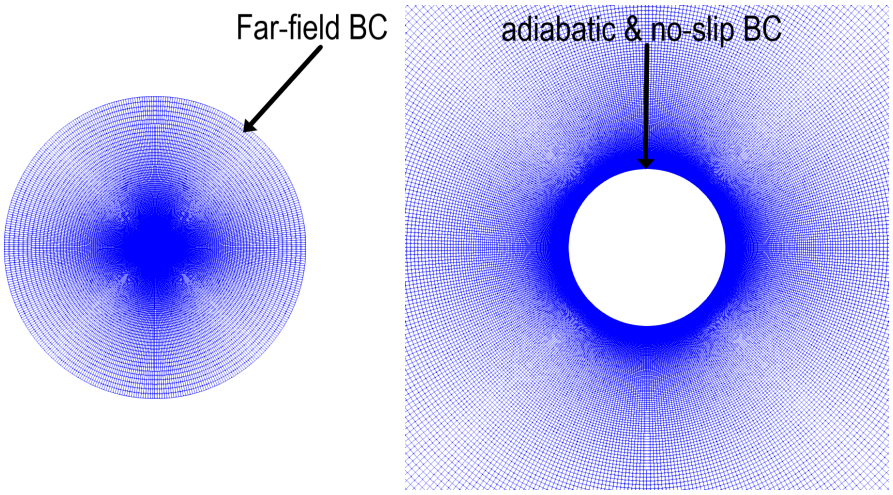

(a) Cylinder far-field boundary (b) Cylinder wall boundary

Figure 5.1: Mesh for the 2D and quasi-3D laminar cylinder test cases

5.1.3 Two-dimensional circular cylinder in laminar flow

Flow solution

The scope of evaluating this test case is to validate the acoustic solver; the first step would be to get an accurate prediction of the flow solution. The comparison is made with the work of Inoue [19] and Lysenko [20] to justify the use of the current grid and solver.

As for any case of flow around bluff bodies, the current flow regime involves alternating flow separation at the cylinder's top and bottom surfaces resulting in the shedding of vortices, thus forming a vortex street pattern in its wake. This can be clearly identified in figure 5.2 which

is a plot of the non-dimensional instantaneous vorticity contours $\omega c/u_\infty$. The regions of large vorticity magnitude correspond to the shed vortices. The direction of the vorticity vectors in the alternating vortices is opposite to each other.

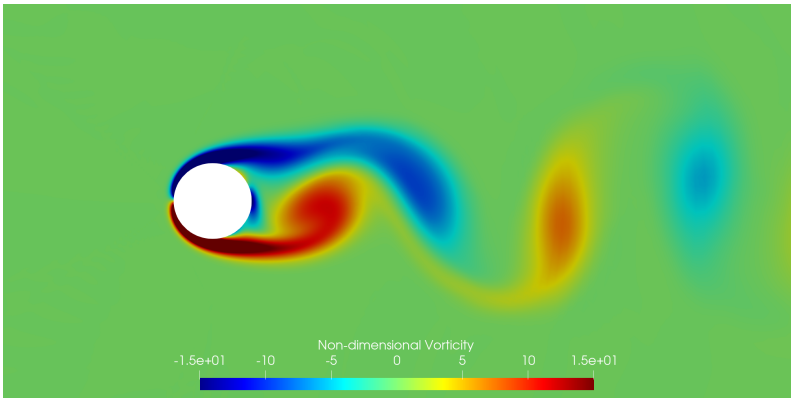

Figure 5.2: Instantaneous non-dimensional vorticity contour.

The alternating shedding of vortices is manifested in the integral lift and drag coefficients due to the change in surface pressure distribution. The nature of the solid FWH integral solution in equation 4.8 indicates that it is crucial to ensure that the dynamics of flow are accurately captured, thereby justifying the definitive comparison of the acoustic data; following this reasoning, the flow field parameters are compared with the LES study carried out for the cylinder case 1 by Lysenko [20] and the DNS study by Inoue [19] to ensure that they are accurately predicted.

The comparison of the integral coefficients between the current simulation in SU2 with the reference literature is made in table 5.2. It is observed that the time-averaged drag coefficient $(\overline{C_d})$, amplitude of lift $(C_l{}')$ and drag coefficients $(C_d{}')$ and the primary Strouhal number of the integral lift (St_1) are in good agreement with experiments, the DNS [19] and LES [20] studies, with their relative errors being well under 5%. The comparison made here ensures that the dynamic surface pressure distribution is captured in the simulation, and it would be appropriate to use the dynamic surface pressure data to obtain the far-field noise.

	$\overline{C_d}$	$C_l{}'$	$C_d{}'$	St_1
Inoue DNS[19]	1.32	0.520	0.026	0.183
Lysenko LES[20]	1.33	0.478	0.023	0.18
SU2 Navier Stokes	1.33	0.510	0.025	0.179

Table 5.2: Comparison of integral coefficient statistics with literature for the Cylinder Case 1

Additional comparisons of the time-averaged flow solution are made in figure 5.3. The time-averaged pressure coefficient on the upper half of the cylinder shown in figure 5.3b further reinforces the agreement seen in the comparison of integral coefficients in table 5.2. In contrast, the non-dimensional time-averaged streamwise velocity in the far-field $\overline{u}/u_\infty$ is overpredicted in comparison with the literature; this can be attributed to the discretization error caused due to the gradual coarsening of the grid in the radial direction, which is more prominent in the far wake.

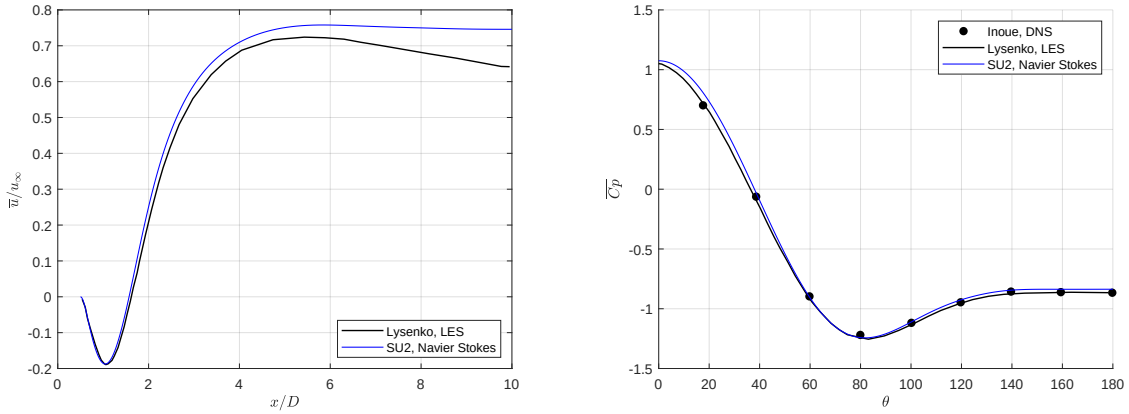

(a) Non-dimensional streamwise velocity $\overline{u}/u_\infty$ (b) Time-averaged surface distribution of Cp

Figure 5.3: Comparison of the time-averaged non-dimensional streamwise velocity in the wake centerline and time-averaged pressure coefficient on the top half of the cylinder surface with literature [19][20].

Acoustic Solution

The flow solution validated earlier warrants the investigation of the far-field noise predictions to verify the Python implementation of Farassat's 1A integral solution by Molina [48]. In this regard, the Root Mean Squared (RMS) value of the acoustic pressure $p' = p - \overline{p}$ at the observers located in the far-field is compared with the same from both Inoue [19] and Lysenko [20]. The observers locations are distributed at the radial location $r/D = 75$. The RMS value of the non-dimensional acoustic pressure fluctuations $p'/\rho_\infty u_\infty^2$ in the far-field is plotted in figure 5.4. The extent of the domain, the spatial and temporal resolution considered also provided the direct acoustic solution with the help of minimal post-processing. It is noticed that the acoustic pressure fluctuation predictions from the FWH script are of the same order of magnitude but are underpredicted consistently at all the observer locations; meanwhile, the direct solution predicts an accurate estimation of the noise in comparison with that obtained by Lysenko[20]. An attempt to obtain the noise predictions from an implementation of a permeable surface was investigated, but the resulting predictions were of poor accuracy.

5.1.4 Need for a three-dimensional test case

An attempt to match the acoustic solution from the FWH script with the same from DNS was attempted in the previous section. The acoustic pressure fluctuations predicted by the current FWH solver involve significant discrepancies when compared with the DNS and LES results. Zhou[2] explained in their study that the time-domain FWH integral solution developed by Di Francescantonio[29] in two dimensions would entail a semi-infinite integral, which would require data from an infinitely long time sample to account for the contributions from all the sources, This would also hold for the current FWH solver as the time-domain solutions proposed by both Di Francescantonio[29] and Farassat[24] effectively reduce to expression 4.8 when a solid-surface integration is performed. Thus, it was essential to find a simple three-dimensional test case that would be appropriate to validate the current workflow. Brentner[21] used the erstwhile WOPWOP code to predict the far-field noise from the flow over a circular cylinder in laminar and turbulent flow regimes. WOPWOP is a helicopter rotor noise prediction tool that utilizes Farassat's 1A time-domain solution for the FWH acoustic transport equation. Thus, it was appropriate to choose the simplest amongst the cases investigated by Brentner to validate the current CFD-CAA workflow. The description of the test case and associated results are given in the following subsections. The simulation setup in terms of numerical settings and mesh is identical to that

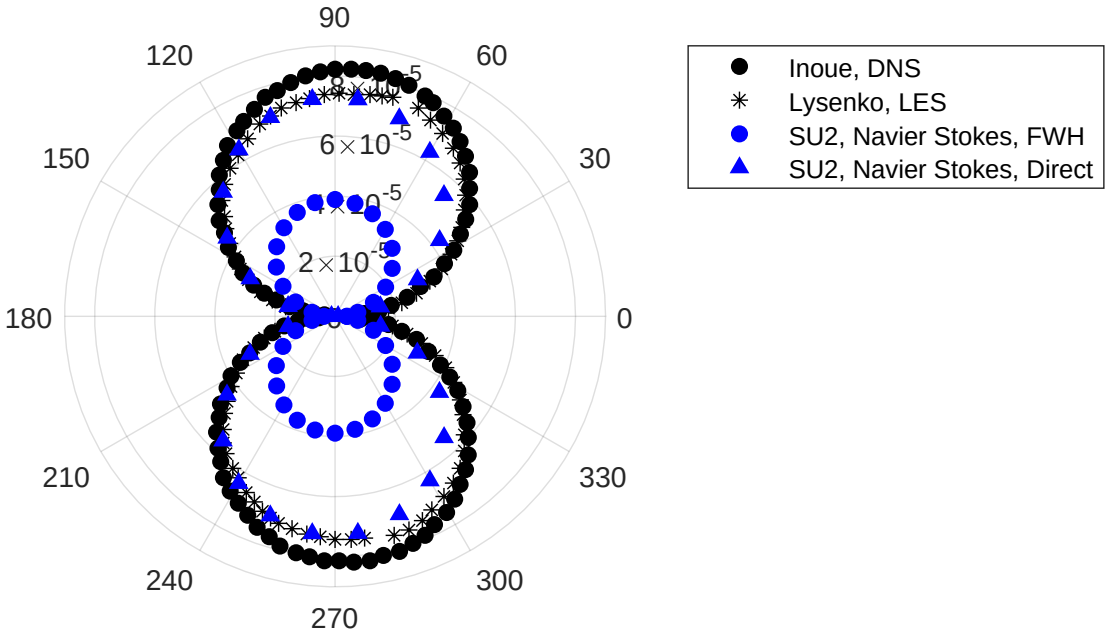

Figure 5.4: Comparison RMS value of non-dimensional acoustic pressure between DNS[19], LES[20], SU2 direct method and SU2 Navier Stokes with the FWH script

used for the cylinder case 1 and is not repeated.

5.1.5 Quasi three-dimensional laminar flow test case

To ascertain the effect of vortex shedding correlation length on far-field noise caused by viscous flow over a cylinder, albeit with nominal computational resources, Brentner [21] assumed a two-dimensional flow solution to be correlated over the entire span of the cylinder. In doing so, cylinders of different span sizes were investigated to match the SPL spectra with the wind tunnel experiment of Revell [59]. It was noticed that a spanwise correlation length (and also span size) of $10D$ was required to obtain the same SPL spectrum that was determined from an experiment involving a cylinder of span $26.3D$ and a spanwise correlation length of $26.3D$ proved to overpredict the magnitude of SPL at the primary shedding frequency by 25dB in comparison to the experiment. In Brentner's study [21], Farassat's 1A integral solution was used to obtain the far-field noise predictions, thereby making it a suitable candidate to validate the current FWH integral solution solver. This test case will also be referred to as cylinder case 2 for convenience.

5.1.6 Test case description

Brentner [21] investigated viscous flow regimes of Reynolds numbers 1000, 10,000 and 90,000. The laminar flow case characterized by a Reynolds number of 1000 was chosen for validation because of the availability of the SPL directivity patterns at the vortex shedding peak and its harmonic, in contrast to the other two cases for which only the far-field SPL spectrum was available. The mesh used for the cylinder case 1 is also used here as the resolution is adequately fine such that $y+ < 1$ throughout the domain. The same numerical settings as before are also used and are not repeated. The relevant freestream parameters used are listed in the below table. The freestream pressure p_∞ is calculated to be 21.7462Pa from the assumption of Sutherland's law as the model for molecular viscosity, which is assumed in SU2. The relevant flow parameters are listed in table 5.3.

Re	Ma	D(m)	u_∞(m/s)
1000	0.2	1	68

Table 5.3: Flow parameters for the cylinder case 2

Flow solution

As this flow regime also involves vortex shedding, the flow solution can be validated by comparing the statistical parameters of the integral lift and drag coefficients. The lift and drag time-series predicted for the two-dimensional viscous flow simulation by Brentner [21] and the same obtained by using the Navier Stokes solver in SU2 are compared in figure 5.5. The lift and drag signals are plotted with respect to the non-dimensional measure of time (t^*) given by $t^* = t/\frac{c}{u_\infty}$; which refers to the flow passes and is commonly expressed in non-dimensional time units called Convective Time Units (CTU). It can be seen that the flow solution from SU2 matches well with the literature in terms of the amplitude of the lift and drag signals. The frequency of the drag signal is evidently more than that of the lift. The alternating sign in the lift signal is due to the vortices shed from the upper and lower surfaces of the cylinder, which exhibit recirculation regions with alternating directions of the vorticity; whereas, the drag force is always in the direction of the freestream velocity. The phase difference is a virtue of the initial transient in the signal that has been neglected.

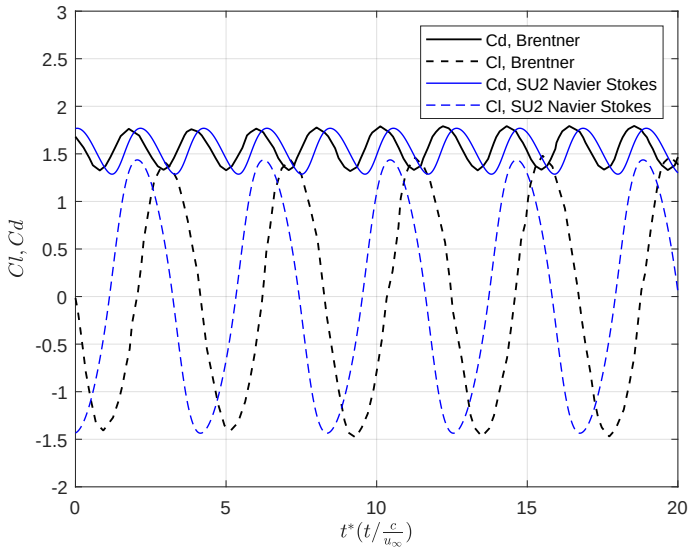

Figure 5.5: Comparison of Cl and Cd time histories for the flow past a 2-D circular cylinder with that of Brentner [21]

The comparison made in the above figure is suggestive of the fact that the dynamics of the flow are captured accurately. This is further reinforced by comparing the predicted frequency of the lift signal's non-dimensional primary shedding frequency St_1 in terms of the diameter-based Strouhal number $(St = fD/u_\infty)$ and the time averaged drag signal with that from the literature, as per table 5.4. Both the parameters are predicted with less than 2% relative error.

	St_1	$\overline{C_d}$
Brentner [21]	0.238	1.562
SU2 Navier Stokes	0.237	1.541

Table 5.4: Comparison of the predicted shedding peak and time-averaged drag coefficient with literature [21].

Validation of acoustic solution

Now that an accurate prediction of the two-dimensional flow solution is obtained, the focus is shifted to replicating the observer noise predictions obtained in the literature, particularly the far-field SPL spectra and the directivity plots. As per the approach adopted by Brentner, the flow is assumed to be coherent in the spanwise direction for the different spanwise lengths considered; this is achieved by repeating the flow solution along various spanwise locations up to the desired spanwise extent. The far-field SPL spectrum at the observer located perpendicular to the freestream and at a radial location of $r/D = 128$ is plotted in figure 5.6a. The flow solution was assumed to be coherent over a spanwise extent of $L_y = 26D$. Dynamic surface pressure distribution for 340 flow passes sampled at every time-step, i.e., $0.034D/u_\infty$, which is one of the inputs to the FWH solver. The resulting acoustic pressure time series is used to obtain the SPL directivity and SPL spectrum plots as per equation 4.12. Welch's method is used to obtain the plot of the far-field SPL spectrum by dividing the acoustic pressure signal into two segments with a 50% overlap. It is noticed that the magnitude of SPL at the primary shedding peak is accurately predicted along with the frequency of the shedding peak and its harmonic, with the relative error being less than 0.5%. At frequencies other than the tonal frequencies, the SPL magnitude is overpredicted; nevertheless, it is of an acceptable measure. Excellent agreement with the literature is seen in the predictions of the OASPL directivity plotted in figure 5.6b. The OASPL directivity plot corresponds to the cylinder of spanwise extent $L_y = 10D$ and the radial location of the observers at $r/D = 35$.

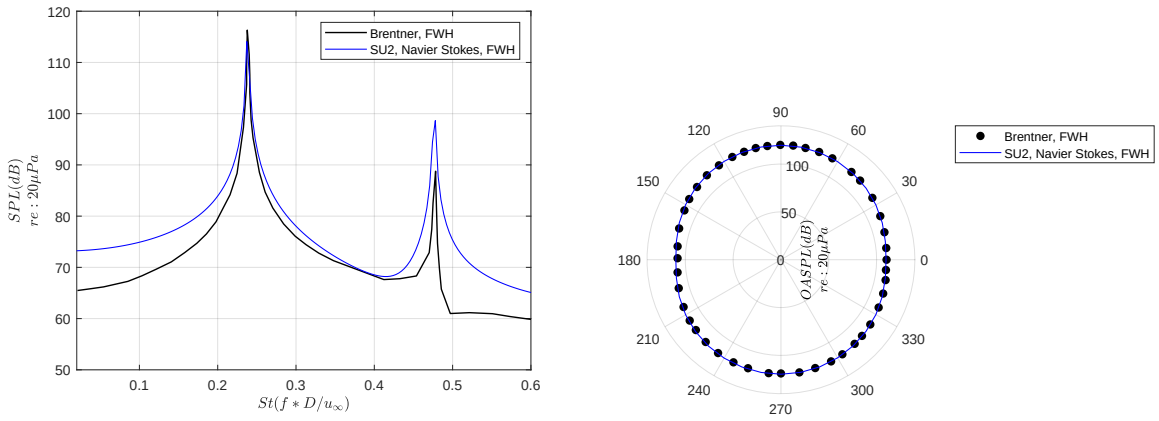

(a) Spanwise extent $L_y = 26D$ and Observers at $r/D = 128$

(b) Spanwise extent $L_y = 10D$ and Observers at $r/D = 35$

Figure 5.6: Comparison of the far-field SPL spectrum and the directivity of the OASPL with literature [21] for different spanwise extents and observer locations

As a low Mach number flow phenomenon is considered here, an assumption of dipole directivity is reasonable; the contour plot of the acoustic pressure fluctuations resolved by the grid is given in figure 5.8, which further confirms this assumption. In the purview of validating

the current FWH script, it is necessary to accurately predict the directivity of the resulting noise at characteristic frequencies. Since the vortex shedding phenomenon generates a sound signal that is tonal in nature, the characteristic frequencies would be the primary vortex shedding peak and its harmonic. The SPL directivity at the characteristic frequencies are plotted in figure 5.7. The flow solution is again sampled at every time step for about 340 flow passes. The SPL magnitude and directivity at the primary shedding frequency St_1 nearly overlap with the experiment's. The acoustically compact nature of the source is captured accurately at the primary frequency St_1 and at the first harmonic of the shedding frequency St_2, where the magnitude of the SPL directivity is accurate throughout the domain except for some discrepancy in the directions perpendicular to the streamwise direction.

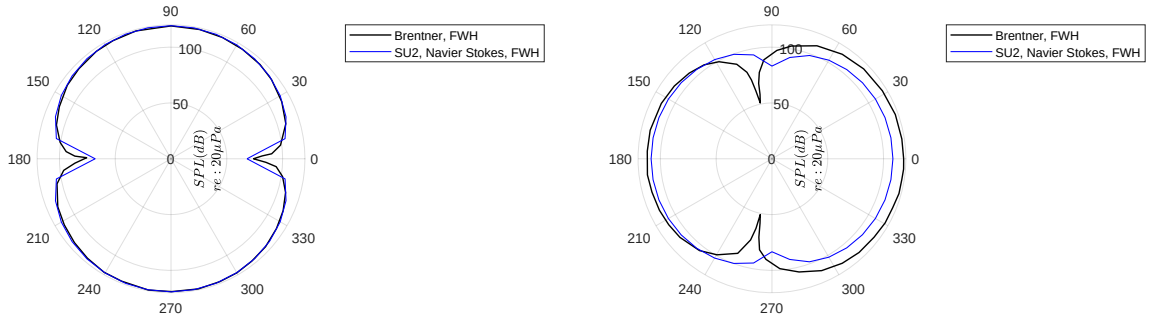

(a) SPL directivity at the primary peak St_1

(b) SPL directivity at the first harmonic St_2

Figure 5.7: Comparing the far-field SPL directivity at the observers located radially at $r/D = 35$ with the literature [21] for a spanwise extent of $10D$.

The objective of investigating the two-dimensional and quasi three-dimensional laminar flow test cases in this section was to evaluate the validity of the Python implementation of Farassat's 1A FWH integral solution made by Molina [48]. The solver failed to provide accurate predictions for the purely two-dimensional case, which has been observed earlier by Zhou [2]. Thus, it was needed to use the solver to obtain the noise predictions from a three-dimensional geometry. The quasi three-dimensional laminar cylinder test case investigated by Brentner [21] is an ideal candidate for the validation study owing to the requirement of modest computational resources and numerical complexity. Accurate far-field noise predictions are possible as per the trends observed in the OASPL directivity and the frequency domain results of the SPL spectrum and the SPL directivity plots. There are nevertheless minor discrepancies observed in the frequency domain data that can be a result of the post-processing strategy used in terms of the type of window, window size, or the time span considered; these errors are, however, not significant because of which, it can be concluded that the FWH script that is being used has been successfully validated.

5.2 NACA0021 in deep stall

The validated FWH solver necessitates its application to determine far-field aerodynamic noise from practical flow regimes involving complex physics. The NACA0021 in deep stall is an example of one such flow regime characterized by low Reynolds and Mach numbers. This test case also finds prominence in validating new turbulence resolving approaches owing to the availability of vast aerodynamic data from the wind tunnel experiments performed by Swalwell [39]. The availability of acoustic data in this regime is limited due to the nozzle flow oscillations that make the far-field noise dependent on the nozzle configuration, thereby resulting in unreliable acoustic data [9]. Brooks [8], in their experimental work, limited the angle of attack to 25° due to large uncorrectable flow deflections. The difficulty in getting reliable data can be overcome by performing DDES simulations, which have been formulated specifically for flows involving massive

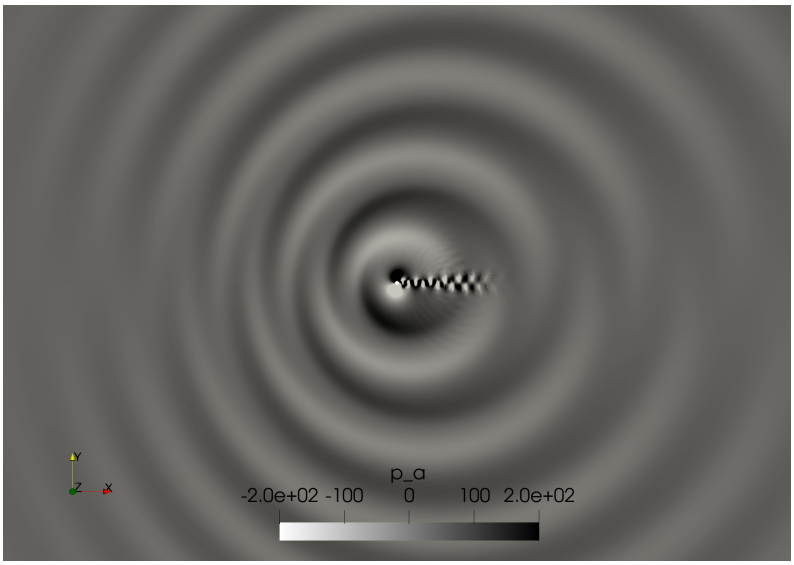

Figure 5.8: Acoustic field (p') obtained using the direct method

separation. Nevertheless, appropriate numerical methods and turbulence models have to be investigated to identify their role in obtaining a physically accurate solution so that an accurate prediction of the far-field noise can be obtained from the FWH solver.

5.2.1 Simulation Setup

This subsection briefly lists the numerical methods used to obtain the flow solution. The merits of these methods are explained in section 4.1. The methods that are not dealt with in both these sections are default to SU2 or any other CFD program and can be found in the configuration files given in the appendix B.

Spatial Discretization

The FVM based compressible RANS solver in SU2 is chosen for the simulation. The effect of purely upwind and hybrid central/upwind convective schemes is investigated by using the Roe [55] and SLAU2 [56] schemes. MUSCL reconstruction is further applied with the convective schemes to obtain second-order accuracy and the Vekatakshrishnan slope limiter to ensure monotonicity. The blending function proposed by Travin [58] is used with SLAU2 to have a better resolution of the wake region by central differencing. The convective term in the SA turbulence model is discretized spatially by a simple first order upwind scheme. Gradients are evaluated by the Green-Gauss method.

Temporal Discretization

An implicit second-order dual-time-stepping scheme [53] carries out temporal discretization; its use leads to the utilization of two different CFL numbers defined for the physical and pseudo time domains called unsteady and steady CFL numbers. The unsteady CFL number is disregarded due to the implicit nature of temporal discretization, whereas a strong dependence on the steady CFL number is observed. The steady CFL number influences the time-step chosen by the solver in pseudo-time. Furthermore, pseudo-time temporal resolution can also be controlled by specifying the number of inner iterations. For this case, a steady-state CFL number of 5 leads to favorable convergence in pseudo time. The influence of inner iterations is explained in brief in subsection 5.2.4.

Turbulence Modeling

It has been concluded in the literature [17] that the underlying RANS turbulence model does not heavily influence the flow solution in the deep stall test case. Hence, choosing a computationally inexpensive turbulence model would be beneficial; the Spalart-Allmaras based DDES would then be a natural choice for modeling the turbulence in RANS regions of DDES. The dynamic SGS model used in the regions of LES is also based on the SA turbulence model as explained for DES in subsection 2.8.3. The availability of the grid and flow solution-based definitions of the DDES length scale warrants a detailed investigation to elucidate the role of the DDES length scale on the unsteady aerodynamic solution and acoustic data; this is pursued in subsection 5.2.8.

5.2.2 Test case description

The flow parameters relevant to the test case are listed in table 5.5. The comparison of the dynamic flow field data is made with the experimental data obtained by Swalwell [13] for the same flow configuration but for a smaller airfoil geometry with a chord (c) of 0.125 m and span (L_y) of $7.2c$. As the deep stall flow configuration involves massive separation and shedding of coherent vortices, it is expected that the using smaller span sizes will result in an over prediction of the integral lift and drag coefficients as the vortices shed would exhibit high values of coherence along the span-wise direction as explained by Garbaruk [17]. The span size effects are also investigated here, and analysis of the resulting data is done in subsection 5.2.6. However, investigating a geometry of such a large span will prove to be computationally expensive, which is why a span of $1c$ is preferred for the test cases listed in the table 5.6.

Parameter	Value
Chord-based Reynolds number (Re_c)	2.7×10^5
Chord length (c)	1m
Angle of attack (α)	60°
Freestream Mach number M_∞	0.1
ty l_u	0.6%

Table 5.5: Flow parameters for the NACA0021 deep stall test case.

One of the objectives of studying this test case is to evaluate the influence of convective schemes of varying degrees of artificial dissipation and different SGS length scale definitions on the unsteady flow solution and far-field noise, the test cases investigated for this purpose are listed in the table 5.6.

	Case 1	Case 2	Case 3	Case 4	Case 5
Convective Scheme	Roe	SLAU2	JST	SLAU2	SLAU2
Blending Function (σ)	1	σ_{NTS}	σ_{NTS}	σ_{NTS}	σ_{NTS}
SGS Definition	Δ_{max}	Δ_{max}	Δ_ω	Δ_{SLA}	Δ_{SLA}
Span Size $L_y(m)$	1	1	1	1	5

Table 5.6: Deep stall test cases investigated.

Mesh and Boundary Conditions

A circular domain of diameter $14c$ is used with an O grid mesh having elements that gradually coarsen towards the far-field boundary. For the $1c$ span configuration, the mesh is composed of about 4.06×10^5 hexahedral elements with $N_r = 81$, $N_\theta = 167$ and $N_z = 30$. The elements

are adequately clustered at the leading and trailing edges. The condition $y+ \approx 1$ is satisfied in the wall-normal direction. Same resolution in the radial, azimuthal and spanwise directions is maintained in the grid for the $5c$ span configuration. The gradual coarsening of the elements in the radial direction ensures that the far-field boundary reflects no spurious waves, because of which it would not be required to use the non-reflecting boundary condition. Although the gradual coarsening limits the resolution of the flow in the far wake, it would not be significant to the unsteady loading of the airfoil, which is only influenced by the flow structures in the near field. A grid refinement study has not been performed due to the computationally intensive nature of DDES simulations.

The no-slip and adiabatic boundary conditions are applied to the airfoil surface. The outermost surface of the domain is imposed with the far-field boundary condition. Periodic boundary conditions were used on both the spanwise faces.

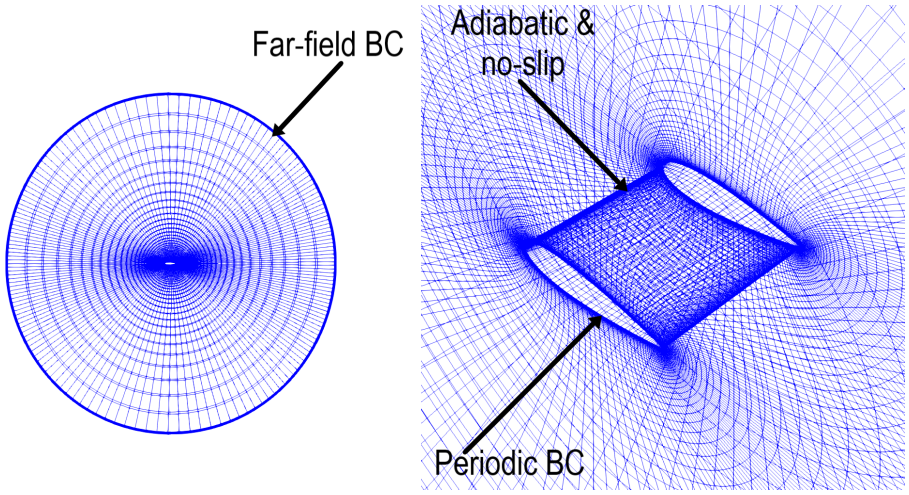

(a) Domain with the far-field boundary.

(b) Airfoil surface and periodic boundaries.

Figure 5.9: The O-grid mesh for NACA0021 in deep stall with $L_y = 1c$.

5.2.3 Simulation Procedure

Starting the DDES simulation from an initial condition involving the freestream values of the state variables is not recommended as it would lead to a long period of the initial transient in which the flow solution is not converged. In a bid to enable a faster convergence rate, the following procedure is followed:

1. A converged first-order RANS solution is obtained by neglecting the MUSCL reconstruction.
2. The solution obtained in the previous step is used as the initial condition to obtain a converged second-order accurate RANS solution using MUSCL reconstruction.
3. The converged second-order RANS solution is used as the initial solution for the unsteady DDES simulation.

5.2.4 Time sample and temporal resolution considerations

The aperiodic vortex shedding behavior requires long simulation run times [41]. The inaccurate initial transient present in unsteady simulations further factors into this requirement. Moreover,

it was also found in the running average plot of the experimental C_d that only after 4000 convective time units (CTU) did the running average value of the drag coefficient reach the ensemble mean. It has also been noted in the previous simulation exercises [41][18][16] that the initial transient is present for about 100-400 CTUs. Taking into account these considerations rather conservatively, the data sampling for unsteady aerodynamics and acoustics post-processing is begun only at 4800 CTUs and ended at 5200 CTUs. Figure 5.10a is a plot of the variation of the running average integral lift C_l (lift coefficient of the whole airfoil) with the non-dimensional time. It is observed for every case that at least 1400 CTUs are required for the running average value to reach the ensemble mean.

A time-step of $0.03c/u_\infty$ is chosen based on a similar temporal resolution of $0.025c/u_\infty$ considered in the literature [12][43] which has proven to provide accurate predictions of the vortex shedding peak and the harmonic of the integral lift coefficient. In order to ensure that the temporal resolution is adequate, a smaller time-step $0.015c/u_\infty$ has been checked. The figure 5.10b is a plot comparing the PSD of the integral lift coefficient from both the cases of $0.03c/u_\infty$ and $0.015c/u_\infty$ and the experiment [39]. The trends in the distribution of the power in the lift signal match with each other for both the time steps as per the PSD plot in figure 5.10b. However, the over prediction in the magnitude of the PSD is seemingly higher for the larger time step at the shedding peak and higher frequencies. The discrepancy should be acknowledged, but it is not as significant to demand the use of the smaller time step for all the cases due to the doubling of the computational expense. The dynamic behavior is captured accurately for both the time steps as the shedding frequency predictions only exhibit a relative error of 2% with the experiment.

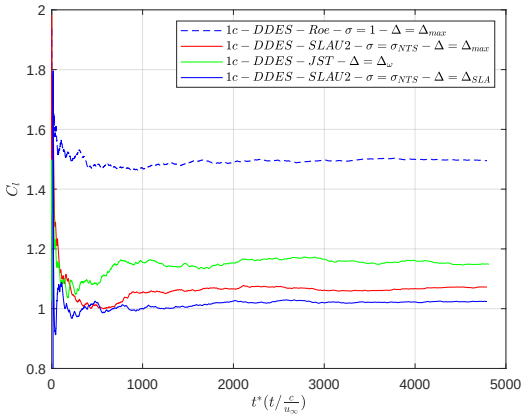

(a) Variation of running average of C_l.

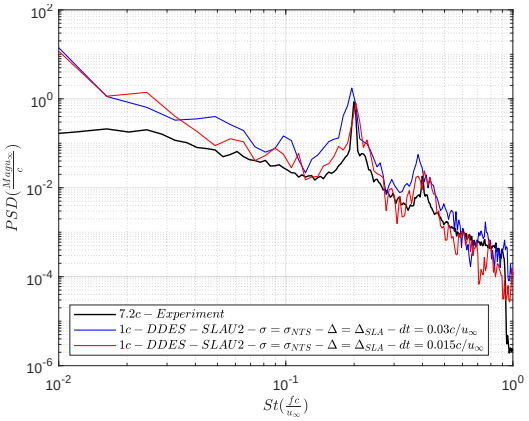

(b) Integral lift's PSD variation with time step.

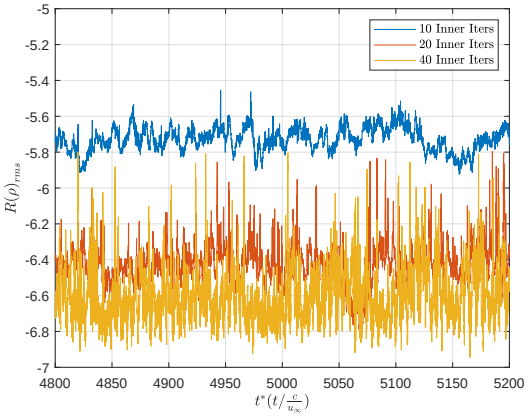

(c) Density residual variation with inner iterations.

Figure 5.10: Plots of running average of integral C_l, PSD of integral C_l, and density residual variation.

The figure 5.10c shows the variation of the density residuals with the number of flow passes for different number of inner iterations. The stochastic nature of the vortex shedding in deep stall results in the variation of the residuals with time. A steady CFL of 5 was used in all three cases to ensure a constant time-step in pseudo time. In the plot, the density residuals plotted correspond to the value attained at the last iteration in pseudo-time. The density residuals predicted at 10 inner iterations are an order of magnitude larger than those at 20 and 40 iterations, for which they are of a comparable order of magnitude; this indicates an asymptotic behavior in the convergence rate in pseudo-time. Hence, it was decided to choose 40 inner iterations for all the deep stall cases because it provides the lowest residual predictions on average.

The numerical methods imperative to obtaining the results discussed in the following sections have been in briefly explained in the previous sections and section 4.1 with more details. The reader is referred to the appendix B.

5.2.5 Flow field results for NACA0021 deep stall case

The results presented here on correspond to the DDES simulations with 40 inner iterations and the time-step of $0.03c/u_\infty$. The solution data is sampled between 4800 and 5200CTUs. This section aims to identify the physical phenomena manifested in the massively separated wake. The flow field of the $1c$ case is investigated. The discussed physical phenomena are found in all the cases in the table 5.6.

Pressure contours

The pressure contours at the mid-span plane of the NACA0021 in deep-stall are plotted in the figure 5.11. It can be seen that the flow remains attached on the pressure side, and there is a region of massive separation on the suction side. The dynamics associated with deep stall can be seen developing on the suction side in figures 5.11a and 5.11b. The shear layer roll-up can be identified at the leading edge owing to the recirculation region present upstream of the leading edge. The figure 5.11b depicts the shed leading edge vortex convected downstream and the shear layer roll-up at the trailing edge. The subsequent shedding of vortices at the leading and trailing edges form a vortex street pattern characteristic of airfoils in deep stall, which can also be considered similar to a bluff body.

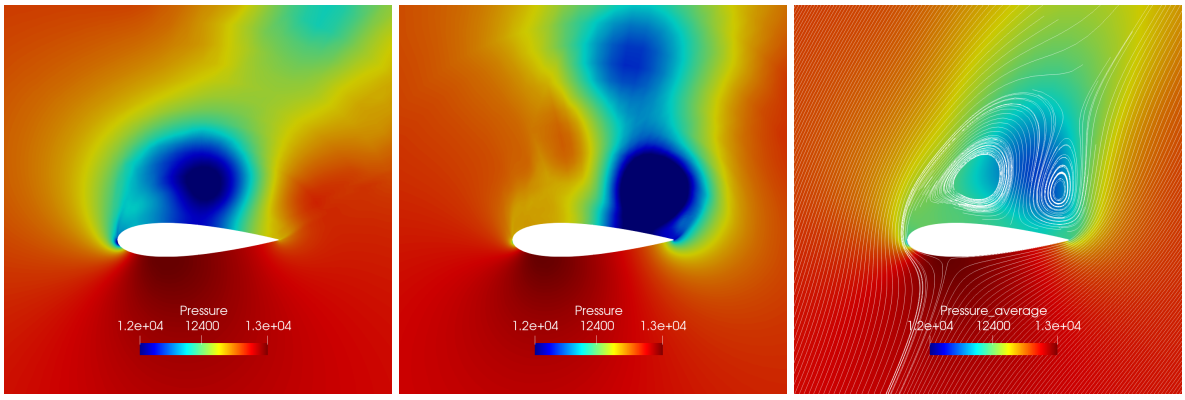

(a) Separation at Leading Edge (b) Separation at Trailing Edge (c) Time-averaged pressure

Figure 5.11: Near wake Pressure contour for the $1c$ span geometry at the mid-span plane

The figure 5.11c contains the plot of the time-averaged pressure, with streamlines on the mid-span plane. The extent of the massively separated near wake region can be identified

in this plot, along with the low-pressure recirculation region on the suction side corresponding to the vortices shed from the leading and trailing edges.

Contours of Non-dimensional Vorticity

The unsteady vortex shedding phenomenon in the massively separated wake is noticed in the contours of non-dimensional spanwise vorticity $\omega_y c/u_\infty$ plotted in figure 5.12 at different leading and trailing edge vortex shedding instances. The alternating vortices shed at the leading and trailing edges form a vortex street pattern in the far wake. The recirculation regions corresponding to the leading and trailing edges exhibit high spanwise vorticity, albeit with the opposite direction due to the roll up of the vortices at the leading and trailing edges. The shear layer roll-up at the trailing edge is accompanied by the detachment and stretching of the leading edge vortex in these plots; the same can be noticed at the leading edge. The coarseness of the mesh in the downstream direction hampers the resolution of the shed vortices in the far wake. Although structures finer than the primary vortices are resolved, they can hardly be identified in the plot of non-dimensional vorticity. The Q criterion contours help visualize these intermediary structures as shown in figure A.1 in the appendix.

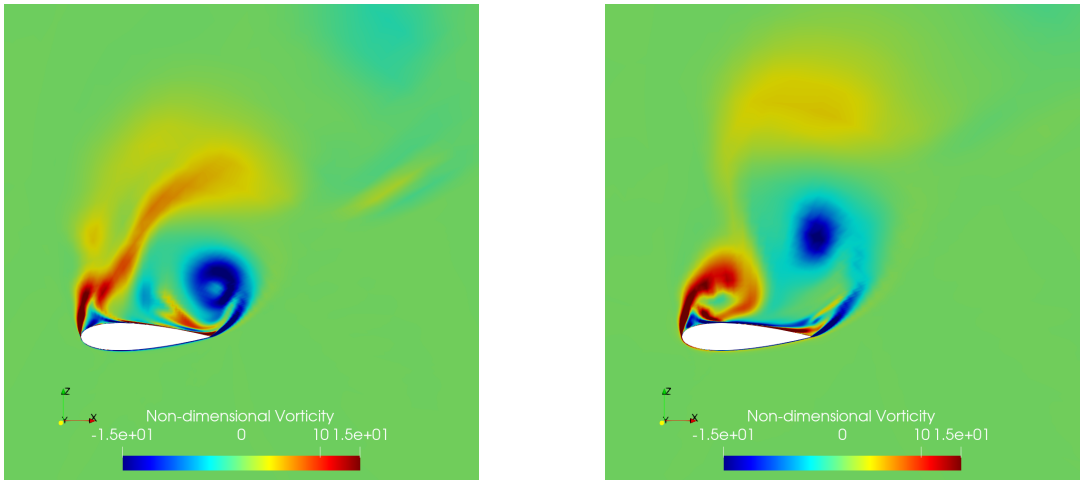

(a) 4871.4 CTU

(b) 4872.6 CTU

(c) 4873.8 CTU

(d) 4875 CTU

Figure 5.12: Vorticity contours at at different instances of vortex shedding at leading and trailing edges at the mid-span section $y/c = -0.5$.

Figure 5.13 depicts the contours of non-dimensional vorticity at spanwise locations

$y/c = -0.25$, $y/c = -0.5$, and $y/c = -0.75$ for the non-dimensional time instance of 4871.4 CTU. The highly coherent nature of vortices along the spanwise direction is evident from the plots due to the occurrence of vortex roll-up at the trailing edge in all the spanwise sections. However, the three-dimensionality is also apparent as the trailing edge vortex is in the initial phase of the roll-up at the spanwise section $y/c = -0.25$,whereas the same vortex is about to detach at the spanwise section $y/c = -0.75$. Furthermore, intermediary structures finer than the primary vortices and with smaller values of coherence along the spanwise direction are also visible. Naturally, the Q criterion plots would enable better visualization of the finer structures; the Q criterion contours at different spanwise locations are included in the appendix in figure A.2. The spanwise coherence in the initial shear layer regions exhibits a dependence on the length of the airfoil span considered [17]. A more appropriate parameter to investigate the spanwise coherence is to plot the two-point spanwise correlations of the components of the flow velocity; the variation of the two-point spanwise correlation for two different span sizes has been investigated by Garbaruk [17] and is explained in the subsection 5.2.6.

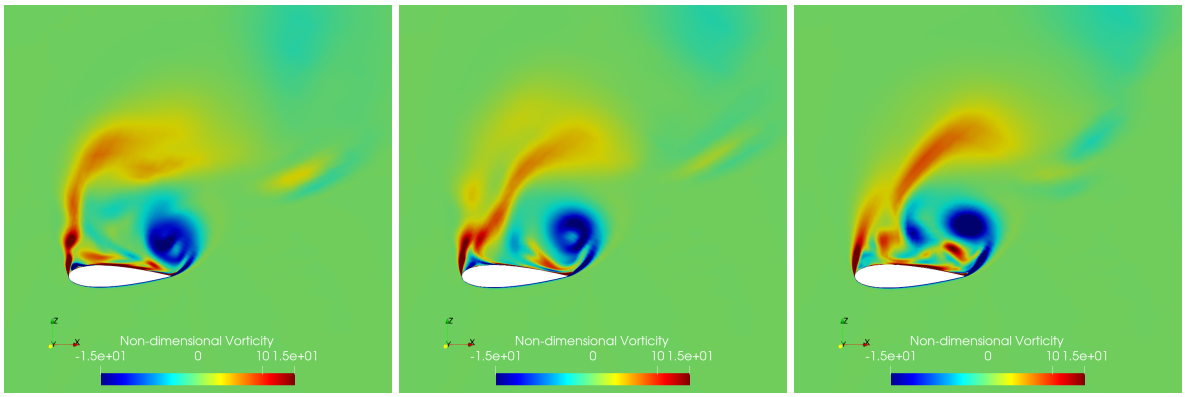

(a) $y = -0.25/c$ (b) $y = -0.5/c$ (c) $y = -0.75/c$

Figure 5.13: Spanwise variation of non-dimensional vorticity $\omega_y c/u_\infty$ at instance of 4871.4 CTU.

The time instances for which the mid-span non-dimensional vorticity contours are plotted in figures 5.12a-5.12d are indicated in the mid-span sectional C_l time series in figure 5.14. The lift varies stochastically as has been observed earlier in the literature [41], but with the primary frequency being that of the vortex shedding.

Iso-surfaces of Q-criterion

A more nuanced view of the scales present in the near wake region of the three-dimensional massively separated flow can be identified by plotting the iso-surfaces of Q-criterion for the two instances of the developing leading edge vortex considered in figure 5.12c and figure 5.12d. In figure 5.15 the primary leading and trailing edge vortices can be identified along with the streamwise rib vortices that are being convected downstream. Finer structures in the initial shear layer region are also found in figure 5.15b. The shear layer roll-up is quasi-two-dimensional initially(figure 5.15a), following which, the KH instabilities enable it to evolve three-dimensionally (figure 5.15b). The nature of the shear layer roll-up is influenced by the local eddy viscosity in the initial shear layer region, which further depends on the SGS length scale used; this is explained in detail in subsection 5.2.8. The eddy viscosity also influences the degree of flow resolution in the wake.

Now that the flow field features have been identified, the following subsections highlight the influence of the airfoil span, the convective schemes, and the chosen SGS length scales on the dynamics and resolution of the wake. The insights drawn from these subsections aid the identification the appropriate convective scheme and the SGS length scale to obtain the

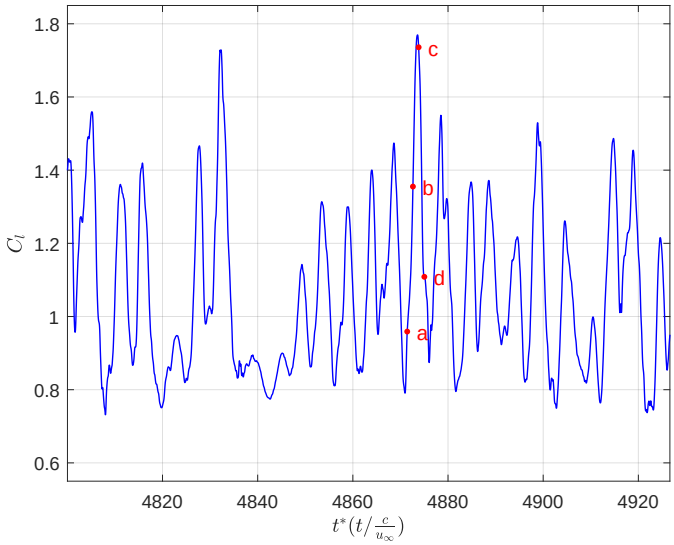

Figure 5.14: Time series of mid-span sectional Cl corresponding to vorticity contour instances in figure 5.12. a,b,c,d indicate the time instances referred in figure 5.12.

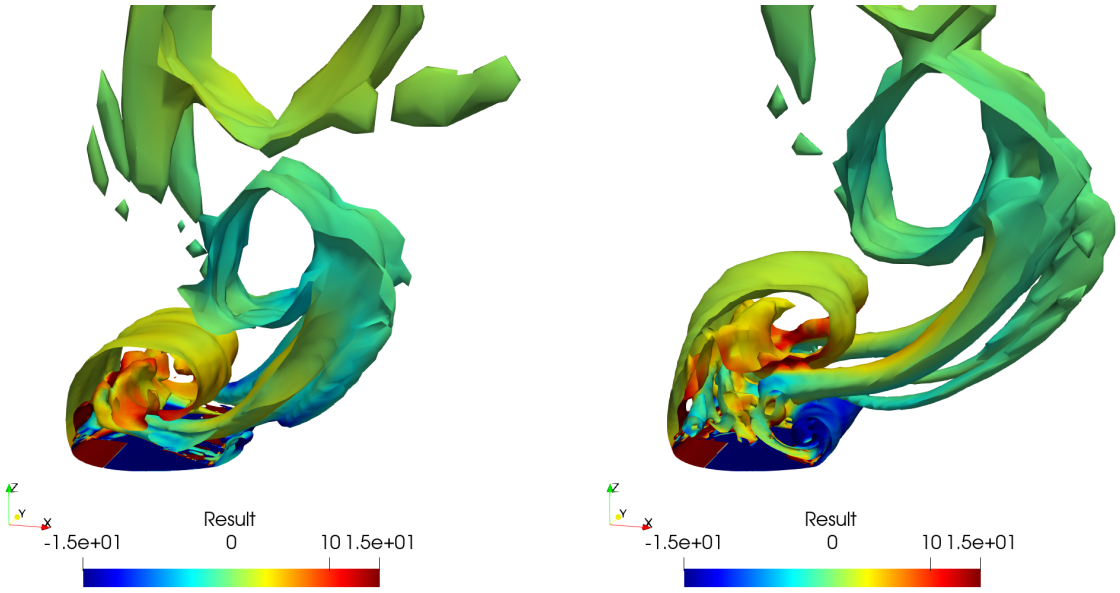

(a) 4873.8 CTU

(b) 4875 CTU

Figure 5.15: Iso-surfaces of Q criterion $\left(Q = 0.1 * u_\infty^2/L_y^2\right)$ colored by non-dimensional vorticity.

dynamic surface pressure data, which will help yield the estimate of the far-field separation-stall noise caused by airfoils in deep stall.

5.2.6 Influence of Span Sizes

A NACA0021 airfoil of span $7.2c$ has been used in the wind-tunnel experiments carried out by Swalwell [13] to generate static and dynamic data such as the time-averaged surface pressure coefficient distribution and the time series of the coefficients of the aerodynamic lift, drag, normal, and tangential forces for the airfoil in angles of attack from $0°$ to $90°$. The primary step in obtaining acoustic data for this case from the current DDES-FWH framework is to establish that the physical phenomena in the deep stall regime are accurately captured by the simu-

lation procedure being followed. The computationally expensive nature of DDES simulations renders the simulation of such configurations impracticable; thus, it has been a general practice in the literature to simulate the deep-stall test case with an airfoil configuration having a span of $1c$ [12] [40] [41]; this practice has gained further traction following the evaluation of the time-sample and span size effects by Garbaruk [17]. The scope of this section is to validate the DDES simulation procedure described in the subsection 5.2.1 and justify the practice of choosing an airfoil of a smaller span for further analysis.

Two-point spanwise correlations

DES simulation of the $\alpha = 60°$ NACA0021 deep stall test case with span sizes $L_y = 1c$ and $L_y = 4c$ were performed by Garbaruk [17], the ensuing plot of two-point correlation of the local velocity components u, v and w in the spanwise direction is shown in figure 5.16. Mid-span locations at the leading edge separation point and in the near wake were chosen to evaluate the correlation function $R_{ii}(z)$. Large spanwise coherence lengths can be identified from the correlation trends of the wall parallel and normal velocities (u and v) for both the span sizes, but the coherence value is relatively higher in the $1c$ span. An anti-phase relationship exists for the spanwise velocity w for the $1c$ span, whereas in the wake of the airfoil with a larger span, the same component of velocity is incoherent for points being separated by a distance of more than $1c$.

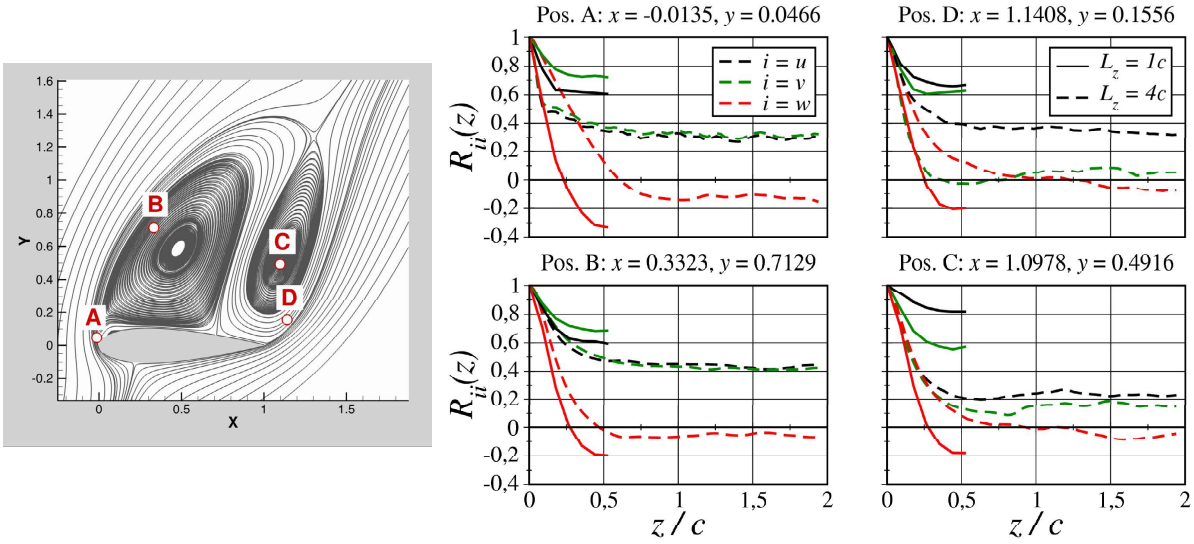

Figure 5.16: Comparison of two-point spanwise correlation of velocity components u, v and w for airfoils with spans sizes of $1c$ and $4c$ [17].

Influence of primary vortices on the time-varying integral coefficients

In an LES study of the deep-stall test case, Park [45] simulated the flow around airfoils of span $1c$, $2c$, $4c$ and $7c$. By plotting the time-averaged pressure contours, they deduced that an increase in span L_y resulted in the primary vortices moving further away from the airfoil surface and a reduction in the extent of the pressure drop in the recirculation region. Thus, a weakened influence of the primary vortices on the time-series of the integral coefficients was established with the increase in span size. They also identified that the flow field in the wake of the $1c$ case involved highly anisotropic secondary vortices; on the contrary, the $4c$ span's wake contained more isotropic structures.

Validation of time-varying sectional aerodynamic force coefficients and time-averaged surface pressure distribution

The available experimental data only correspond to the time-average surface pressure distribution and the time-series of C_l, C_d, C_t and C_n. The PSD of the experimental lift is also routinely compared to verify the correct spectral trends in the simulation; for this purpose, one of the recommendations issued during the DESider project [41] is to use the sectional lift coefficient instead of the full span integral lift coefficient (determined by the pressure distribution on the whole airfoil) to obtain a better comparison with the experiment. In addition, spanwise averaging of the force spectra is recommended to reduce the broadband noise in the power spectrum. The PSD of the experimental lift corresponds to that derived by calculating the dynamic lift signal from the B2 tapping location in figure 2.19a. The same approach is followed here by integrating the time-varying pressure signal at different spanwise sections as per the integral approach explained by Anderson [60]; this procedure is rather straightforward and is explained in the appendix A.1.2. The power spectra obtained at the individual spanwise sections are averaged to obtain the final lift power spectrum, which is representative of the dynamics captured in the simulated test cases. For the $5c$ geometry, eight individual spanwise sections are considered for plotting the spanwise averaged power spectrum of the lift coefficient, and four spanwise sections are considered for the $1c$ geometry. For the $5c$ case, which involves a relatively significant variation of coherence along the spanwise direction, the PSD should be sectional averaged to get a broadband agreement of the magnitude of the PSD with the experiment at the primary shedding peak and its harmonic. The PSD plotted with the help of the dynamic full-span lift has a magnitude that is underpredicted in the entire range of resolved frequencies. The plot comparing the PSD's obtained from the experimental time series, full-span lift, and the spanwise averaged sectional lift for the $5c$ span is given in the figure A.5. It has been noticed that the magnitude of non-dimensional PSD is consistently underpredicted at all frequencies other than the primary shedding peak and its first harmonic. For the $1c$ case, the discrepancy between the PSD obtained from the integral lift and the spanwise averaged PSD is not as significant; this is justified as the primary vortices are almost coherent through the spanwise extent of the domain.

In a bid to ensure the validity of the deep-stall flow solution in the current study, it is required to match the time-averaged statistics and spectral characteristics found in the experiment [13]. Airfoils of span $1c$ and $5c$ are considered for this purpose. Based on the insights drawn from the literature discussed previously in section 2.7.3, the DDES approach adopted in this study is said to be validated when the result from the $5c$ case (Case 5) is in better agreement with the experiment than the result from the $1c$ case.

Cases 4 and 5 mentioned in the table 5.6 are considered for this purpose because the SLAU2 convective scheme and the Δ_{SLA} SGS length scale are found to be optimal in capturing the dynamics associated with deep stall. The reasons behind the choice of the convective scheme and the SGS length scale definition are mentioned in subsection 5.2.7 and subsection 5.2.8. The time-variation of the lift and drag coefficients at section $y/c = 0.363L_y$ for the timespan 4800-5200CTUs are given in figure 5.17a and figure 5.17b. Both the lift and drag time series reflect the predictions found in the literature, as the variation of the sectional lift and drag coefficient is relatively more contained for the $5c$ span than the $1c$ span. The mean and standard deviation of the lift and drag coefficients along with the chord-based Strouhal number $St = (fc/u\infty)$ of vortex shedding St_1 and its first harmonic St_2 are compared with the experiment in table 5.7. Both the time-averaged sectional lift and drag coefficient predictions are within 3.5% for the $5c$ span, whereas the overprediction with the $1c$ span amount to about 25%. The time-averaged pressure coefficient distribution on the airfoil surface is compared between cases 4, 5, and the experiment in the figure 5.17d. Excellent agreement is found on the pressure side due to the attached boundary. The attached boundary layer is modeled by RANS, and it is well known that RANS does provide accurate results for attached flows. It is also apparent from this figure that pressure-drop on the suction side for the $1c$ span is more when compared

to the same for case 5; thus, it explains the consistent overprediction of the lift coefficient for the airfoil with the shorter span.

The spanwise-averaged sectional lift PSD for cases 4 and 5 are compared with the same from the experiment in figure 5.17c; for this, the Welch's method is used. The lift and drag signals are split into four segments after considering an overlap of 50% between each segment; they are then windowed by the Hamming window. The signals are sampled at the non-dimensional frequency $33.33c/u_\infty$, which is the inverse of the simulation time step. The resulting spectra are non-dimensionalized and plotted. The plot reflects the expected trend of consistent overprediction in the PSD magnitude for case 4.

On the other hand, in case 5, the PSD magnitude is overpredicted at frequencies lower than the vortex shedding frequency and overpredicted at higher frequencies. Nevertheless, the discrepancy in the results of case 5 is relatively lower. The primary shedding frequency predicted by both the span lengths is the same and is within 2% of what is observed in the experiment and other DDES validation exercises 2.25 as per the values of St_1 in table 5.7. The frequency of the first harmonic St_2 is also accurately captured, but the reason behind the better prediction for the $1c$ span is unknown.

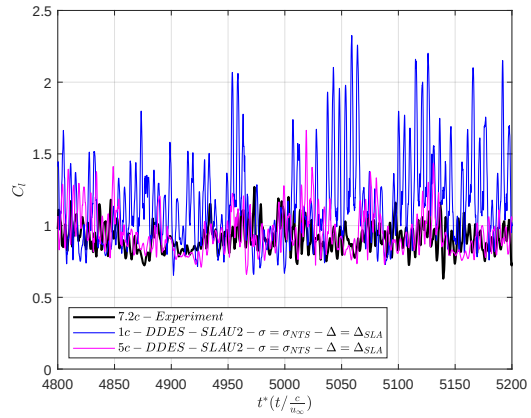

(a) C_l time history

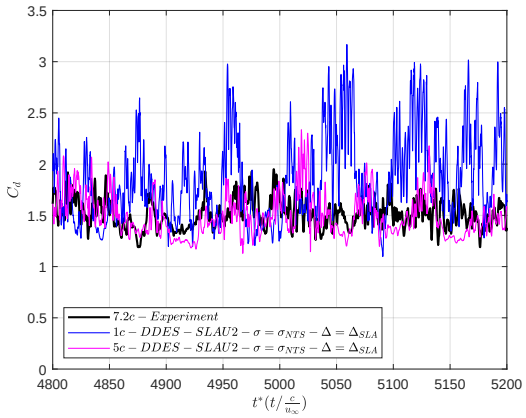

(b) C_d time history

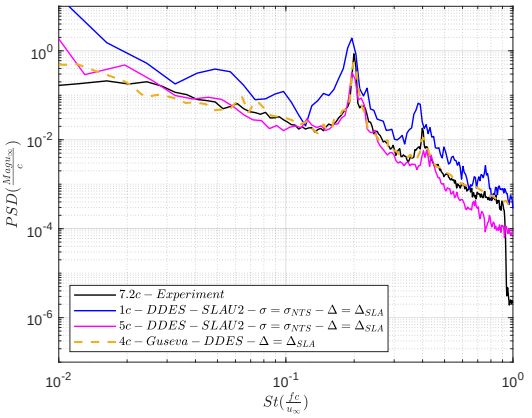

(c) Non-dimensional power spectra of C_l

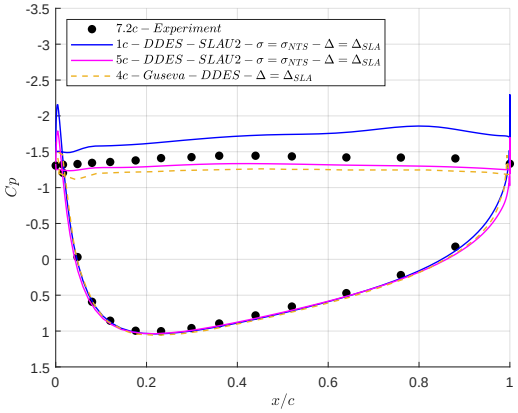

(d) Time averaged Cp at section $y/c = 0.363L_y$

Figure 5.17: Comparison of time variation of integral coefficients C_l, C_d and C_l power spectra for the deep stall cases of spans $1c$ and $5c$

From the analysis made in this section, the objectives set for the study comparing the airfoils of different spanwise extent have been achieved, thereby enabling a successful validation of the DDES approach undertaken. Furthermore, it can be concluded that the dynamics in the near wake are captured accurately and the increase in the spanwise extent does aid in getting better predictions of the time-averaged and spectral properties of the section lift and drag

coeffiecients. Going by the reasoning given for the general overprediction of the time-averaged and spectral characteristics for the airfoil with the $1c$ span, it is valid to state that the flow solution in case 4 does capture the physics of vortex shedding in deep stall. Thus, it would be appropriate to choose the airfoil with smaller span for evaluating the effects of different SGS length scales and the convective schemes.

	$\overline{C_l}$	$\overline{C_d}$	St_1	St_2	σ_{C_l}	σ_{C_d}
Experiment[13]	0.9156	1.5363	0.1993	0.3987	0.0951	0.1587
DDES $1c - \Delta_{SLA}$	1.1507	1.8396	0.1953	0.3824	0.3056	0.4083
DDES $5c - \Delta_{SLA}$	0.9474	1.4898	0.1953	0.4036	0.1440	0.1976
Guseva $4c - \Delta_{SLA}$[18]	-	-	0.1988	0.4052	-	-

Table 5.7: Comparison of integral coefficient statistics

5.2.7 Influence of convective schemes

The merits of choosing an upwind/central hybrid inviscid scheme are apparent from the discussion made in the subsection 4.1.3; the current analysis is complementary to it as it further proves the need for convective schemes with low artificial dissipation in the LES region; results from deep stall test cases 1 and 2 are analyzed to substantiate this argument. The Δ_{max} SGS length scale is used in both the cases to make it an apt comparison. It should be noted that the SLAU2 scheme already offers lower numerical dissipation [56]; thus, utilizing the low dissipation modification of Travin(σ_{NTS}) with SLAU2 would mean that case 2 would involve significantly lower artificial dissipation in the LES region relative to the pure upwinding utilized in case 1.

The dissipative nature of the Roe scheme results in a downstream recirculation region in the near wake, that shows a strong drop in pressure relative to the flow solution obtained with the SLAU2 scheme in case 2; this can be observed in the contour plots of the time-averaged pressure shown in figure A.4a and figure A.4b. Another consequence of the relative significant pressure drop is that the surface pressure coefficient on the suction side of the airfoil is underpredicted significantly when compared to case 2 and the experiment as observed in figure 5.18d. It is also observed that the length of the massively separated wake region is higher for case 1 than all the other deep stall cases having a span of $1c$.

The relatively large pressure drop exacerbates the lift signal as observed in the figure 5.18a. The lift signal for the case involving SLAU2 also shows bursts of large values of the lift coefficient; this is due to the stochastic nature of the vortex shedding process that exhibits weak and strong modes of vortex shedding [41]. The span size is also a contributing factor, as discussed earlier. It is also observed in the lift and drag time series that the predicted vortex shedding modes in case 1 are generally strong as the sectional lift and drag coefficients are consistently overpredicted compared to that from the experiment and case 2. Thus, it is natural to expect that the magnitude of the PSD of the sectional lift is overpredicted for case 1 in comparison with the experiment and case 2; this is clearly observed in the figure 5.18c. The shedding frequency of the primary leading and trailing edge vortices St_1 is underpredicted by the solution in case 1 by 6% as observed in table 5.2.8. It is seen in the table that all the statistical parameters determined from the flow solution obtained by an upwind discretization of the convective fluxes compare poorly with the experiment, in contrast to the flow solution obtained by a hybrid upwind/central difference scheme.

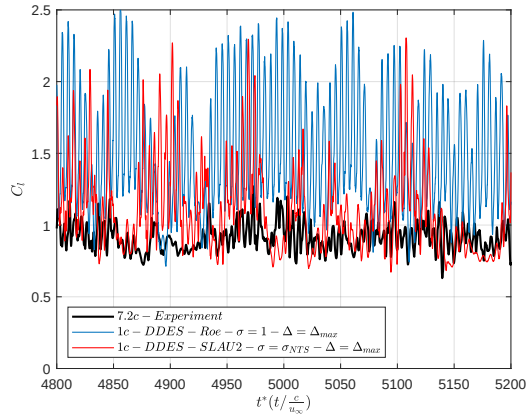

(a) C_l time history

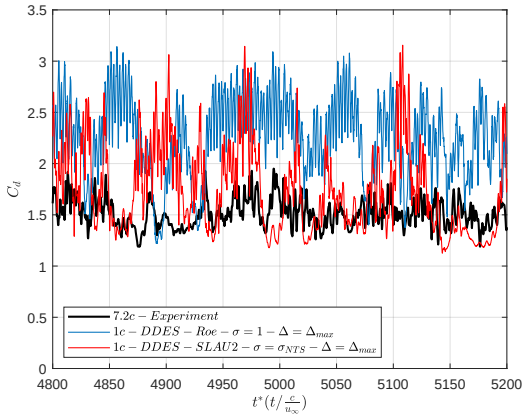

(b) C_d time history

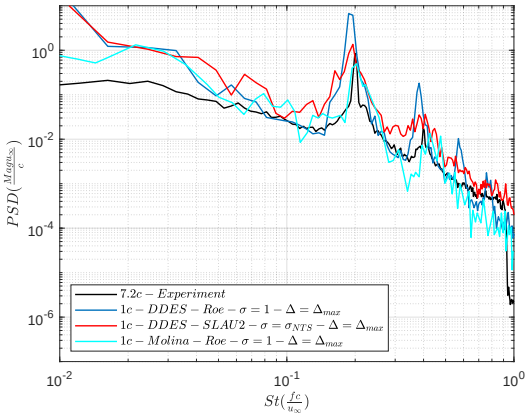

(c) Non-dimensional power spectra of C_l

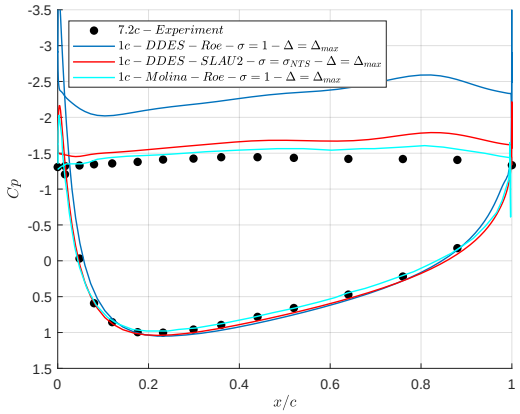

(d) Time averaged Cp at section $y/c = 0.363L_y$

Figure 5.18: Comparison of time variation of integral coefficients C_l, C_d, C_l power spectra and the time averaged distribution of the pressure-coefficient for the case of span $1c$ with convective schemes of different levels of disspiative nature

	$\overline{C_l}$	$\overline{C_d}$	St_1	St_2	σ_{C_l}	σ_{C_d}
Experiment[13]	0.9156	1.5363	0.1993	0.3987	0.0951	0.1587
DDES $\Delta_{max} - Roe$	1.5007	2.2625	0.1871	0.3824	0.4066	0.3840
DDES $\Delta_{max} - SLAU2$	1.1110	1.7606	0.1953	0.4069	0.3143	0.4264
Molina $\Delta_{max} - Roe$[43]	-	-	0.2028	-	-	-

Table 5.8: Comparison of integral coefficient statistics between deep stall test cases 1 and 2.

The PSD of the sectional lift from case 1 (figure 5.18c) contains multiple harmonics of the vortex shedding peak, which is not present in the sectional PSD of the experimental lift and of case 2. Molina [43] in their validation study also performed the DDES simulation of case 1, but the same trends were not observed as the primary vortex shedding frequency was accurately predicted along with the PSD magnitude. A possible explanation for the discrepancy between the solution obtained by Molina [43] using the Roe scheme and case 1 would be that a relatively fine mesh was used by Molina [43] which reduced the amount of the artificial dissipation.

It would also be beneficial to qualitatively prove that the flow solution in the current scenario is influenced by the degree of upwinding rather than the underlying grid-based SGS length scale Δ_{max}. In the figure 5.19a, the LES region can be identified by the marked increase in the time-averaged non-dimensional eddy viscosity in the region downstream of the airfoil. It is observed that the eddy viscosity increases gradually in the downstream direction; this is

consistent with the grid-based definition of Δ_{max} as the larger and more isotropic elements in the far-field result in the decrease of the DDES modified wall distance 2.17, which reduces the magnitude of the destruction term in the SA model equation 2.13 (which is also the dynamic SGS model equation); thus causing a gradual increase of the eddy viscosity in the downstream direction. The same explanation holds for the distribution of the non-dimensional eddy viscosity for case 2, as per the distribution of the time-averaged non-dimensional eddy viscosity contour shown in figure 5.20a. However, in case 2, the value of non-dimensional eddy viscosity is significantly larger than than that in case 1. The shear rate tensor, which is the primary contributor to the production term in the SA turbulence model equation 2.13 is under predicted when artificial dissipation is prominent; thus, the resulting SGS viscosity and eddy viscosity would be lower in case 1 in comparison to case 2, proving that the flow solution is affected primarily by the dissipative Roe scheme.

It is known that the Roe scheme being dissipative does not provide good resolution of the structures in the LES region. Lower artificial dissipation in the LES region can be expected by using the SLAU2 scheme along with the low dissipation modification σ_{NTS}, which would then be beneficial in resolving the flow in the near wake of the current deep stall test case. This is confirmed by plotting the iso-surfaces of Q-criterion for cases 1 and 2; this is done in figure 5.19b and figure 5.22a, which are colored by the non-dimensional spanwise vorticity $\omega_y c/u_\infty$. It is noticed that very few scales other than the primary leading and trailing edge vortices are resolved in case 1 compared to case 2.

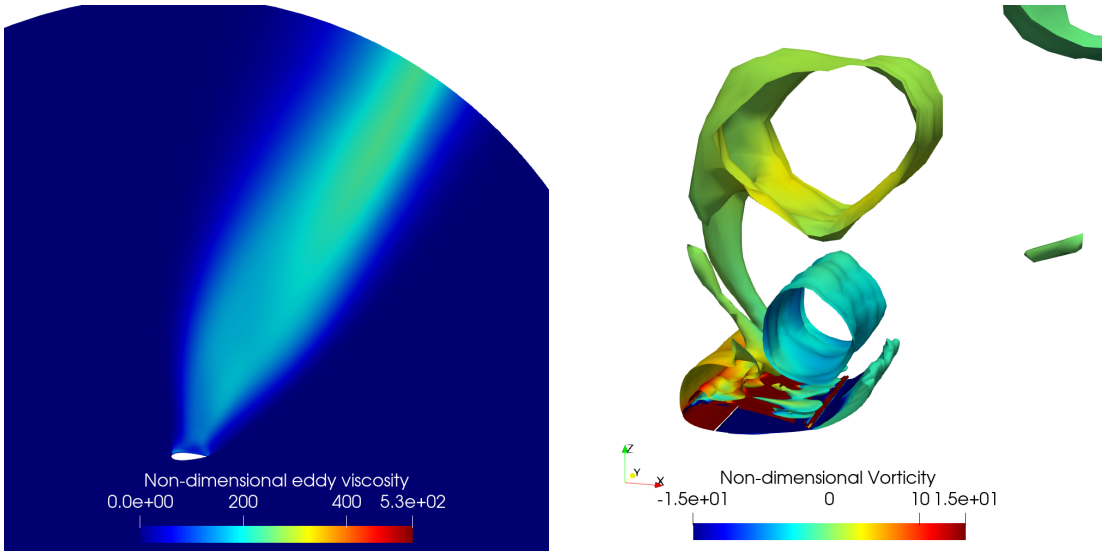

(a) Contour plot of μ_t/μ

(b) Iso-surfaces of Q criterion

Figure 5.19: Contour plot of the non-dimensional eddy viscosity and iso-surfaces of Q criterion $\left(Q = 0.1 * u_\infty^2/L_y^2\right)$ for the Δ_{max} case with the Roe scheme

Based on the static, dynamic, and spectral analysis carried out in this subsection, it can be concluded that choosing a convective scheme with low artificial dissipation is vital for accurately capturing the deep stall's physical phenomena. In the current scenario, choosing the SLAU2 scheme with the modification σ_{NTS} will be appropriate to obtain the dynamic surface pressure data for acoustics post-processing.

5.2.8 Influence of Sub Grid Length Scales

In the previous subsection, the influence of artificial dissipation on the massively separated wake has been ascertained, following which the hybrid upwind/central-difference SLAU2 scheme is chosen for further flow simulations. It is now important to evaluate the different SGS length

scales implemented in SU2 for the given mesh and choose the appropriate SGS length scale that results in the best resolution of the flow given the coarseness of the considered mesh. The dynamics in the near field on the suction side have a major influence on the dynamic loading of the airfoil surface, which is transported to the far-field as noise.

It should be mentioned that the combination of the SLAU2 [56] convective scheme and Travin's low dissipation modification (σ_{NTS}) [58] did not yield a converged solution for the case involving the Δ_ω SGS length scale, which is why the JST [54] scheme was used to discretize the convective fluxes. JST, a purely central difference scheme, should provide a resolution in the near wake that is comparable to what is achieved by SLAU2.

The time-averaged plots of the non-dimensional eddy viscosity μ_t/μ for the SGS length scales Δ_{max}, Δ_ω, and Δ_{SLA} are shown in the figure 5.20. An observation consistent with the theory is obtained as a marked decrease of eddy viscosity is observed in the massively separated wake region (in figures 5.20b and 5.20c) when the flow variables are included in the definition of the SGS length scale. The grid-dependent nature of Δ_{max} means that as the cells become progressively large and anisotropic in the far wake region, the destruction term in the SA model equation 2.13 is weakened due to the increased modified wall distance $\tilde{d}$ (given in equation 2.17). The eddy viscosity in the near wake is comparable between both Δ_{max} and Δ_ω. However, it is also interesting to note that Δ_ω predicts the largest value of eddy viscosity in the near wake; this stems from the definition of Δ_ω which in the recirculation region would predict a large value of the $\tilde{d}$ as the vorticity vector would be nearly parallel to the spanwise direction because of the highly coherent vortices shed at the leading and trailing edges, making $\tilde{d}$ dependent on $\sqrt{\Delta_x \Delta_z}$. The Δ_{SLA} is formulated to be applicable in anisotropic grids [42]; the resulting flow solution in case 4 exhibits the lowest value of the eddy viscosity in the entire wake region. It is apparent from figure 5.20c that the time-averaged eddy viscosity is comparable at all the locations in the massively separated wake region; thus, Δ_{SLA} should be the choice of SGS length scale for acoustics as it would enable a more accurate description of the flow physics and also provide the best resolution in terms of the turbulent length scales.

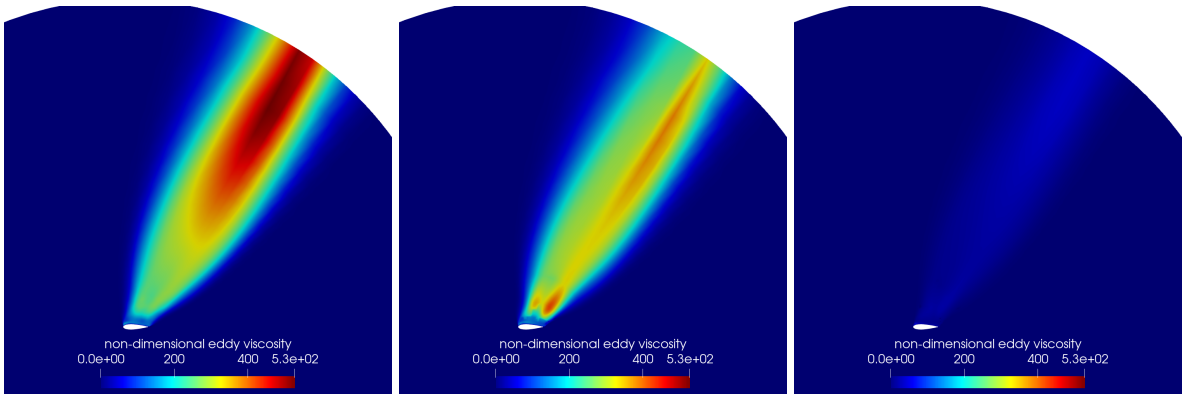

(a) Δ_{max} (b) Δ_ω (c) Δ_{SLA}

Figure 5.20: Comparison of time averaged non dimensional eddy viscosity contours (ν_t/ν) on the mid-span plane $y/L_y = 0.5$

It is known from the literature referred to in subsection 2.8.4 and subsection 2.8.5 that both Δ_ω and the Δ_{SLA} are formulated to help reduce the local eddy viscosity in the initial regions of the shear layer, thereby enabling its accelerated roll-up and transition to turbulence by faster development of the KH instabilities. As observed in figure 5.20, the predicted eddy-viscosity is highest and comparable for the test cases 2 and 3, where Δ_{max} and Δ_ω are utilized. The accelerated roll-up does not influence the wake shape or the pressure-drop in the near wake as per the contour of time-averaged pressure in figure A.4; this means that the accelerated roll-up will not have any impact on the airfoil loading. This is confirmed by the distribution of the

pressure coefficient for all the three cases in figure 5.21d.

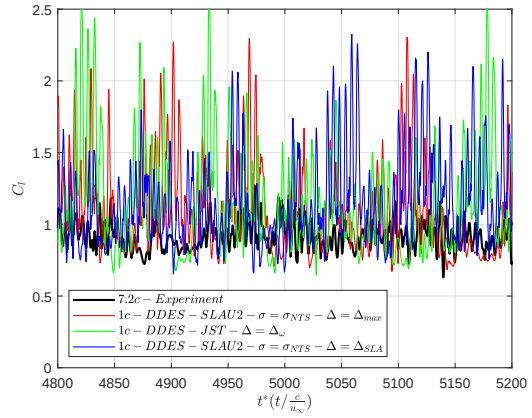

(a) C_l time history

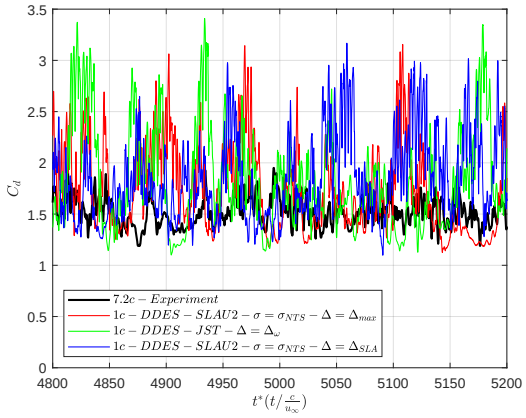

(b) C_d time history

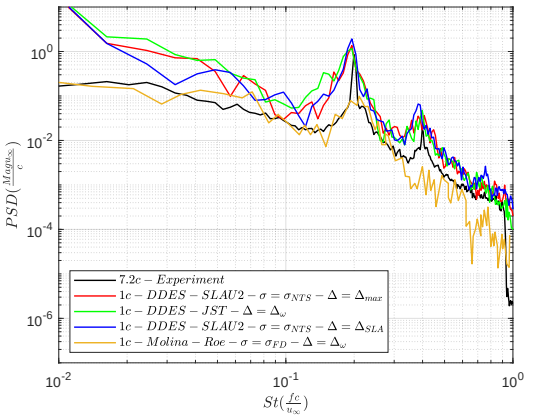

(c) Non-dimensional power spectra of C_l.

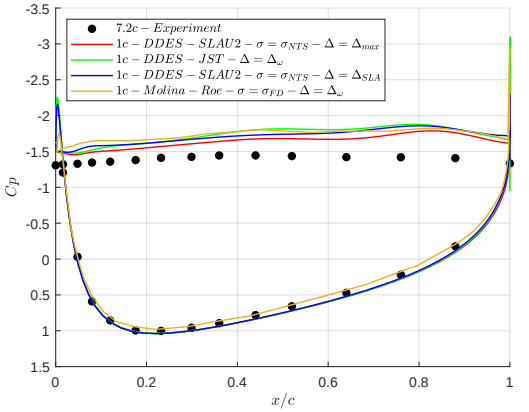

(d) Time averaged Cp at section $y/c = 0.363L_y$

Figure 5.21: Comparison of time variation of integral coefficients C_l, C_d and C_l power spectra for the deep stall cases with Sub-Grid Length Scales Δ_{max} and Δ_{SLA}

The time-averaged sectional lift and drag coefficients are overpredicted by about 25% and 18% by the all the SGS models as per the values listed in table 5.9. The consistent over-prediction in the mean values is due to the smaller span considered for the DDES simulations. The time series of sectional lift and drag in figure 5.21a and figure 5.21b show that sectional values are comparable for all the three cases. The period of strong and weak vortex shedding modes has been observed to be stochastic in the literature [41], thereby justifying the sudden increase in the lift and drag coefficients. The phase shift in the signals is a virtue of the initial transient, whose time extent differs for each of the considered SGS models as shown in the time series of the integral lift's running average value in figure 5.10a. Considering the nature of the time-variation of the sectional lift and drag in all the three cases, it is expected for the spanwise averaged PSD of the sectional lift to follow a similar trend in all the three cases; this is indeed reflected in the spanwise averaged plots of the power spectra of the sectional lift in figure 5.21c. The spanwise averaged power spectra of the sectional lift nearly overlap for all the SGS lengths scales for frequencies at and above the primary vortex shedding peak St_1. The magnitude of the non-dimensional PSD is overpredicted in the entire range of frequencies; this is due to the use of the smaller span as explained by Garbaruk[17]. As per the statistical values compared in table 5.9. The prediction of the primary vortex shedding frequency is the same in all the three cases and is underpredicted only by 2% relative to the experiment. Furthermore, the frequency of the first harmonic of the primary vortex shedding St_2 also shows excellent agreement with the value from the experimental PSD of the sectional left.

In comparison with the lift PSD obtained by Molina [43] for a case involving the SGS length scale Δ_ω and Roe scheme with Winkler's low dissipation modification σ_{FD} 4.4, the current simulations compare better with the experiment in terms of the PSD magnitude and also the vortex shedding frequency. It should also be noted that the first harmonic of the vortex shedding is not resolved in Molina's section lift PSD plot. On the contrary, the time-averaged surface pressure-coefficient distribution obtained by Molina is similar to what is obtained in the current study, as shown in the figure 5.21d.

	$\overline{C_l}$	$\overline{C_d}$	St_1	St_2	σ_{C_l}	σ_{C_d}
Experiment[13]	0.9156	1.5363	0.1993	0.3987	0.0951	0.1587
DDES Δ_{max}	1.1110	1.7606	0.1953	0.4069	0.3143	0.4264
DDES Δ_ω	1.1509	1.8419	0.1953	0.3987	0.3544	0.4769
DDES Δ_{SLA}	1.1507	1.8396	0.1953	0.3824	0.3056	0.4083
Molina Δ_ω[43]	-	-	0.2105	-	-	-

Table 5.9: Comparison of integral coefficient statistics for the variation in SGS length scales used.

The analysis of the statistics done previously does not provide any insight into the resolution of the scales in the near wake. Given that the convective fluxes in the LES regions are being spatially discretized with central differencing or blended upwind/central difference schemes, the flow resolution would be similar. However, this is not the case because the eddy viscosity prediction in the near wake LES region is highest when the Δ_{max} and Δ_ω SGS length scales are used as per the figure 5.20. Whereas, when the Δ_{SLA} is used, the predicted eddy viscosity is nearly an order of magnitude lower relative to the same prediction by using Δ_{max} and Δ_ω. Thus, very few scales in the near and far wake are dissipated by the SGS viscosity in case 4 when compared to cases 2 and 3; this can also be verified qualitatively by plotting the iso-surfaces of the Q criterion for a given time instance from the flow solution of all the three SGS length scales. Figure 5.22 shows the iso-surfaces of Q-criterion for an instance of the trailing edge vortex being shed. It is observed that the Δ_{SLA} SGS length scale provides the best resolution that can be captured by the current mesh, thereby making it the best choice for the SGS length scale in obtaining the dynamic surface pressure data for acoustics post-processing.

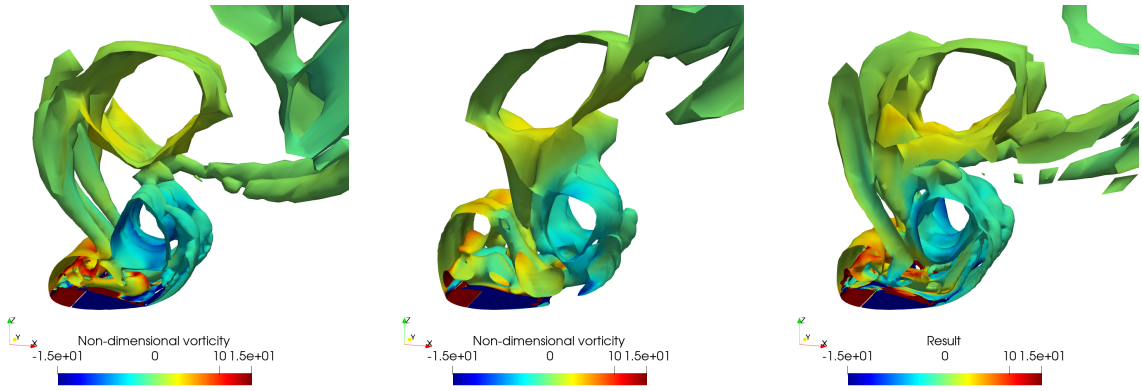

(a) Δ_{max} (b) Δ_ω (c) Δ_{SLA}

Figure 5.22: Comparison of iso-surfaces of Q-criterion $\left(Q = 0.1 * u_\infty^2 / L_y^2\right)$ for an instance of shear layer roll-up at the leading edge obtained using different SGS length scales.

5.2.9 Deep Stall Acoustic Results

The analyses made in the previous section indicate that the SLAU2 convective scheme with the low dissipation modification σ_{NTS} and the SGS length scale of Δ_{SLA} provide the best resolution among the various combinations of convective schemes and SGS length scales investigated; therefore, the flow solution obtained for deep stall test case 4 is used for acoustics post-processing. The surface pressure fluctuations are sampled in the interval of $4800 - 5200\ CTUs$ for every non-dimensional time step $0.03c/u_\infty$; the reason for this has been mentioned in the subsection 5.2.4. Because of the unavailability of the far-field noise data from experimental studies of the current deep stall regime, the observer location distribution has to be assumed; consequently, the observers are assumed to be distributed circularly on the midspan plane $(y/c = -0.5)$ at the radial location $r/c = 20$ from the midpoint of the airfoil chord. The angular spacing between every successive observer is $5°$. The surface normals file (explained in the subsection 4.2.2) is obtained upon post-processing to complete all the user inputs needed for computing the far-field acoustic pressure fluctuations. Quantities such as OASPL and SPL are calculated at the far-field observer locations by using the relations given in the section 4.3. For the current deep-stall flow regime, the far-field OASPL directivity, narrow band SPL spectrum, and the directivity of SPL are generated.

The plot of OASPL is representative of the power in the noise signal. The distribution of OASPL at the considered observer locations is plotted in the figure 5.23a. In this plot, θ corresponds to the azimuthal coordinate measured with respect to the geometric x axis. The power of the noise signal appears to be uniform at throughout 58.14 dB, with no directional bias.

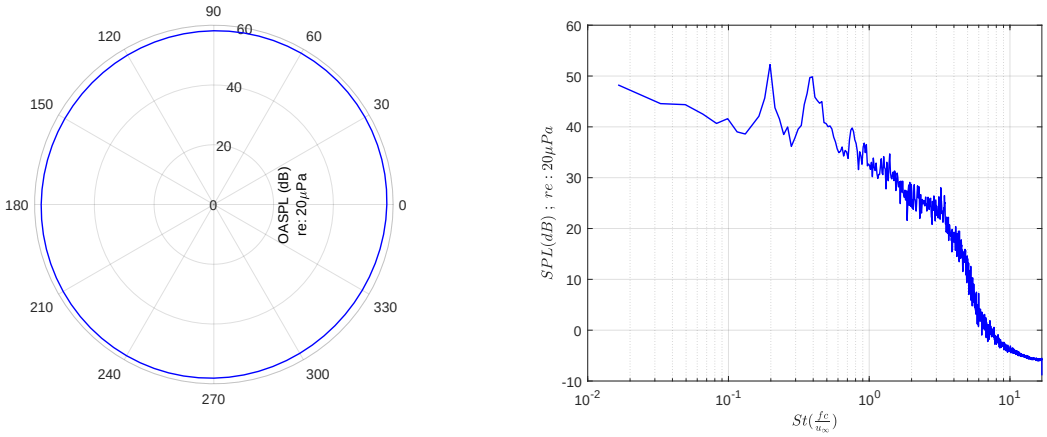

(a) OASPL directivity

(b) Narrow band SPL spectrum.

Figure 5.23: (a) OASPL directivity with observers at $r/D = 20$. (b)SPL spectrum at observer located at $r/c = 20$ and $\theta = 90°$.

Separation-stall noise is characterized by an increase in the low frequency noise [8] [36]. For airfoils in deep stall, two tonal peaks at low frequencies have been observed by Moreau [9]; the narrow band frequency spectrum (SPL spectrum) plotted in figure 5.23b obtained at the observer perpendicular to the airfoil chord on the midspan plane exhibits these features.

Moreau [9] having investigated the NACA0018, NACA-65-1210, flat plates and other airfoils in deep stall, proposed frequency scaling, which involved scaling the Strouhal number with the separation bubble thickness h as $St = fh/u_\infty$. The PSD scaling in terms of $(h/c)^{-4}/\left(u_\infty^5 \zeta^2\right)$ resulted in the normalized spectra shown in the figure 5.24b in which the Strouhal scaled low frequency tones are 0.2 and 0.4 respectively. Here, ζ refers to the ratio of chord lengths. The same procedure, when followed for the NACA0021 in deep stall, results in the plot of the normalized spectrum depicted in figure 5.24a; in this plot, when the chord

length is used for scaling the frequency, the tonal peaks are at Strouhal numbers of 0.2 and 0.4, however; it is not equivalent to using the separation bubble thickness. Swalwell [13] and Moreau [9] suggested the use of $csin(\alpha)$ as the typical vortex shedding length scale, which, when used, results in the Strouhal numbers of 0.17 and 0.34 for the tonal peaks, which is still in line with the normalized experimental PSD. The discrepancy of about $20\ dB$ in the magnitude of the normalized PSD is due to the different span sizes $(1.625c - 3c)$ used in the experiment and the NACA0021 deep stall test case $(1c)$. Kato's long span correction formula [61] can be used to account for the difference in the magnitude of the normalized PSD between the current study (figure 5.24a) and the experiment (figure 5.24b); this has not been pursued here.

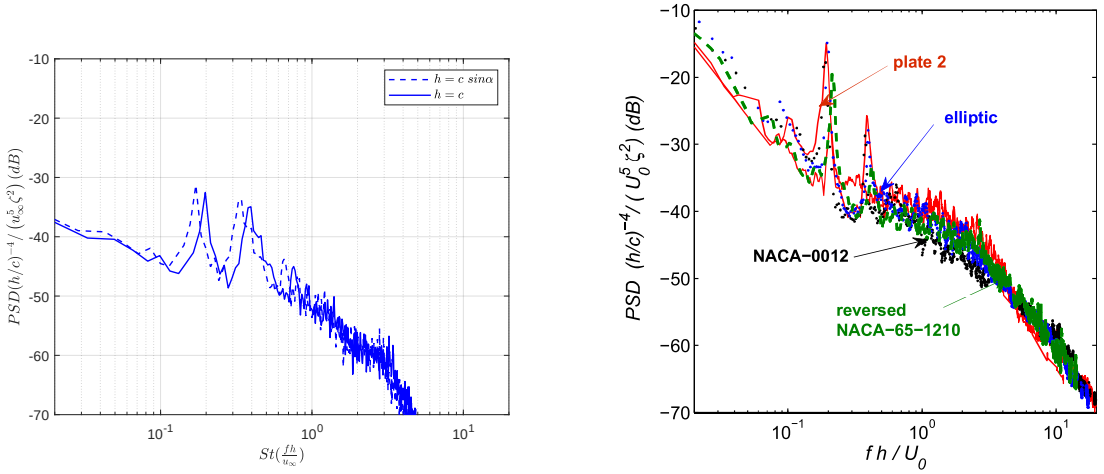

(a) Normalized spectrum as per Moreau [9]. (b) Normalized noise spectra from experiments [9].

Figure 5.24: (a) Noise spectra in accordance with the deep stall scaling of Moreau [9]. (b)Scaled noise spectra obtained for various deep stall test cases investigated experimentally by Moreau [9].

The SPL directivity at different chord-based Strouhal St and Helmholtz kc numbers are given in the figure 5.25. At low frequencies of $St = 0.0165$ and $St = 1.2507$, the airfoil is a compact source; the resulting directivity of the acoustic field is dipolar and is symmetric in the top and bottom half-planes. The dipole pattern persists at Strouhal numbers of $St = 2.4850$ and $St = 3.7193$, but the noise level is relatively higher in the upper half-plane. At the medium frequencies where the airfoil transitions to a non-compact source at Helmholtz numbers $kc = 0.8964$ and $kc = 1.1197$, backscattering is observed in figure 5.25e and figure 5.25f.

It can be concluded that a physically consistent acoustic solution is obtained for the NACA0021 test case with the help of the DDES-FWH framework. The elevation of noise levels at low frequencies typical of separation-stall noise has been captured. The narrow band SPL spectrum of the NACA0021 airfoil, when normalized as per the literature [9] results in good agreement with the tonal frequencies of the experimental test cases, although dependence on the length scale h is observed. A marked discrepancy in the magnitude of the normalized PSD with the literature is noticed; this is speculated to be a consequence of the difference in the span size of the experimental geometries and the $1c$ span NACA0021 airfoil. This can either be remedied by using a long span correction formula or by obtaining noise predictions from a flow solution involving a span size that is comparable with that used in the experiments.

In this section, the DDES-FWH framework has been successfully applied to obtain the far-field noise data for the case of a NACA0021 in deep stall. Although the noise data has not been precisely replicated, the characteristics of the separation-stall noise signature associated with low Reynolds number turbulent flows have been captured. The well-documented effect of the airfoil's span size on the flow solution's statistical and spectral parameters is replicated, validating the numerical setup for DDES. Convective schemes that are inherently dissipative pro-

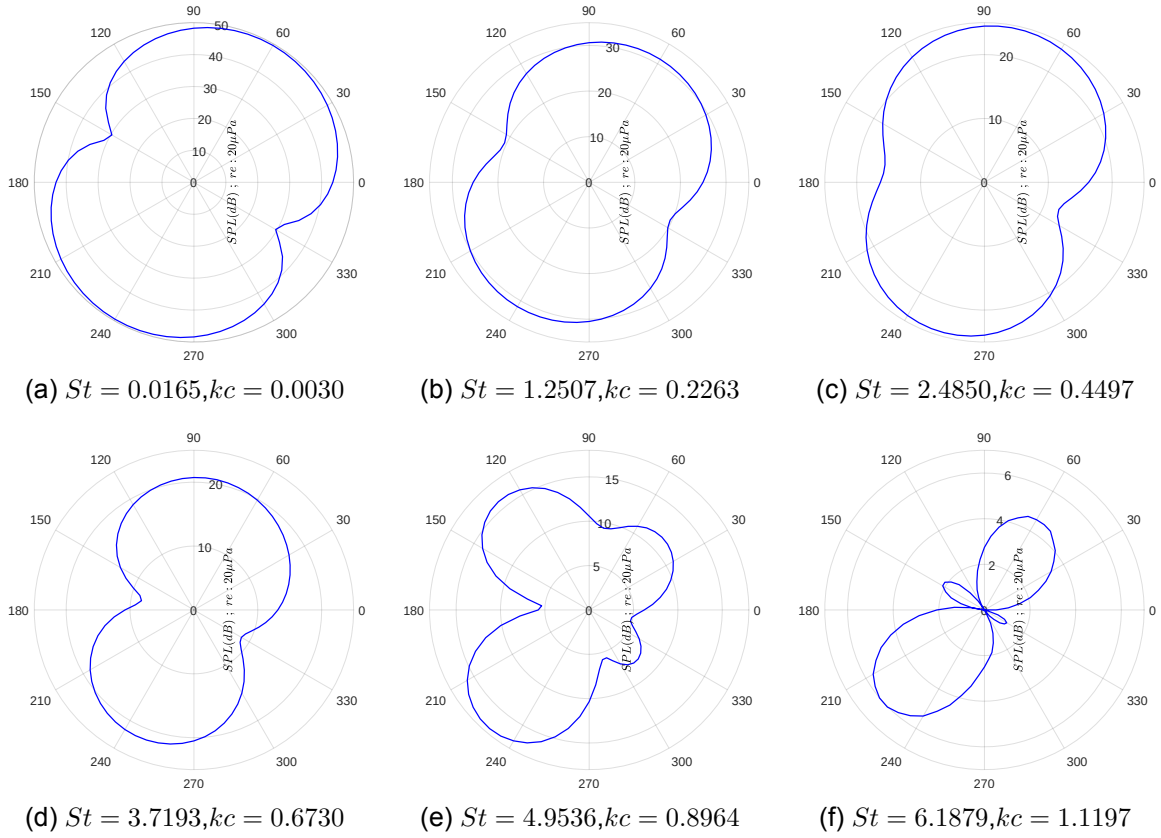

(a) $St = 0.0165, kc = 0.0030$ (b) $St = 1.2507, kc = 0.2263$ (c) $St = 2.4850, kc = 0.4497$

(d) $St = 3.7193, kc = 0.6730$ (e) $St = 4.9536, kc = 0.8964$ (f) $St = 6.1879, kc = 1.1197$

Figure 5.25: SPL directivity at low and medium frequeencies $r/c = 20c$.

vide an underresolved unphysical flow solution, making their use counterintuitive for the purpose of acoustics post-processing. It is rather advisable to use a hybrid central-difference/upwinding scheme such as SLAU2 with a low dissipation blending function σ_{NTS} to ensure a physically accurate flow solution. The nature of the deep stall test case is such that the development of the KH-instabilities in the initial shear layer is not delayed even with the use of a grid-based SGS length scale Δ_{max}. Hence, all the three SGS length scales have accurately captured the vortex shedding phenomenon; Δ_{SLA} is found to provide the best resolution of the scales in the flow as it is not sensitive to anisotropic cells and coarseness of the grid, making it the optimal choice from which the dynamic surface pressure data can be obtained for acoustics post-processing.

5.3 NACA0018 test case

The deep stall test case studied in the previous section is a natural application of the non-zonal hybrid RANS/LES methods of DES and DDES; thus, it is no surprise that a physically accurate flow solution and noise data were obtained. Now that the DDES-FWH framework has been used to obtain noise predictions for the case of the NACA0021 in deep stall, it can be deemed reliable for obtaining accurate separation-stall noise predictions once the magnitude of the normalized PSD agrees with the experiment [9]. Furthermore, the DDES-FWH framework can be regarded as robust in obtaining noise predictions for the more complex airfoils intrinsic to wind turbine blades if it can provide accurate far-field noise predictions for one other fundamental airfoil self-noise mechanism of turbulent boundary layer trailing edge (TBL-TE) noise.

5.3.1 Test Case Description

The scope of the current section is to investigate the applicability of the DDES-FWH framework to predict the far-field noise produced by the turbulent flow over a profile of the NACA0018 airfoil at 0° angle of attack. The flow is characterized by the chord-based Reynolds number of 2.8×10^5. This geometry has been used as a baseline case in the experiments performed by Carpio [6] to determine the effect of using metal foam trailing edge inserts on the far-field noise; an LBM study to elucidate the mechanisms relevant for noise reduction of the same configurations has been conducted by Teruna [7]. The relevant flow parameters of the test case are listed in table 5.10. In the experiments performed by Carpio [6], an airfoil of $20\ cm$ chord and $40\ cm$ span is considered. In the LBM study of Teruna , the simulation of an airfoil of $20\ cm$ chord and $8\ cm$ span is undertaken. The baseline cases in both the experiment and the LBM simulation involve boundary layer tripping on both the pressure and suction sides. The tripping is carried about by distributing carborundum particles of $0.84\ mm$ diameter on a $10\ mm$ strip. In the LBM study, zig-zag strips are placed at the chord-wise location of $0.2\ c$ from the leading edge on both suction and pressure sides with height $0.6\ mm$ and amplitude $3\ mm$.

Parameter	Value
Chord-based Reynolds number (Re_c)	2.8×10^5
Chord length (c)	1 m
Span (L_y)	0.1 m
Angle of attack (α)	0°
Free-stream Mach number M_∞	0.06
Free-stream turbulence intensity l_u	0.1%

Table 5.10: Flow parameters for the NACA0018 TBL-TE test case.

Consistency with the literature is maintained in the current DDES study by using a RANS roughness model at the chordwise location $0.2\ c$. A smooth airfoil of the same configuration is also considered. The test cases investigated will be referred to as the rough and the clean cases for convenience.

5.3.2 Simulation Setup

The same numerical settings that were used for the Case 4 of the NACA0021 in deep stall (table 5.6) are used here; the relevant details have been mentioned in the subsection 5.2.1, hence these are not repeated. The reader is directed to refer to the appendix B to get an overview of the numerical settings.

For both the clean and rough cases, a non-dimensional time-step of $0.001\ c/u_\infty$ is found to be optimal for accurately capturing the periodicity of the integral aerodynamic coefficients. A steady-state CFL number of 0.1 is used along with 10 inner iterations to obtain adequate convergence in pseudo-time.

Mesh and Boundary Conditions

The same O-grid strategy has been used to discretize the flow domain, which is of the radial extent $92c$. Adequate clustering of the elements is made at the leading and trailing edges. The grid consists of 3.37×10^6 elements with $N_\theta = 516$, $N_y = 60$ and $N_r = 109$ along the azimuthal, spanwise and radial directions. The first inflection layer is present at $y+ \ 1$. The far-field, periodic boundary conditions, and no-slip and constant heat flux boundary conditions are imposed similarly to the NACA0021 deep stall test case.

5.3.3 Flow Field Results

The attached flow regime simulated for determining the TBL-TE noise does not exhibit a long initial transient as that for the NACA 0021 deep stall test case; thus, the procedure of using the unconverged first and second-order RANS initial solutions is not followed. The unsteady simulation is rather begun from the freestream initial conditions.

The CFD-CAA procedure followed here is similar to that in the previous test case investigations, where the flow solution is matched with the experiment before the sampling of the flow solution for the dynamic surface pressure distribution for obtaining far-field noise predictions. The first parameter that is compared is the time-averaged skin-friction coefficient at the vicinity of the trailing edge on the suction side of the airfoil in figure 5.26a; it is observed in this figure that time-averaged skin friction is consistently under predicted with respect to the data from the LBM study [7] until about $x/c = 0.9$ where, the skin-friction coefficient has a value of 0, indicating flow separation in the current DDES simulations. It is also evident from this figure that the addition of the roughness does not have any tangible effect. The flow separation at the chordwise location on the mid-span plane $x/c = 0.9$ can also be spotted in the time-averaged Cp included in the appendix A.6.

In the context of TBL-TE noise, matching the boundary layer properties in the vicinity of the trailing edge is a crucial first step in ensuring that the correct far-field noise signature is obtained. For this purpose, the boundary layer thickness δ_{99} is evaluated at five chordwise sections from $0.96\ x/c$ to $1\ x/c$. It is seen that both the clean and rough cases result in the same value of the boundary layer thickness δ_{99} and are underpredicted throughout in comparison with the experimental measurements [6].

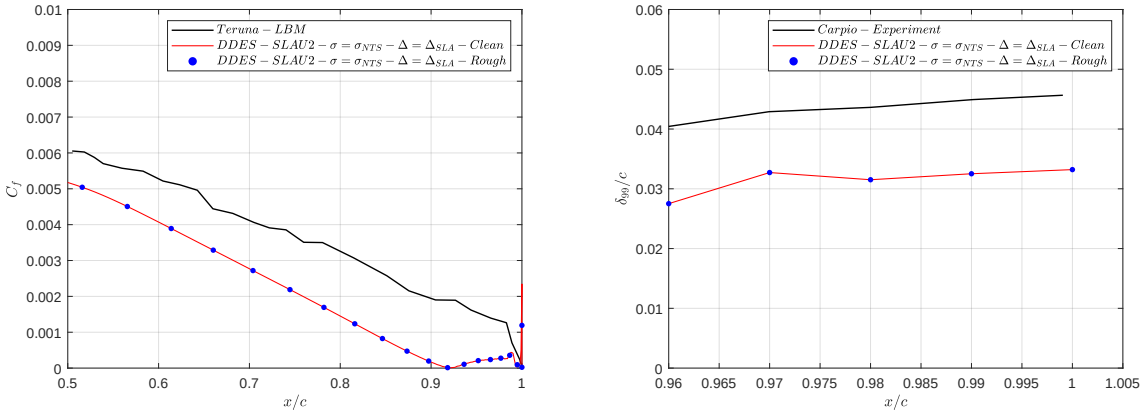

(a) Skin friction coefficient (C_f) comparison. (b) Comparison of boundary layer thickness (δ_{99}).

Figure 5.26: (a) Comparison of mid-span time-averaged C_f in the vicinity of the trailing edge with the same from the LBM study [7]; (b) Comparison of boundary layer thickness δ_{99} to the same obtained from experiments [6].

Based on the flow separation found at the vicinity of the trailing edge, one should expect that profiles of the flow parameters obtained in the DDES simulations will not match the experiment. This is found to be true in the plots of the time-averaged wall-parallel velocity profile $\overline{u}/u_\infty$ and the RMS value of the wall parallell turbulent velocity fluctuations u'_{rms}/u_∞ in figure 5.27a and figure 5.27b.

A significant discrepancy is found in the time-averaged wall-parallel velocity profile at the trailing edge in the figure 5.27a. The flow separation is confirmed by the profile of $\overline{u}/u_\infty$ having negative values of time-averaged wall-parallel velocity close to the wall. The profile of the RMS value of the turbulent wall-parallel velocity fluctuations u'_{rms}/u_∞ in the boundary layer is plotted in the figure 5.27b. The velocity fluctuations are an order of magnitude lower relative

to what is observerd in the experiment.

The overlap of all the results from the DDES simulation with the roughness model and the DDES simulation of the smooth airfoil geometry implies that the extent of roughness is currently inadequate to trip the boundary layer. As the flow physics pertinent to TBL-TE noise is not captured accurately by either the clean or rough cases, it is expected that the far-field noise signature will not match with the experiment. Flow recirculation at the trailing edge would indicate that the resulting far-field noise will be tonal, unlike TBL-TE noise's broadband nature.

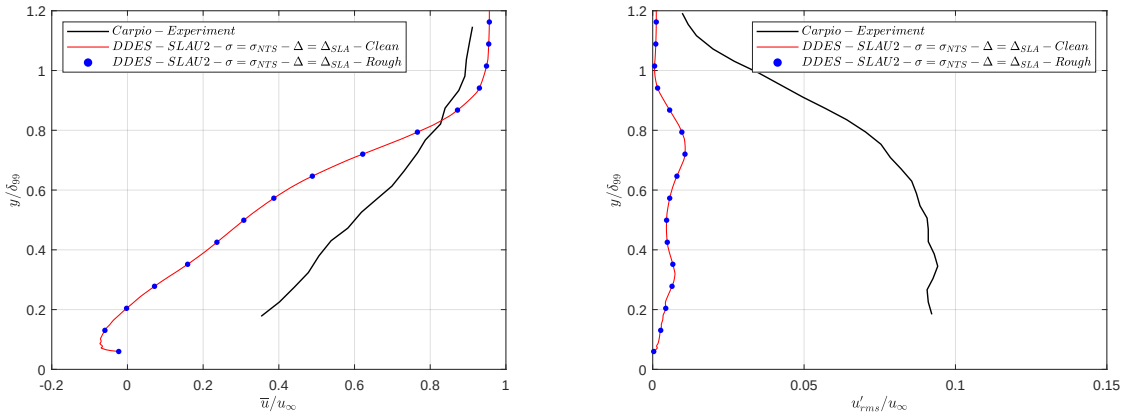

(a) Mean wall parallel velocity $\overline{u}/u_\infty$ profile. (b) RMS of wall paralell turbulent velocity u'_{rms}/u_∞.

Figure 5.27: Comparison with data from wind tunnel studies [6] in terms of (a) Profile of time-averaged wall parallel velocity $\overline{u}/u_\infty$; (b) Profile of streamwise turbulent velocity u'_{rms}/u_∞.

5.3.4 Acoustic Results

After an initial simulation of $135\ CTUs$, the flow solution is sampled at every non-dimensional time-step $0.001\ c/u_\infty$ for a period of 15 flow passes to generate the dynamic surface-pressure distribution data file needed for the FWH solver. The observer locations are distributed circularly at a radial distance of $7.4\ c$ from the airfoil's trailing edge on the mid-span plane. The data obtained from the FWH solver is the far-field acoustic pressure fluctuations; this data is post-processed to generate the narrow band SPL spectrum. Owing to the simulation of a smaller span $0.1\ c$ compared to the experiment ($2\ c$), the resulting narrow band SPL data has to be corrected. This is achieved by using Kato's long span correction forrmula [61] which is given by equation 5.2,equation 5.3 and equation 5.4. In these formulas, $(S_{pp}(f))$ is the value of the narrow band SPL spectrum obtained after scaling the same obtained from post-processing the simulation data, $(S_{pp}(f))_{sim}$ is the narrow band SPL (equation 4.12) obtained by the CFD-CAA simulations, L_{exp} is the span of the experimental geometry, L_{sim} refers to the span considered in the simulation and L_c is the spanwise coherence length which is calculated as per equation 5.1. In equation 5.1, Γ is the coherence function.

$$L_c = \int_{y_1}^{+\infty} \Gamma\left(|y_2 - y_1|, f\right) \mathrm{d}y_2 \tag{5.1}$$

$$\text{If } L_c < L_{sim}, \quad (S_{pp}(f))_{\text{exp}} = (S_{pp}(f))_{sim} + 10 \log \frac{L_{exp}}{L_{sim}}, \tag{5.2}$$

$$\text{If } L_{sim} < L_c < L_{exp}, \quad (S_{pp}(f))_{\text{exp}} = (S_{pp}(f))_{sim} + 20 \log \frac{L_c}{L_{sim}} + 10 \log \frac{L_{exp}}{L_c}, \tag{5.3}$$

$$\text{If } L_{exp} < L_c, \quad (S_{pp}(f))_{exp} = (S_{pp}(f))_{sim} + 20 \log \frac{L_{exp}}{L_{sim}}. \tag{5.4}$$

For the current NACA0018 TBL-TE test case, it is assumed that the flow exhibits low values of coherence in the spanwise direction $(L_c < L_{sim})$. The resulting narrow band SPL spectrum is plotted in the figure 5.28 for the observer located on the mid-span plane at $\theta = 90°$ with respect to the chord of the airfoil and at a distance of $7.4c$ away from the trailing edge. Owing to the presence of separation and recirculation in the vicinity of the trailing edge, the predicted narrow band SPL spectrum is comprised of tonal components, which is in stark contrast with the broadband SPL spectrum obtained in the experiment [6]. Although the magnitude of the SPL at the tonal peaks is comparable with the experimentally obtained broadband SPL spectrum, the current simulation exercise has proven to be futile in accurately predicting the far-field TBL-TE noise.

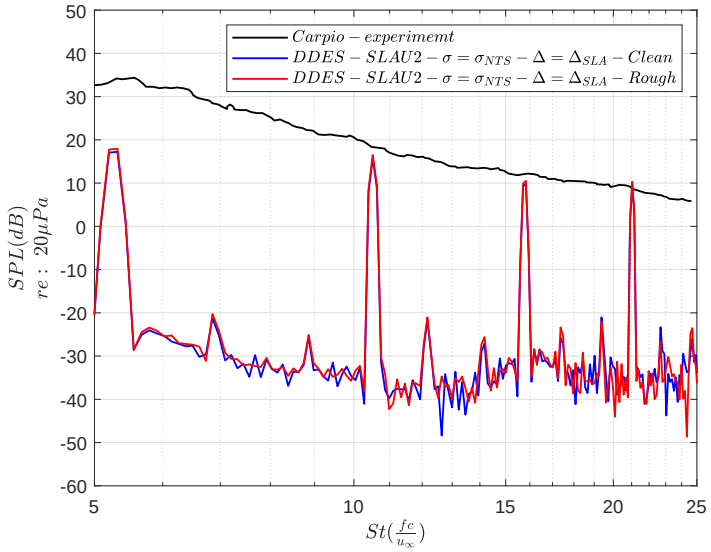

Figure 5.28: Narrow band SPL spectrum at the observer on the midspan plane and perpendicular to the chord at the trailing edge for test cases with and without roughness models.

A variety of factors are surmised to have contributed to failure of the chosen DDES simulation strategy for the NACA0018 TBL-TE noise test case . It is possible that the dynamic surface pressure data sampled for acoustics post-processing was done in the time-period in which the initial transient was still prevalent. A limitation of the current FWH solver is that it is not paralellized, because of which the dynamic surface pressure data cannot be sampled for very long time spans. The Δ_{SLA} SGS length scale has been formulated to accelerate the separation of two-dimensional initial shear layers [42], which would have caused the premature flow separation at the vicinity of trailing edge. The degree of roughness modeled to trip the boundary layer has been inadequate as the results from the roughness case has mirrored the smooth case.

6 CONCLUSIONS AND RECOMMENDATIONS

6.1 Conclusions

In the context of devising a reliable DDES-FWH framework, certain objectives were laid out in chapter 3. This section summarizes the key findings derived by pursuing the different test case studies.

In the two-dimensional laminar cylinder $Re = 150$ test case investigated in section 5.1, a significant discrepancy is observed between the acoustic pressure fluctuations predicted by the Navier-Stokes - FWH process. Nevertheless, the direct resolution of the acoustic pressure is in excellent agreement with the same obtained by a prior LES study [20]. The shortcoming of the time-domain variant of Farassat's 1A FWH integral solution is that for obtaining accurate noise predictions for-two dimensional geometries, data spanning large time samples is required; this has been acknowledged in the literature [2]. Consequently, the quasi-three-dimensional laminar cylinder case $(Re = 1000)$ investigated by Brentner [21] is found to be more appropriate to ensure the correct functioning of the FWH solver as an identical FWH integral solution approach is used. The predictions of the far-field SPL spectrum and the directivity plots at the primary vortex shedding frequency and its first harmonic match the results obtained by Brentner [21], thereby validating the FWH solver.

In the scope of simulating the NACA0021 in deep stall, the chosen temporal resolution in both the physical and pseudo time is justified by evaluating different time steps and inner iterations for the given mesh. The dependence of the flow solution's statistical and spectral properties of the lift and drag coefficients on the chosen span size is investigated. It is found that the lift PSD for the $5c$ span compares better with the experiment than for the $1c$ span. As this has been documented in earlier literature [17], it validates the numerical procedure being followed to conduct the DDES simulations. When used for discretizing the convective fluxes, the purely upwinding Roe scheme results in over-prediction of the lift and drag statistics. Whereas, the SLAU2 scheme with the low dissipation modification σ_{NTS} results in a physically accurate flow solution as the spectral and statistical quantities of the lift and drag coefficients agree excellently with the literature.

Upon evaluating the deep-stall test case with different SGS length scales, the grid-based definition of the SGS length scale is found to be detrimental to the resolution of fine turbulent structures because a large value of eddy viscosity is found in the massively separated wake. Comparable values of eddy viscosity in the near wake are also found with the vorticity-based definition of the SGS length scale Δ_ω, thereby offering little improvement in terms of flow resolution. The flow solution predicted with the use of the Δ_{SLA} SGS length scale entails a massively separated wake region where the value of eddy viscosity is nearly an order of magnitude lower than what has been predicted by the use of Δ_{max} or Δ_ω; thus, offering the best resolution of the wake among the three. The far-field noise signature predicted for the deep stall regime consists of features inherent to separation-stall noise as a high level of low-frequency noise is obtained. The two low-frequency tones observed earlier in the wind tunnel experiments of Moreau [9] are also identified in the narrow band SPL spectrum of the NACA0021 in deep stall, confirming that the predicted noise signature is physically accurate. Finally, the normalized SPL spectrum collapses well with the spectra of the experimentally investigated test cases

of Moreau [9]. The non-dimensional frequency of the tonal peaks are predicted accurately. However, a dependence on the length scale used for Strouhal number scaling is observed. This discrepancy is nevertheless not significant and can be disregarded. The underpredicted magnitude of the normalized PSD of SPL is due to the chosen simulation span being smaller than that of the experimentally investigated geometries. Although the directivity plots of the OASPL and SPL show physically plausible behaviour at low and medium frequencies, they could not be verified due to the unavailability of reliable reference data.

Although, the use of the SLAU2 and Δ_{SLA} captured the flow physics accurately in the case of the NACA0021 in deep stall, the same is not the case when it is used for the case of NACA0018 at 0° angle of attack. The flow is found to separate at the trailing edge which results in an erroneous prediction of the far-field noise that has a tonal signature. This is a fatal error as TBL-TE noise is supposed to be broadband. Using a roughness model is also found to be futile as no improvement is found with respect to the smooth airfoil case.

6.2 Recommendations

- The low-frequency noise signature in the deep stall regime is consistent with the experiments of Moreau [9]. Nevertheless, the magnitude of the normalized PSD is underpredicted; this is expected to be a consequence of using a smaller span size in the simulation. It should be investigated whether using an appropriate span size scaling or a long span correction formula such as the one proposed by Kato [61] would lead to a better agreement with the experimental trends.
- The far-field noise predictions for the NACA0021 in deep stall are still not fully reliable due to the unavailability of experimental acoustic data for such high angles of attack 60°. It would be beneficial to perform a validation study of a test case for which reliable acoustic data is available.
- Using the airfoil surface as the FWH integration surface leads to the negligence of contributions from the terms other than the loading terms. Thus, using solid integration surfaces other than the airfoil surface should be investigated. Extending the current FWH solver to include permeable integration surfaces will enable its use for predictions of separation stall noise at moderate Mach numbers, where it has been found by Turner [11] that quadrupole sources have a sizable contribution.
- The extent of the initial transient was evaluated in the deep stall test case. The same should be done for the NACA0018 test case, following which it is recommended to carry out a convergence study to evaluate the effect of sampling the surface pressure fluctuations for different time spans.
- It is known from the literature that SGS length scale definition Δ_{max} delays flow separation [18] [43] [44]. It can be used advantageously in the NACA0018 test case to avoid flow separation and ensure the correct physics pertinent to TBL-TE noise is captured.
- In the NACA0018 test case, the DDES shielding function f_d given by equation 2.18 should be plotted to identify whether the boundary layer is being resolved or modeled. If the boundary layer is being modeled by URANS, DDES would offer no improvement over the standard URANS solution.

REFERENCES

[1] C. Wagner, T. Hüttl, and P. Sagaut, editors. *Introduction*, page 1–23. Cambridge Aerospace Series. Cambridge University Press, 2007.

[2] B.Y. Zhou, T.A. Albring, N.R. Gauger, T.D. Economon, and J.J. Alonso. *An Efficient Unsteady Aerodynamic and Aeroacoustic Design Framework Using Discrete Adjoint*. 2016.

[3] S. Wagner, R. Bareiß, and G. Guidati. *Wind Turbine Noise*. Springer, Berlin, Heidelberg, 1996.

[4] G. Stewart and D. William, editors. *Aeroacoustics of Low Mach Number Flows*. Academic Press, 2017.

[5] W. Wolf, J.L. Azevedo, and S.K. Lele. *Effects of Mean Flow Convection and Quadrupole Sources on Airfoil Trailing Edge Noise*. 2012.

[6] A.R. Carpio, F. Avallone, and D. Ragni. *On the Role of the Flow Permeability of Metal Foams on Trailing Edge Noise Reduction*. 2018.

[7] C. Teruna, F. Manegar, F. Avallone, D. Ragni, D. Casalino, and T. Carolus. Noise reduction mechanisms of an open-cell metal-foam trailing edge. *Journal of Fluid Mechanics*, 898, 2020.

[8] T. Brooks, D. Pope, and M. Marcolini. Airfoil self-noise and prediction. 1218, 08 1989.

[9] S. Moreau, M. Roger, and J. Christophe. *Flow Features and Self-Noise of Airfoils Near Stall or in Stall*. 2009.

[10] W.R. Wolf, J.G. Kocheemoolayil, and S.K. Lele. *Large Eddy Simulation of Stall Noise*. 06 2014.

[11] J.M. Turner and J.W. Kim. Aerofoil dipole noise due to flow separation and stall at a low reynolds number. *International Journal of Heat and Fluid Flow*, 86:108715, 2020.

[12] C. Mockett. *A comprehensive study of detached-eddy simulation*. Doctoral thesis, Technische Universität Berlin, Fakultät V - Verkehrs- und Maschinensysteme, Berlin, 2009.

[13] K.E. Swalwell. The effect of turbulence on stall of horizontal axis wind turbines. *PhD Thesis*, 2005.

[14] P.R. Spalart. Comments on the feasibility of les for wings, and on a hybrid rans/les approach. *Proceedings of first AFOSR international conference on DNS/LES*, 1997.

[15] M. Shur, P.R. Spalart, M. Strelets, and A. Travin. Detached-eddy simulation of an airfoil at high angle of attack. In W. Rodi and D. Laurence, editors, *Engineering Turbulence Modelling and Experiments 4*, pages 669–678. Elsevier Science Ltd, Oxford, 1999.

[16] Y. Zhang, A. van Zuijlen, and G. van Bussel. *Massively separated turbulent flow simulation around non-rotating MEXICO blade by means of RANS and DDES approaches in OpenFOAM*. 2015.

[17] A. Garbaruk, S. Leicher, C. Mockett, P. Spalart, M. Strelets, and F. Thiele. Evaluation of time sample and span size effects in des of nominally 2d airfoils beyond stall. In Shia-Hui Peng, Piotr Doerffer, and Werner Haase, editors, *Progress in Hybrid RANS-LES Modelling*, pages 87–99, Berlin, Heidelberg, 2010. Springer Berlin Heidelberg.

[18] E. Guseva, A. Garbaruk, and M. Strelets. Assessment of delayed des and improved delayed des combined with a shear-layer-adapted subgrid length-scale in separated flows. *Flow, Turbulence and Combustion*, 98:481–502, 2017.

[19] O. Inoue and N. Hatakeyama. Sound generation by a two-dimensional circular cylinder in a uniform flow. *Journal of Fluid Mechanics*, 471:285–314, November 2002.

[20] D. A. Lysenko, I.S. Ertesvåg, and Kjell Erik Rian. Towards simulation of far-field aerodynamic sound from a circular cylinder using openfoam. *International Journal of Aeroacoustics*, 13(1-2):141–168, 2014.

[21] K. Brentner, J. Cox, C. Rumsey, and B. Younis. Computation of sound generated by flow over a circular cylinder: An acoustic analogy approach. 04 1997.

[22] J.G Schepers. Sirocco: Silent rotors by acoustic optimisation. *Wind turbine noise: perspectives for control, conference proceedings*, 03 2005.

[23] B. Stoevesandt, J.G. Schepers, P. Fuglsang, and S. Yuping, editors. *Wind Turbine Aerodynamic Noise Sources*. Springer, 2022.

[24] F. Farassat. Derivation of formulations 1 and 1a of farassat. 2007.

[25] D. G. Crighton. Computational aeroacoustics for low mach number flows. In Jay C. Hardin and M. Y. Hussaini, editors, *Computational Aeroacoustics*, pages 50–68, New York, NY, 1993. Springer New York.

[26] C. Tim and S.K. Lele. Computational aeroacoustics: progress on nonlinear problems of sound generation. *Progress in Aerospace Sciences*, 40(6):345–416, 2004.

[27] M.J. Lighthill and M.H.A Newman. On sound generated aerodynamically i. general theory. *Proceedings of the Royal Society of London. Series A. Mathematical and Physical Sciences*, 211(1107):564–587, 1952.

[28] J. E. Ffowcs Williams and D. L. Hawkings. Sound generation by turbulence and surfaces in arbitrary motion. *Philosophical Transactions of the Royal Society of London. Series A, Mathematical and Physical Sciences*, 264:321 – 342, 1969.

[29] P. di Francescantonio. A new boundary integral formulation for the prediction of sound radiation. *Journal of Sound and Vibration*, 202(4):491–509, 1997.

[30] M. Shur, P. Spalart, and M. Strelets. Noise prediction for increasingly complex jets. part i: Methods and tests. *International Journal of Aeroacoustics*, 4:213–246, 07 2005.

[31] J. E. Ffowcs Williams and L. H. Hall. Aerodynamic sound generation by turbulent flow in the vicinity of a scattering half plane. *Journal of Fluid Mechanics*, 40(4):657–670, 1970.

[32] R.K. Amiet. Acoustic radiation from an airfoil in a turbulent stream. *Journal of Sound and Vibration*, 41(4):407–420, 1975.

[33] S. Glegg and W. Devenport. Chapter 15 - trailing edge and roughness noise. In S. Glegg and W. Devenport, editors, *Aeroacoustics of Low Mach Number Flows*, pages 365–395. Academic Press, 2017.

[34] A.G. Sagrado and T. Hynes. Wall pressure sources near an airfoil trailing edge under turbulent boundary layers. *Journal of Fluids and Structures*, 30:3–34, 2012.

[35] W.K. Blake. Chapter 5 - noncavitating lifting sections. In W.K. Blake, editor, *Mechanics of Flow-Induced Sound and Vibration, Volume 2 (Second Edition)*, pages 377–503. Academic Press, second edition edition, 2017.

[36] R.W. Paterson, R.K. Amiet, and C.L Munch. Isolated airfoil-tip vortex interaction noise. *Journal of Aircraft*, 12(1):34–40, 1975.

[37] G. Lacagnina, P. Chaitanya, T. Berk, J.H. Kim, P. Joseph, B. Ganapathisubramani, S.M. Hasheminejad, T.P. Chong, O. Stalnov, K.S Choi, M.F. Shahab, M. Omidyeganeh, and A. Pinelli. Mechanisms of airfoil noise near stall conditions. *Phys. Rev. Fluids*, 4:123902, Dec 2019.

[38] F. H. Sighard. *Fluid Dynamic Drag: Practical Information on Aerodynamic Drag and Hydrodynamic Resistance*. Hoerner Fluid Dynamics, 1965.

[39] K. Swalwell, J. Sheridan, and W. Melbourne. *Frequency Analysis of Surface Pressures on an Airfoil After Stall*. 2003.

[40] W. Haase, B. Aupoix, U. Bunge, and D. Schwamborn. *FLOMANIA - a European initiative on flow physics modelling. Results of the European-Union funded project, 2002 - 2004*, volume 94. 01 2006.

[41] W. Haase, M. Braza, and A. Revell. *DESider: A European effort on hybrid RANS-LES Modelling (Notes on numerical fluid mechanics and multidisciplinary design, Vol. 103)*, volume 103. 01 2009.

[42] M. Shur, P. Spalart, M. Strelets, and A. Travin. An enhanced version of des with rapid transition from rans to les in separated flows. *Flow, Turbulence and Combustion*, 95, 12 2015.

[43] E. Molina, C. Spode, R.G.A. da Silva, D.E. Manosalvas-Kjono, S. Nimmagadda, T.D. Economon, J.J. Alonso, and M. Righi. *Hybrid RANS/LES Calculations in SU2*. 2017.

[44] S. Deck. Recent improvements in the zonal detached eddy simulation (zdes) formulation. *Theoretical and Computational Fluid Dynamics*, 26:523–550, 12 2011.

[45] J. S. Park, F. D. Witherden, and P. E. Vincent. High-order implicit large-eddy simulations of flow over a naca0021 aerofoil. *AIAA Journal*, 55(7):2186–2197, 2017.

[46] P. Spalart and S. Allmaras. *A one-equation turbulence model for aerodynamic flows*. 1992.

[47] P. Sagaut, S. Deck, and M. Terracol. *Multiscale and Multiresolution Approaches in Turbulence*. IMPERIAL COLLEGE PRESS, 2nd edition, 2013.

[48] E. Molina, B.Y. Zhou, J.J. Alonso, M. Righi, and R.G. Silva. *Flow and Noise Predictions Around Tandem Cylinders using DDES approach with SU2*.

[49] S. Sharma, T. F. Geyer, and J. Giesler. Effect of geometric parameters on the noise generated by rod-airfoil configuration. *Applied Acoustics*, 177:107908, Jun 2021.

[50] P.R. Spalart. Detached-eddy simulation. *Annual Review of Fluid Mechanics*, 41(1):181–202, 2009.

[51] N. Chauvet, S. Deck, and L. Jacquin. Zonal detached eddy simulation of a controlled propulsive jet. *AIAA Journal*, 45(10):2458–2473, 2007.

[52] T.D. Economon, F. Palacios, S.R. Copeland, T.W. Lukaczyk, and J.J. Alonso. Su2: An open-source suite for multiphysics simulation and design. *AIAA Journal*, 54(3):828–846, 2016.

[53] A. Jameson and S. Shankaran. *An Assessment of Dual-Time Stepping, Time Spectral and Artificial Compressibility Based Numerical Algorithms for Unsteady Flow with Applications to Flapping Wings*.

[54] A. Jameson, W. Schmidt, and E. Turkel. *Numerical solution of the Euler equations by finite volume methods using Runge Kutta time stepping schemes*.

[55] P.L. Roe. Approximate riemann solvers, parameter vectors, and difference schemes. *Journal of Computational Physics*, 43(2):357–372, 1981.

[56] K. Kitamura and E. Shima. Towards shock-stable and accurate hypersonic heating computations: A new pressure flux for ausm-family schemes. *Journal of Computational Physics*, 245:62–83, 2013.

[57] C. Winkler, A. Dorgan, and M. Mani. *A Reduced Dissipation Approach for Unsteady Flows on Unstructured Grids*.

[58] A. Travin, M. Shur, M. Strelets, and P. R. Spalart. Physical and numerical upgrades in the detached-eddy simulation of complex turbulent flows. In R. Friedrich and W. Rodi, editors, *Advances in LES of Complex Flows*, pages 239–254, Dordrecht, 2002. Springer Netherlands.

[59] J.D. Revell, R.A. Prydz, and A.P. Hays. Experimental study of aerodynamic noise vs drag relationships for circular cylinders. *AIAA Journal*, 16(9):889–897, 1978.

[60] J. D. Anderson. *Fundamentals of aerodynamics*. McGraw-Hill series in aeronautical and aerospace engineering. McGraw Hill Education, New York, NY, sixth edition. edition, 2017.

[61] J.C. Giret, A. Sengissen, S. Moreau, M. Sanjosé, and Jean christophe Jouhaud. *Prediction of the sound generated by a rod-airfoil configuration using a compressible unstructured LES solver and a FW-H analogy*.

A ADDITIONAL FLOW FIELD AND NOISE DATA

A.1 NACA0021 in deep stall

A.1.1 Q-criterion contours

Variation of Q-criterion with time

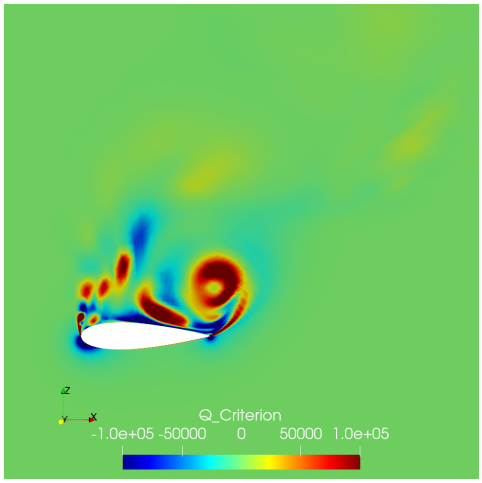

(a) 4871.4 CTU

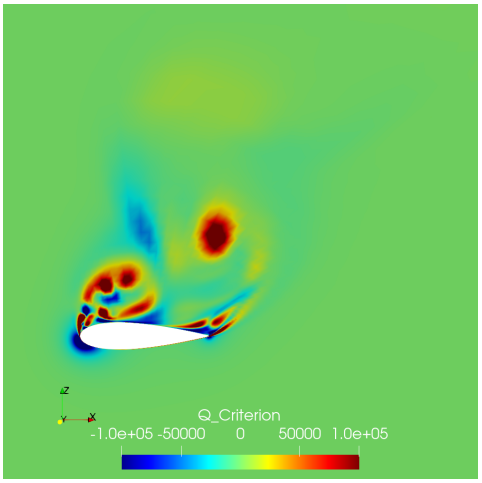

(b) 4872.6 CTU

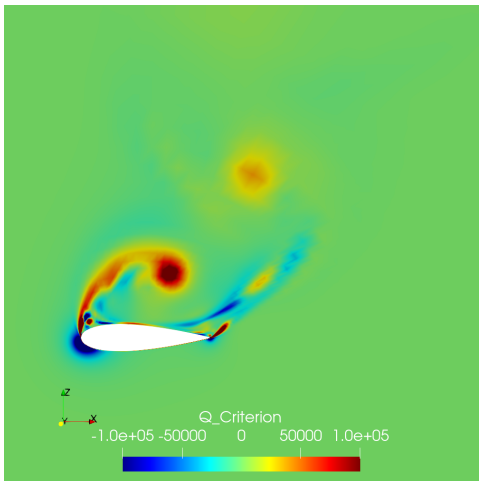

(c) 4873.8 CTU

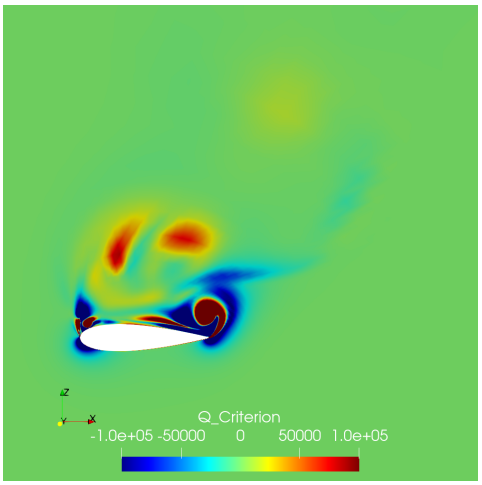

(d) 4875 CTU

Figure A.1: Q-criterion contours at at different instances of vortex shedding at leading and trailing edges at the mid-span section $y/c = -0.5$.

Spanwise variation of Q-criterion

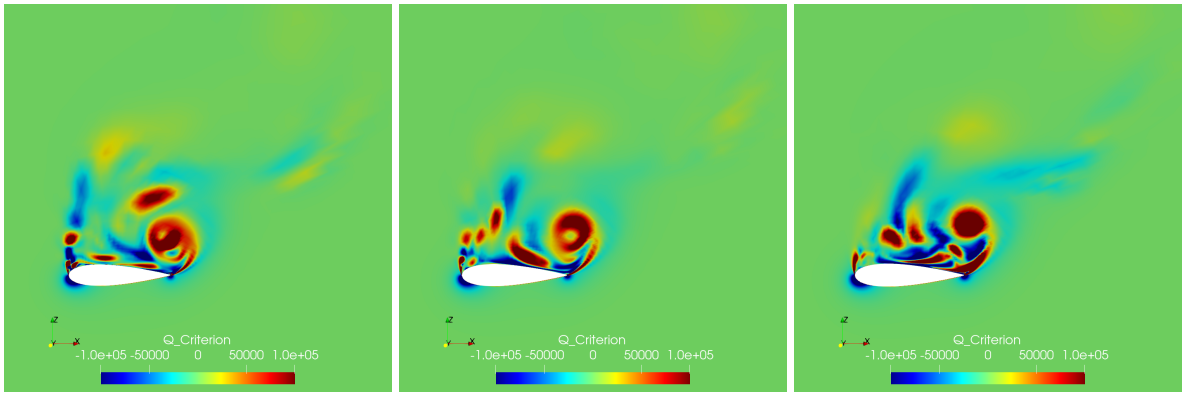

(a) $y = -0.25/c$ (b) $y = -0.5/c$ (c) $y = -0.75/c$

Figure A.2: Spanwise variation of Q-criterion at instance of 4871.4 CTU.

A.1.2 Evaluation of sectional lift and drag coefficients

Anderson [60] derived rudimentary relations for the lift, drag, and moment coefficients for a known surface pressure coefficient distribution on a two-dimensional airfoil section. The geometrical and surface coordinates for the airfoil are shown in figure A.3.

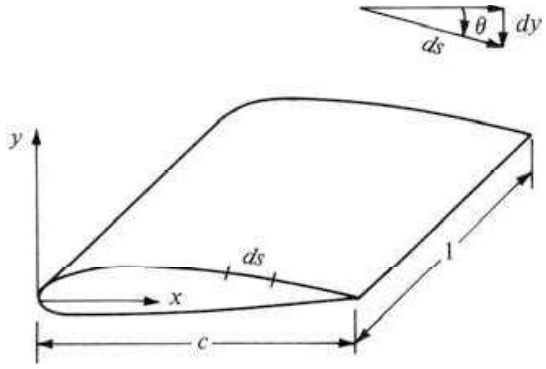

Figure A.3: Geometric and surface coordinates of the two-dimensional airfoil section.

The integral normal and axial force coefficients (c_n and c_a) resulting from a know surface pressure coefficient C_p and skin friction coefficient c_f distribution are given by equation A.1 and equation A.1. The subscripts u and l refer to the upper and lower halves of the airfoil surface.

$$c_n = \frac{1}{c}\left[\int_0^c (C_{p,l} - C_{p,u})\,dx + \int_0^c \left(c_{f,u}\frac{dy_u}{dx} + c_{f,l}\frac{dy_l}{dx}\right)dx\right] \tag{A.1}$$

$$c_a = \frac{1}{c}\left[\int_0^c \left(C_{p,u}\frac{dy_u}{dx} - C_{p,l}\frac{dy_l}{dx}\right)dx + \int_0^c (c_{f,u} + c_{f,l})\,dx\right] \tag{A.2}$$

The eventual lift and drag coefficients are related to the normal and axial force coefficients as per equation A.3 and equation A.4. Here, α is the angle of attack.

$$c_l = c_n \cos\alpha - c_a \sin\alpha \tag{A.3}$$

$$c_d = c_n \sin\alpha + c_a \cos\alpha \tag{A.4}$$

A.1.3 Time-averaged pressure in the massively separated near wake

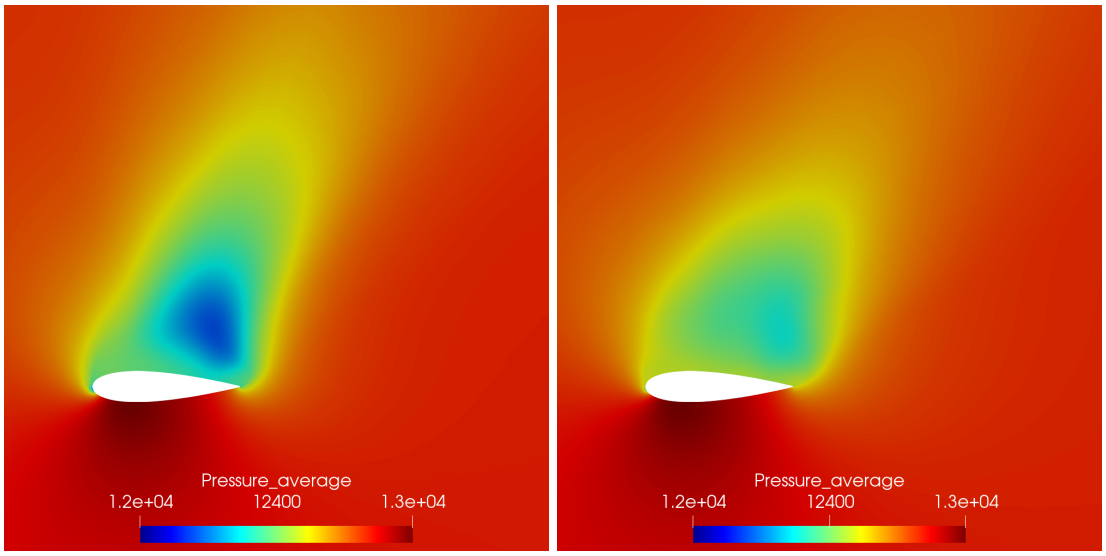

(a) Roe, $\Delta = \Delta_{max}$ (b) SLAU2, $\Delta = \Delta_{max}$

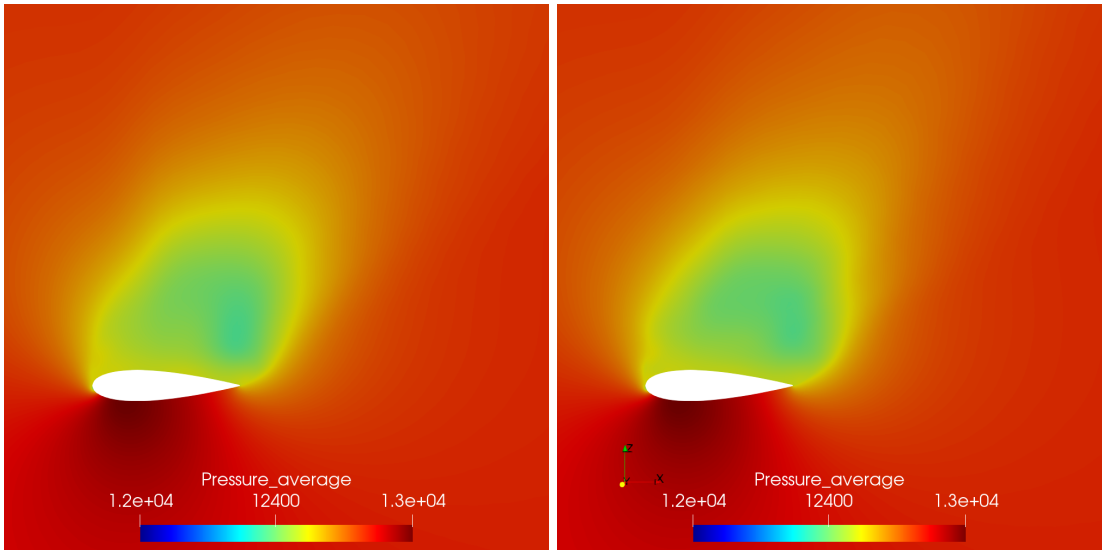

(c) JST, $\Delta = \Delta_{\omega}$ (d) SLAU2, $\Delta = \Delta_{SLA}$

Figure A.4: Comparison of time-averaged pressure distribution in the near wake region at the mid-span plane for the NACA0021 deep stall test case using DDES with different convective schemes and SGS length scales

A.1.4 Need for spanwise averaging of sectional PSDs

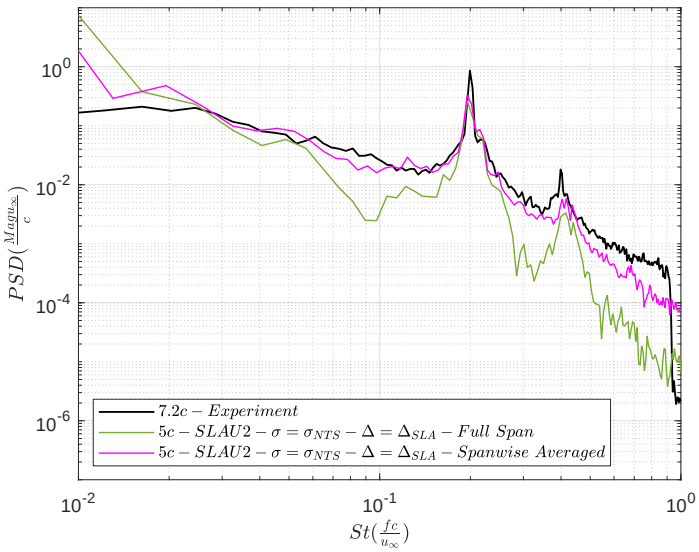

Figure A.5: Comparison of PSD from full span integral lift with the average of sectional PSDs for the airfoil with span $5c$.

A.2 NACA0018 TBL-TE noise test case

A.2.1 Time averaged surface pressure coefficient for the NACA0018 TBL-TE case

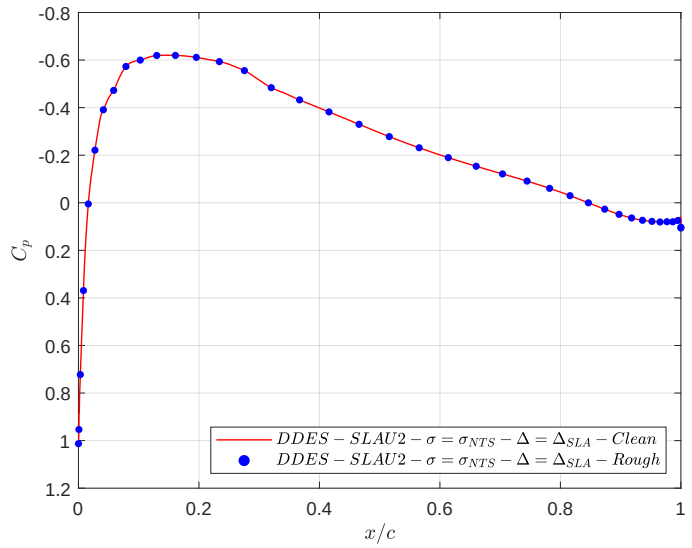

Figure A.6: Time-averaged surface pressure coefficient at the mid-span section on the suction side of the airfoil.

B CONFIGURATION FILES

B.1 Quasi Three-Dimensional Laminar Cylinder

```
    %%%%%%%%%%%%%%%%%%%%%%%%%%%%%%%%%%%%%%%%%%%%%%%%%%%%%%%%%%%%%%%%%%%%%%%%%%%%%%%%
%                                                                                      %
% SU2 configuration file                                                               %
% Case description: Steady, laminar flow around a cylinder (Re 1000)                  %
% Author: Prakyath Pindi Nataraj                                                       %
% Institution:                                    %
% Date: 2021.11.30                                                                     %
% File Version 7.0.8  %
%                                                                                      %
%%%%%%%%%%%%%%%%%%%%%%%%%%%%%%%%%%%%%%%%%%%%%%%%%%%%%%%%%%%%%%%%%%%%%%%%%%%%%%%%%%%

% ------------- DIRECT, ADJOINT, AND LINEARIZED PROBLEM DEFINITION ------------%
%
% Physical governing equations (EULER, NAVIER_STOKES,
%                               WAVE_EQUATION, HEAT_EQUATION, FEM_ELASTICITY,
%                               POISSON_EQUATION)
SOLVER= NAVIER_STOKES
%
% Specify turbulent model (NONE, SA, SA_NEG, SST)
KIND_TURB_MODEL= NONE
%
% Mathematical problem (DIRECT, CONTINUOUS_ADJOINT)
MATH_PROBLEM= DIRECT
%
% Restart solution (NO, YES)
RESTART_SOL=YES

% --------------------- COMPRESSIBLE FREE-STREAM DEFINITION --------------------%
%
% Mach number (non-dimensional, based on the free-stream values)
MACH_NUMBER= 0.2
%
% Angle of attack (degrees, only for compressible flows)
AOA= 0.0
%
% Free-stream temperature (288.15 K by default)
FREESTREAM_TEMPERATURE= 288.15
%
% Reynolds number (non-dimensional, based on the free-stream values)
REYNOLDS_NUMBER= 1000.0
%
% Reynolds length (1 m by default)
REYNOLDS_LENGTH= 1.0

% -------------- COMPRESSIBLE AND INCOMPRESSIBLE FLUID CONSTANTS --------------%
%
% Different gas model (STANDARD_AIR, IDEAL_GAS, VW_GAS, PR_GAS)
FLUID_MODEL= STANDARD_AIR
%
% Ratio of specific heats (1.4 (air), only for compressible flows)
GAMMA_VALUE= 1.4
%
% Specific gas constant (287.87 J/kg*K (air), only for compressible flows)
GAS_CONSTANT= 287.87


% ---------------------- REFERENCE VALUE DEFINITION --------------------------%
```

```
%
% Reference origin for moment computation
REF_ORIGIN_MOMENT_X = 0.00
REF_ORIGIN_MOMENT_Y = 0.00
REF_ORIGIN_MOMENT_Z = 0.00
%
% Reference length for pitching, rolling, and yawing non-dimensional moment
REF_LENGTH= 1.0
%
% Reference area for force coefficients (0 implies automatic calculation)
REF_AREA= 0.0
%
% ------------------------- TIME-DEPENDENT SIMULATION -------------------------------%
%
% Time domain simulation
TIME_DOMAIN= YES
%
% Unsteady simulation (NO, TIME_STEPPING, DUAL_TIME_STEPPING-1ST_ORDER,
%                      DUAL_TIME_STEPPING-2ND_ORDER, HARMONIC_BALANCE)
TIME_MARCHING= DUAL_TIME_STEPPING-2ND_ORDER
%
% Time Step for dual time stepping simulations (s) -- Only used when UNST_CFL_NUMBER = 0.0
% For the DG-FEM solver it is used as a synchronization time when UNST_CFL_NUMBER != 0.0
TIME_STEP= 0.00025
%
% Total Physical Time for dual time stepping simulations (s)
MAX_TIME= 5.00
%
% Unsteady Courant-Friedrichs-Lewy number of the finest grid
UNST_CFL_NUMBER= 0.0
%
%%  Windowed output time averaging
% Time iteration to start the windowed time average in a direct run
% WINDOW_START_ITER = 500
%
% Window used for reverse sweep and direct run. Options (SQUARE, HANN, HANN_SQUARE, %%
%%BUMP) Square is default.
% WINDOW_FUNCTION = SQUARE
INNER_ITER=20
RESTART_ITER=40001

% -------------------- BOUNDARY CONDITION DEFINITION --------------------------%
%
% Navier-Stokes wall boundary marker(s) (NONE = no marker)
MARKER_HEATFLUX= ( cylinder, 0.0 )
%
% Farfield boundary marker(s) (NONE = no marker)
MARKER_FAR= ( freestream )
%
% Marker(s) of the surface to be plotted or designed
MARKER_PLOTTING= ( cylinder )
%
% Marker(s) of the surface where the functional (Cd, Cl, etc.) will be evaluated
MARKER_MONITORING= ( cylinder )

% ------------- COMMON PARAMETERS DEFINING THE NUMERICAL METHOD ---------------%
%
% Numerical method for spatial gradients (GREEN_GAUSS, WEIGHTED_LEAST_SQUARES)
NUM_METHOD_GRAD= WEIGHTED_LEAST_SQUARES
%
% Courant-Friedrichs-Lewy condition of the finest grid
CFL_NUMBER= 50.0
%
% Adaptive CFL number (NO, YES)
CFL_ADAPT= NO
%
% Parameters of the adaptive CFL number (factor down, factor up, CFL min value,
%                                        CFL max value )
CFL_ADAPT_PARAM= ( 0.1, 2.0, 100.0, 1e10 )
%
% Runge-Kutta alpha coefficients
RK_ALPHA_COEFF= ( 0.66667, 0.66667, 1.000000 )
%
```

```
% Number of total iterations
TIME_ITER= 200000

% ------------------------ LINEAR SOLVER DEFINITION ---------------------------%
%
% Linear solver for implicit formulations (BCGSTAB, FGMRES)
LINEAR_SOLVER= FGMRES
%
% Preconditioner of the Krylov linear solver (JACOBI, LINELET, LU_SGS)
LINEAR_SOLVER_PREC= ILU
%
% Minimum error of the linear solver for implicit formulations
LINEAR_SOLVER_ERROR= 1E-10
%
% Max number of iterations of the linear solver for the implicit formulation
LINEAR_SOLVER_ITER= 20

% -------------------- FLOW NUMERICAL METHOD DEFINITION -----------------------%
%
% Convective numerical method (JST, LAX-FRIEDRICH, CUSP, ROE, AUSM, HLLC,
%                              TURKEL_PREC, MSW)
CONV_NUM_METHOD_FLOW= SLAU2
%
% Monotonic Upwind Scheme for Conservation Laws (TVD) in the flow equations.
%           Required for 2nd order upwind schemes (NO, YES)
MUSCL_FLOW= YES
%
% Slope limiter (NONE, VENKATAKRISHNAN, VENKATAKRISHNAN_WANG,
%                BARTH_JESPERSEN, VAN_ALBADA_EDGE)
SLOPE_LIMITER_FLOW= VENKATAKRISHNAN
%
% Coefficient for the Venkat's limiter (upwind scheme). A larger values decrease
%             the extent of limiting, values approaching zero cause
%             lower-order approximation to the solution (0.05 by default)
VENKAT_LIMITER_COEFF= 0.05
%
% Time discretization (RUNGE-KUTTA_EXPLICIT, EULER_IMPLICIT, EULER_EXPLICIT)
TIME_DISCRE_FLOW= EULER_IMPLICIT

% ------------------------ INPUT/OUTPUT INFORMATION --------------------------%
%
% Mesh input file
MESH_FILENAME=/remotefs/ka_usv_01/sv-094990_unix/su2.cases/acoustics/mesh/cylinder_400x400.su2
%
% Mesh input file format (SU2, CGNS, NETCDF_ASCII)
MESH_FORMAT= SU2
%
% Mesh output file
MESH_OUT_FILENAME= mesh_out.su2
%
% Restart flow input file
SOLUTION_FILENAME= restart_flow.dat
%
% Restart adjoint input file
SOLUTION_ADJ_FILENAME= solution_adj.dat
%
% Output file format (PARAVIEW, TECPLOT, STL)
TABULAR_FORMAT= CSV
%
% Output file convergence history (w/o extension)
CONV_FILENAME= history
%
% Output file restart flow
RESTART_FILENAME= restart_flow.dat
%
% Output file restart adjoint
RESTART_ADJ_FILENAME= restart_adj.dat
%
% Output file flow (w/o extension) variables
VOLUME_FILENAME= flow
%
% Output file adjoint (w/o extension) variables
VOLUME_ADJ_FILENAME= adjoint
```

```
%
% Output objective function gradient (using continuous adjoint)
GRAD_OBJFUNC_FILENAME= of_grad.dat
%
% Output file surface flow coefficient (w/o extension)
SURFACE_FILENAME= surface_flow
%
% Output file surface adjoint coefficient (w/o extension)
SURFACE_ADJ_FILENAME= surface_adjoint
%
OUTPUT_FILES= (SURFACE_PARAVIEW)
% Writing solution file frequency
WRT_SOL_FREQ= 4
%
% Writing solution file frequency for physical time steps (dual time)
WRT_SOL_FREQ_DUALTIME= 4
WRT_SURF_FREQ_DUALTIME= 4
%
% Writing convergence history frequency
WRT_CON_FREQ= 1
%
% Writing convergence history frequency (dual time, only written to screen)
WRT_CON_FREQ_DUALTIME=1
WRT_LIMITERS= NO
WRT_RESIDUALS= NO
WRT_PERFORMANCE= YES
%
HISTORY_OUTPUT= ITER, RMS_RES, AERO_COEFF, LINSOL
SCREEN_OUTPUT= OUTER_ITER, TIME_ITER, INNER_ITER, RMS_DENSITY, LIFT, DRAG
VOLUME_OUTPUT=  COORDINATES, PRIMITIVE, VORTEX_IDENTIFICATION, TIME_AVERAGE
% Restart File Writing Frequency
OUTPUT_WRT_FREQ=4
```

B.2 NACA0021 in Deep Stall

```
    %%%%%%%%%%%%%%%%%%%%%%%%%%%%%%%%%%%%%%%%%%%%%%%%%%%%%%%%%%%%%%%%%%%%%%%%%%%%%%%%
%                                                                                      %
% Stanford University unstructured (SU2) configuration file                           %
% Case description: NACA0021 in Deep Stal                                             %
% Author: Prakyath Pindi Nataraj                                                      %
% Institution:         %
% Date:                                                                               %
% File Version SU2 v7.0.8                                                             %
%                                                                                      %
%%%%%%%%%%%%%%%%%%%%%%%%%%%%%%%%%%%%%%%%%%%%%%%%%%%%%%%%%%%%%%%%%%%%%%%%%%%%%%%%

% ------------- DIRECT, ADJOINT, AND LINEARIZED PROBLEM DEFINITION ------------%
%
% Physical governing equations (POTENTIAL_FLOW, EULER, NAVIER_STOKES,
%                               MULTI_SPECIES_NAVIER_STOKES, TWO_PHASE_FLOW,
%                               COMBUSTION)
SOLVER= RANS
%
% Specify turbulence model (NONE, SA, SA_NEG, SST)
KIND_TURB_MODEL= SA
%
% Specify Hybrid RANS/LES for SA family (NONE, SADES, SADDES)
HYBRID_RANSLES= SA_EDDES
%
% DES Constant (0.65)
DES_CONST= 0.65
%
% Mathematical problem (DIRECT, ADJOINT, LINEARIZED, ONE_SHOT_ADJOINT)
MATH_PROBLEM= DIRECT
%
% Restart solution (NO, YES)
RESTART_SOL= YES
% Compute the average solution for unsteady simulations (NO, YES)
COMPUTE_AVERAGE= YES
%
```

```
% ----------- COMPRESSIBLE AND INCOMPRESSIBLE FREE-STREAM DEFINITION ----------%
%
% Mach number (non-dimensional, based on the free-stream values)
MACH_NUMBER= 0.10
%
% Angle of attack (degrees)
AOA= 60
%
% Side-slip angle (degrees)
SIDESLIP_ANGLE= 0.0
%
% Free-stream pressure (101325.0 N/m^2 by default, only Euler flows)
%FREESTREAM_PRESSURE= 101325
%
% Specify Turbulence Intensity (%)
FREESTREAM_TURBULENCEINTENSITY = 0.006
%
% Free-stream temperature (273.15 K by default)
FREESTREAM_TEMPERATURE= 300
%
% Reynolds number (non-dimensional, based on the free-stream values)
REYNOLDS_NUMBER=  2.75E5
%
% Reynolds length (1 m, 1 inch by default)
REYNOLDS_LENGTH= 1

% -------------- COMPRESSIBLE AND INCOMPRESSIBLE FLUID CONSTANTS --------------%
%
% Different gas model (STANDARD_AIR, IDEAL_GAS, VW_GAS, PR_GAS)
FLUID_MODEL= STANDARD_AIR
%
% Ratio of specific heats (1.4 (air), only for compressible flows)
GAMMA_VALUE= 1.4
%
% Specific gas constant (287.87 J/kg*K (air), only for compressible flows)
GAS_CONSTANT= 287.87

% ---------------------- REFERENCE VALUE DEFINITION --------------------------%
%
% Reference origin for moment computation
REF_ORIGIN_MOMENT_X = 0.25
REF_ORIGIN_MOMENT_Y = 0.00
REF_ORIGIN_MOMENT_Z = 0.00
%
% Reference length for pitching, rolling, and yawing non-dimensional moment
REF_LENGTH= 1.0
%
% Reference area for force coefficients (0 implies automatic calculation)
REF_AREA=0
%
% Flow non-dimensionalization (DIMENSIONAL, FREESTREAM_PRESS_EQ_ONE,
%                              FREESTREAM_VEL_EQ_MACH, FREESTREAM_VEL_EQ_ONE)
REF_DIMENSIONALIZATION= DIMENSIONAL
%
% ------------------------- TIME-DEPENDENT SIMULATION --------------------------%
%
% Time domain simulation
TIME_DOMAIN= YES
%
% Unsteady simulation (NO, TIME_STEPPING, DUAL_TIME_STEPPING-1ST_ORDER,
%                      DUAL_TIME_STEPPING-2ND_ORDER, HARMONIC_BALANCE)
TIME_MARCHING= DUAL_TIME_STEPPING-2ND_ORDER
%
% Time Step for dual time stepping simulations (s) -- Only used when UNST_CFL_NUMBER = 0.0
% For the DG-FEM solver it is used as a synchronization time when UNST_CFL_NUMBER != 0.0
TIME_STEP= 0.000864
%
% Total Physical Time for dual time stepping simulations (s)
MAX_TIME= 13.0
%
% Unsteady Courant-Friedrichs-Lewy number of the finest grid
UNST_CFL_NUMBER= 0.0
%
```

```
%%  Windowed output time averaging
% Time iteration to start the windowed time average in a direct run
WINDOW_START_ITER = 500
%
% Window used for reverse sweep and direct run. Options (SQUARE, HANN, HANN_SQUARE, BUMP) Square is default.
WINDOW_FUNCTION = SQUARE
%% Number of internal iterations (dual time method)
INNER_ITER= 40
% Iteration number to begin unsteady restarts
RESTART_ITER= 159001


% -------------------- BOUNDARY CONDITION DEFINITION --------------------------%
%
%
% Navier-Stokes (no-slip), constant heat flux wall  marker(s) (NONE = no marker)
% Format: ( marker name, constant heat flux (J/m^2), ... )
MARKER_HEATFLUX= ( Airfoil, 0.0 )
%
% Navier-Stokes (no-slip), isothermal wall marker(s) (NONE = no marker)
% Format: ( marker name, constant wall temperature (K), ... )
MARKER_ISOTHERMAL= ( NONE )
%
% Far-field boundary marker(s) (NONE = no marker)
MARKER_FAR= ( Farfield )
%
%MARKER_PERIODIC= ( Sym1, Sym2, 0.0, 0.0, 0.0, 0.0, 0.0, 0.0, 0.0, -1.0, 0.0, Sym2, Sym1, 0.0, 0.0, 0.0, 0.0, 0.0, 0.0, 0.0,
% Symmetry boundary marker(s) (NONE = no marker)
%MARKER_SYM= ( Sym1, Sym2 )
MARKER_PERIODIC= (Sym1, Sym2, 0.0, 0.0, 0.0, 0.0, 0.0, 0.0, 0.0, -1.0, 0.0)

%
% Marker(s) of the surface in the surface flow solution file

MARKER_PLOTTING = ( Airfoil )
%MARKER_PLOTTING = ( Sym2 )
%
% Marker(s) of the surface where the non-dimensional coefficients are evaluated.
MARKER_MONITORING = ( Airfoil )
%
% Marker(s) of the surface where obj. func. (design problem) will be evaluated
MARKER_DESIGNING = ( Airfoil )

% ------------- COMMON PARAMETERS TO DEFINE THE NUMERICAL METHOD --------------%
% Numerical method for spatial gradients (GREEN_GAUSS, LEAST_SQUARES,
%                                         WEIGHTED_LEAST_SQUARES)
NUM_METHOD_GRAD= WEIGHTED_LEAST_SQUARES
%
% Courant-Friedrichs-Lewy condition of the finest grid
CFL_NUMBER= 5.0
%
% Adaptive CFL number (NO, YES)
CFL_ADAPT= NO
%
% Parameters of the adaptive CFL number (factor down, factor up, CFL min value,
%                                        CFL max value )
CFL_ADAPT_PARAM= ( 0.0, 0.5, 1.25, 50.0 )
%
% Runge-Kutta alpha coefficients
RK_ALPHA_COEFF= ( 0.66667, 0.66667, 1.000000 )
%
% Number of total iterations
TIME_ITER= 200000
%
% ------------------------ LINEAR SOLVER DEFINITION ---------------------------%
%
% Linear solver or smoother for implicit formulations (BCGSTAB, FGMRES, SMOOTHER_JACOBI,
%                                                      SMOOTHER_ILU0, SMOOTHER_LUSGS,
%                                                      SMOOTHER_LINELET)
LINEAR_SOLVER= FGMRES
%
% Preconditioner of the Krylov linear solver (ILU0, LU_SGS, LINELET, JACOBI)
LINEAR_SOLVER_PREC= ILU\
```

```
%
% Minimum error of the linear solver for implicit formulations
LINEAR_SOLVER_ERROR= 1E-8
%
% Max number of iterations of the linear solver for the implicit formulation
LINEAR_SOLVER_ITER= 40
%
% -------------------- FLOW NUMERICAL METHOD DEFINITION -----------------------%
%
% Convective numerical method (JST, LAX-FRIEDRICH, CUSP, ROE, AUSM, HLLC,
%                              TURKEL_PREC, MSW)
CONV_NUM_METHOD_FLOW= SLAU2
ROE_LOW_DISSIPATION= NTS
%
% Spatial numerical order integration (1ST_ORDER, 2ND_ORDER, 2ND_ORDER_LIMITER)
MUSCL_FLOW= YES
%
% Slope limiter (VENKATAKRISHNAN, BARTH_JESPERSEN)
SLOPE_LIMITER_FLOW=VENKATAKRISHNAN
%
% Entropy fix coefficient (0.0 implies no entropy fixing, 1.0 implies scalar
%                          artificial dissipation)
ENTROPY_FIX_COEFF= 0.0
%
% 1st, 2nd and 4th order artificial dissipation coefficients
%AD_COEFF_FLOW= ( 0.15, 0.5, 0.02 )
%
% Viscous limiter (NO, YES)
%VISCOUS_LIMITER_FLOW= NO
%
% Time discretization (RUNGE-KUTTA_EXPLICIT, EULER_IMPLICIT, EULER_EXPLICIT)
TIME_DISCRE_FLOW= EULER_IMPLICIT
%
% Relaxation coefficient
%RELAXATION_FACTOR_FLOW= 1.0

% -------------------- TURBULENT NUMERICAL METHOD DEFINITION ------------------%
%
% Convective numerical method (SCALAR_UPWIND)
CONV_NUM_METHOD_TURB= SCALAR_UPWIND
%
% Spatial numerical order integration (1ST_ORDER, 2ND_ORDER, 2ND_ORDER_LIMITER)
MUSCL_TURB= NO
%
% Slope limiter (VENKATAKRISHNAN)
SLOPE_LIMITER_TURB= NONE
%
% Viscous limiter (NO, YES)
%VISCOUS_LIMITER_TURB= NO
%
% Time discretization (EULER_IMPLICIT)
TIME_DISCRE_TURB= EULER_IMPLICIT
%
% Reduction factor of the CFL coefficient in the turbulence problem
%CFL_REDUCTION_TURB= 1.0
%
% Relaxation coefficient
%RELAXATION_FACTOR_TURB= 1.0

% ------------------------------- SOLVER CONTROL ------------------------------%
%
% Convergence field
CONV_FIELD= RMS_DENSITY
%
% Min value of the residual (log10 of the residual)
CONV_RESIDUAL_MINVAL= -14
%
% Start convergence criteria at iteration number
CONV_STARTITER= 0
%
% Number of elements to apply the criteria
CONV_CAUCHY_ELEMS= 20
%
```

```
% Epsilon to control the series convergence
CONV_CAUCHY_EPS= 1E-5
%

% ------------------------- GRID ADAPTATION STRATEGY --------------------------%
%
% Percentage of new elements (% of the original number of elements)
NEW_ELEMS= 5
%
% Kind of grid adaptation (NONE, PERIODIC, FULL, FULL_FLOW, GRAD_FLOW, FULL_ADJOINT,
%                          GRAD_ADJOINT, GRAD_FLOW_ADJ, ROBUST,
%                          FULL_LINEAR, COMPUTABLE, COMPUTABLE_ROBUST,
%                          REMAINING, WAKE, SMOOTHING, SUPERSONIC_SHOCK,
%                          TWOPHASE)
KIND_ADAPT= PERIODIC
%
% Scale factor for the dual volume
DUALVOL_POWER= 0.5
%
% Adapt the boundary elements (NO, YES)
ADAPT_BOUNDARY= YES

% ------------------------- INPUT/OUTPUT FILE INFORMATION --------------------------%
%
% Mesh input file
MESH_FILENAME= /remotefs/ka_usv_01/sv-094990_unix/su2.cases/acoustics/mesh/Mesh_naca0021_Ogrid.su2
%
% Mesh input file format (SU2, CGNS)
MESH_FORMAT= SU2
%
% Mesh output file
MESH_OUT_FILENAME= mesh_out.su2
%
% Restart flow input file
SOLUTION_FILENAME= restart_flow.dat
%
% Restart adjoint input file
SOLUTION_ADJ_FILENAME= solution_adj.dat
%
% Output tabular file format (TECPLOT, CSV)
TABULAR_FORMAT= CSV
%
% Files to output
% Possible formats : (TECPLOT, TECPLOT_BINARY, SURFACE_TECPLOT,
%  SURFACE_TECPLOT_BINARY, CSV, SURFACE_CSV, PARAVIEW, PARAVIEW_BINARY, SURFACE_PARAVIEW,
%  SURFACE_PARAVIEW_BINARY, MESH, RESTART_BINARY, RESTART_ASCII, CGNS, STL)
OUTPUT_FILES= (SURFACE_PARAVIEW)
%
% Output file convergence history (w/o extension)
CONV_FILENAME= history
%
% Output file with the forces breakdown
BREAKDOWN_FILENAME= forces_breakdown.dat
%
% Output file restart flow
RESTART_FILENAME= restart_flow.dat
%
% Output file restart adjoint
RESTART_ADJ_FILENAME= restart_adj.dat
%
% Output file flow (w/o extension) variables
VOLUME_FILENAME= flow
%
% Output file adjoint (w/o extension) variables
VOLUME_ADJ_FILENAME= adjoint
%
% Output Objective function
VALUE_OBJFUNC_FILENAME= of_eval.dat
%
% Output objective function gradient (using continuous adjoint)
GRAD_OBJFUNC_FILENAME= of_grad.dat
%
% Output file surface flow coefficient (w/o extension)
```

```
SURFACE_FILENAME= surface_flow
%
% Output file surface adjoint coefficient (w/o extension)
SURFACE_ADJ_FILENAME= surface_adjoint
%
% Read binary restart files (YES, NO)
READ_BINARY_RESTART= YES
%
% Reorient elements based on potential negative volumes (YES/NO)
%REORIENT_ELEMENTS= YES

% Writing solution file frequency
WRT_SOL_FREQ= 1
%
% Writing solution file frequency for physical time steps (dual time)
WRT_SOL_FREQ_DUALTIME= 1
WRT_SURF_FREQ_DUALTIME= 1
%
% Writing convergence history frequency
WRT_CON_FREQ= 1
%
% Writing convergence history frequency (dual time, only written to screen)
WRT_CON_FREQ_DUALTIME= 1
WRT_LIMITERS= NO
WRT_RESIDUALS= NO
WRT_PERFORMANCE= YES
% Writing frequency for volume/surface output
OUTPUT_WRT_FREQ= 1
HISTORY_OUTPUT= ITER, RMS_RES, AERO_COEFF, LINSOL
SCREEN_OUTPUT= TIME_ITER, INNER_ITER, RMS_DENSITY, LIFT, DRAG
VOLUME_OUTPUT=  COORDINATES, PRIMITIVE, VORTEX_IDENTIFICATION, TIME_AVERAGE
```

B.3 NACA0018 TBL-TE

```
    %%%%%%%%%%%%%%%%%%%%%%%%%%%%%%%%%%%%%%%%%%%%%%%%%%%%%%%%%%%%%%%%%%%%%%%%%%%%%%%%
%                                                                                     %
% Stanford University unstructured (SU2) configuration file                          %
% Case description: NACA0018 with roughness                                          %
% Author: Prakyath Pindi Nataraj                                                     %
% Institution:         %
% Date:                                                                              %
% File Version SU2 v7.0.8                                                            %
%                                                                                     %
%%%%%%%%%%%%%%%%%%%%%%%%%%%%%%%%%%%%%%%%%%%%%%%%%%%%%%%%%%%%%%%%%%%%%%%%%%%%%%%%

% ------------- DIRECT, ADJOINT, AND LINEARIZED PROBLEM DEFINITION ------------%
%
% Physical governing equations (POTENTIAL_FLOW, EULER, NAVIER_STOKES,
%                               MULTI_SPECIES_NAVIER_STOKES, TWO_PHASE_FLOW,
%                               COMBUSTION)
SOLVER= RANS
%
% Specify turbulence model (NONE, SA, SA_NEG, SST)
KIND_TURB_MODEL= SA
%
% Specify Hybrid RANS/LES for SA family (NONE, SADES, SADDES)
HYBRID_RANSLES= SA_EDDES
%
% DES Constant (0.65)
DES_CONST= 0.65
%
% Mathematical problem (DIRECT, ADJOINT, LINEARIZED, ONE_SHOT_ADJOINT)
MATH_PROBLEM= DIRECT
%
% Restart solution (NO, YES)
RESTART_SOL= YES
% Compute the average solution for unsteady simulations (NO, YES)
COMPUTE_AVERAGE= YES
%
% ----------- COMPRESSIBLE AND INCOMPRESSIBLE FREE-STREAM DEFINITION ----------%
```

```
%
% Mach number (non-dimensional, based on the free-stream values)
MACH_NUMBER= 0.06
%
% Angle of attack (degrees)
AOA= 0
%
% Side-slip angle (degrees)
SIDESLIP_ANGLE= 0.0
%
% Free-stream pressure (101325.0 N/m^2 by default, only Euler flows)
%FREESTREAM_PRESSURE= 101325
%
% Specify Turbulence Intensity (0.001=0.1%)
FREESTREAM_TURBULENCEINTENSITY = 0.001
%
% Free-stream temperature (273.15 K by default)
FREESTREAM_TEMPERATURE= 300
%
% Reynolds number (non-dimensional, based on the free-stream values)
REYNOLDS_NUMBER=  2.80E5
%
% Reynolds length (1 m, 1 inch by default)
REYNOLDS_LENGTH= 1

% -------------- COMPRESSIBLE AND INCOMPRESSIBLE FLUID CONSTANTS --------------%
%
% Different gas model (STANDARD_AIR, IDEAL_GAS, VW_GAS, PR_GAS)
FLUID_MODEL= STANDARD_AIR
%
% Ratio of specific heats (1.4 (air), only for compressible flows)
GAMMA_VALUE= 1.4
%
% Specific gas constant (287.87 J/kg*K (air), only for compressible flows)
GAS_CONSTANT= 287.87

% ---------------------- REFERENCE VALUE DEFINITION --------------------------%
%
% Reference origin for moment computation
REF_ORIGIN_MOMENT_X = 0.25
REF_ORIGIN_MOMENT_Y = 0.00
REF_ORIGIN_MOMENT_Z = 0.00
%
% Reference length for pitching, rolling, and yawing non-dimensional moment
REF_LENGTH= 1.0
%
% Reference area for force coefficients (0 implies automatic calculation)
REF_AREA=0
%
% Flow non-dimensionalization (DIMENSIONAL, FREESTREAM_PRESS_EQ_ONE,
%                              FREESTREAM_VEL_EQ_MACH, FREESTREAM_VEL_EQ_ONE)
REF_DIMENSIONALIZATION= DIMENSIONAL
%REF_DIMENSIONALIZATION= FREESTREAM_PRESS_EQ_ONE
%
% ------------------------- TIME-DEPENDENT SIMULATION --------------------------%
%
% Time domain simulation
TIME_DOMAIN= YES
%
% Unsteady simulation (NO, TIME_STEPPING, DUAL_TIME_STEPPING-1ST_ORDER,
%                      DUAL_TIME_STEPPING-2ND_ORDER, HARMONIC_BALANCE)
%TIME_MARCHING= DUAL_TIME_STEPPING-1ST_ORDER
TIME_MARCHING= DUAL_TIME_STEPPING-2ND_ORDER
%
% Time Step for dual time stepping simulations (s) -- Only used when UNST_CFL_NUMBER = 0.0
% For the DG-FEM solver it is used as a synchronization time when UNST_CFL_NUMBER != 0.0
TIME_STEP= 0.00005
% Total Physical Time for dual time stepping simulations (s)
MAX_TIME= 5.0
%
% Unsteady Courant-Friedrichs-Lewy number of the finest grid
UNST_CFL_NUMBER= 0.0
%
```

```
%%  Windowed output time averaging
% Time iteration to start the windowed time average in a direct run
WINDOW_START_ITER = 500
%
% Window used for reverse sweep and direct run. Options (SQUARE, HANN, HANN_SQUARE, BUMP) Square is default.
WINDOW_FUNCTION = SQUARE
%% Number of internal iterations (dual time method)
INNER_ITER= 10
% Iteration number to begin unsteady restarts
RESTART_ITER= 150001
%
% ------------------- BOUNDARY CONDITION DEFINITION -------------------------%
%
%
% Navier-Stokes (no-slip), constant heat flux wall  marker(s) (NONE = no marker)
% Format: ( marker name, constant heat flux (J/m^2), ... )
MARKER_HEATFLUX= ( airfoil, 0.0, airfoil_rough, 0.0 )
%
WALL_ROUGHNESS= (airfoil_rough, 0.01411)
% Navier-Stokes (no-slip), isothermal wall marker(s) (NONE = no marker)
% Format: ( marker name, constant wall temperature (K), ... )
MARKER_ISOTHERMAL= ( NONE )
%
% Far-field boundary marker(s) (NONE = no marker)
MARKER_FAR= ( farfield )
%
MARKER_PERIODIC= (sym1, sym2, 0.0, 0.0, 0.0, 0.0, 0.0, 0.0, 0.0, 0.1, 0.0)
%
% Marker(s) of the surface in the surface flow solution file
MARKER_PLOTTING = ( airfoil, airfoil_rough )
%MARKER_PLOTTING = ( Sym2 )
%
% Marker(s) of the surface where the non-dimensional coefficients are evaluated.
MARKER_MONITORING = ( airfoil, airfoil_rough )
%
% Marker(s) of the surface where obj. func. (design problem) will be evaluated
MARKER_DESIGNING = ( airfoil )

% ------------- COMMON PARAMETERS TO DEFINE THE NUMERICAL METHOD --------------%
% Numerical method for spatial gradients (GREEN_GAUSS, LEAST_SQUARES,
%                                         WEIGHTED_LEAST_SQUARES)
NUM_METHOD_GRAD= GREEN_GAUSS
%
% Courant-Friedrichs-Lewy condition of the finest grid
CFL_NUMBER= 0.1
%
% Adaptive CFL number (NO, YES)
CFL_ADAPT= NO
%
% Parameters of the adaptive CFL number (factor down, factor up, CFL min value,
%                                        CFL max value )
CFL_ADAPT_PARAM= ( 0.0, 0.5, 1.25, 50.0 )
%
% Runge-Kutta alpha coefficients
RK_ALPHA_COEFF= ( 0.66667, 0.66667, 1.000000 )
%
% Number of total iterations
TIME_ITER= 200000
%%
% ------------------------ LINEAR SOLVER DEFINITION ---------------------------%
%
% Linear solver or smoother for implicit formulations (BCGSTAB, FGMRES, SMOOTHER_JACOBI,
%                                                      SMOOTHER_ILU0, SMOOTHER_LUSGS,
%                                                      SMOOTHER_LINELET)
LINEAR_SOLVER= FGMRES
%
% Preconditioner of the Krylov linear solver (ILU0, LU_SGS, LINELET, JACOBI)
LINEAR_SOLVER_PREC= ILU
%LINEAR_SOLVER_ILU_FILL_IN= 0
%
% Minimum error of the linear solver for implicit formulations
LINEAR_SOLVER_ERROR= 1E-6
%
```

```
% Max number of iterations of the linear solver for the implicit formulation
LINEAR_SOLVER_ITER= 20
%
% -------------------- FLOW NUMERICAL METHOD DEFINITION -----------------------%
%
% Convective numerical method (JST, LAX-FRIEDRICH, CUSP, ROE, AUSM, HLLC,
%                              TURKEL_PREC, MSW)
CONV_NUM_METHOD_FLOW= SLAU2
ROE_LOW_DISSIPATION= NTS
%
% Spatial numerical order integration (1ST_ORDER, 2ND_ORDER, 2ND_ORDER_LIMITER)
MUSCL_FLOW= YES
%MUSCL_FLOW= NO
%
% Slope limiter (VENKATAKRISHNAN, BARTH_JESPERSEN)
SLOPE_LIMITER_FLOW=VENKATAKRISHNAN
%
% Entropy fix coefficient (0.0 implies no entropy fixing, 1.0 implies scalar
%                          artificial dissipation)
ENTROPY_FIX_COEFF= 0.0
%
% 1st, 2nd and 4th order artificial dissipation coefficients
%AD_COEFF_FLOW= ( 0.15, 0.5, 0.02 )
%
% Viscous limiter (NO, YES)
%VISCOUS_LIMITER_FLOW= NO
%
% Time discretization (RUNGE-KUTTA_EXPLICIT, EULER_IMPLICIT, EULER_EXPLICIT)
TIME_DISCRE_FLOW= EULER_IMPLICIT
%
% Relaxation coefficient
%RELAXATION_FACTOR_FLOW= 1.0

% -------------------- TURBULENT NUMERICAL METHOD DEFINITION ------------------%
%
% Convective numerical method (SCALAR_UPWIND)
CONV_NUM_METHOD_TURB= SCALAR_UPWIND
%
% Spatial numerical order integration (1ST_ORDER, 2ND_ORDER, 2ND_ORDER_LIMITER)
MUSCL_TURB= NO
%
% Slope limiter (VENKATAKRISHNAN)
SLOPE_LIMITER_TURB= NONE
%
% Viscous limiter (NO, YES)
%VISCOUS_LIMITER_TURB= NO
%
% Time discretization (EULER_IMPLICIT)
TIME_DISCRE_TURB= EULER_IMPLICIT
%
% Reduction factor of the CFL coefficient in the turbulence problem
%CFL_REDUCTION_TURB= 1.0
%
% Relaxation coefficient
%RELAXATION_FACTOR_TURB= 1.0

% ------------------------------- SOLVER CONTROL ------------------------------%
%
% Convergence field
CONV_FIELD= RMS_DENSITY
%
% Min value of the residual (log10 of the residual)
CONV_RESIDUAL_MINVAL= -14
%
% Start convergence criteria at iteration number
CONV_STARTITER= 0
%
% Number of elements to apply the criteria
CONV_CAUCHY_ELEMS= 100
%
% Epsilon to control the series convergence
CONV_CAUCHY_EPS= 1E-5
%
```

```
% ------------------------ GRID ADAPTATION STRATEGY -------------------------%
%
% Percentage of new elements (% of the original number of elements)
NEW_ELEMS= 5
%
% Kind of grid adaptation (NONE, PERIODIC, FULL, FULL_FLOW, GRAD_FLOW, FULL_ADJOINT,
%                          GRAD_ADJOINT, GRAD_FLOW_ADJ, ROBUST,
%                          FULL_LINEAR, COMPUTABLE, COMPUTABLE_ROBUST,
%                          REMAINING, WAKE, SMOOTHING, SUPERSONIC_SHOCK,
%                          TWOPHASE)
KIND_ADAPT= PERIODIC
%
% Scale factor for the dual volume
DUALVOL_POWER= 0.5
%
% Adapt the boundary elements (NO, YES)
ADAPT_BOUNDARY= YES

% ------------------------ INPUT/OUTPUT FILE INFORMATION --------------------------%
%
% Mesh input file
MESH_FILENAME= /remotefs/ka_usv_01/sv-094990_unix/su2.cases/acoustics/mesh/naca0018_513x513x0.1.su2
%
% Mesh input file format (SU2, CGNS)
MESH_FORMAT= SU2
%
% Mesh output file
MESH_OUT_FILENAME= mesh_out.su2
%
% Restart flow input file
SOLUTION_FILENAME= /remotefs/ra_usv_092942/prakyath/naca_0018_rough/dt5e-5_eddes/restart/restart_flow.dat
%
% Restart adjoint input file
SOLUTION_ADJ_FILENAME= solution_adj.dat
%
% Output tabular file format (TECPLOT, CSV)
TABULAR_FORMAT= CSV
%
% Files to output
% Possible formats : (TECPLOT, TECPLOT_BINARY, SURFACE_TECPLOT,
%  SURFACE_TECPLOT_BINARY, CSV, SURFACE_CSV, PARAVIEW, PARAVIEW_BINARY, SURFACE_PARAVIEW,
%  SURFACE_PARAVIEW_BINARY, MESH, RESTART_BINARY, RESTART_ASCII, CGNS, STL)
% default : (RESTART, PARAVIEW, SURFACE_PARAVIEW)
OUTPUT_FILES= (RESTART)
%, PARAVIEW)
%
% Output file convergence history (w/o extension)
CONV_FILENAME= history
%
% Output file with the forces breakdown
BREAKDOWN_FILENAME= forces_breakdown.dat
%
% Output file restart flow
RESTART_FILENAME= /remotefs/ra_usv_092942/prakyath/naca_0018_rough/dt5e-5_eddes/restart/restart_flow.dat
%
% Output file restart adjoint
RESTART_ADJ_FILENAME= restart_adj.dat
%
% Output file flow (w/o extension) variables
VOLUME_FILENAME= /remotefs/ra_usv_092942/prakyath/naca_0018_rough/dt5e-5_eddes/flow/flow
%
% Output file adjoint (w/o extension) variables
VOLUME_ADJ_FILENAME= adjoint
%
% Output Objective function
VALUE_OBJFUNC_FILENAME= of_eval.dat
%
% Output objective function gradient (using continuous adjoint)
GRAD_OBJFUNC_FILENAME= of_grad.dat
%
% Output file surface flow coefficient (w/o extension)
SURFACE_FILENAME= /remotefs/ra_usv_092942/prakyath/naca_0018_rough/dt5e-5_eddes/surface_flow/surface_flow
```

```
%
% Output file surface adjoint coefficient (w/o extension)
SURFACE_ADJ_FILENAME= surface_adjoint
%
% Read binary restart files (YES, NO)
%READ_BINARY_RESTART= YES
%
% Reorient elements based on potential negative volumes (YES/NO)
%REORIENT_ELEMENTS= YES

% Writing convergence history frequency (dual time, only written to screen)
WRT_CON_FREQ_DUALTIME= 1
WRT_LIMITERS= NO
WRT_RESIDUALS= NO
WRT_PERFORMANCE= YES
% Writing frequency for volume/surface output
OUTPUT_WRT_FREQ= 10000
HISTORY_OUTPUT= ITER, RMS_RES, AERO_COEFF,LINSOL
SCREEN_OUTPUT= WALL_TIME,TIME_ITER, INNER_ITER, RMS_DENSITY, RMS_MOMENTUM_X, LIFT, DRAG
```